Fall 12-15-2023

Spatial and Temporal Variability in Snow Properties and Firn Volume Across the Juneau Icefield in Southeast Alaska

Mikaila Mannello
mikaila.mannello@maine.edu

SPATIAL AND TEMPORAL VARIABILITY IN SNOW PROPERTIES AND

FIRN VOLUME ACROSS THE JUNEAU ICEFIELD

IN SOUTHEAST ALASKA

By

Mikaila A. Mannello

B.S. University of Pittsburgh, 2020

A THESIS

Submitted in Partial Fulfillment of the

Requirements for the Degree of

Master of Science

(in Quaternary and Climate Studies)

The Graduate School

The University of Maine

December 2023

Advisory Committee:

Seth Campbell, Associate Professor School of Earth and Climate Sciences, Climate Change Institute, Advisor

Kristin Schild, Assistant Professor School of Earth and Climate Sciences, Climate Change Institute

Peter Koons, Emeritus Professor School of Earth and Climate Science, Climate Change Institute

SPATIAL AND TEMPORAL VARIABILITY IN SNOW PROPERTIES AND

FIRN VOLUME ACROSS THE JUNEAU ICEFIELD

IN SOUTHEAST ALASKA

By Mikaila A. Mannello

Thesis Advisor: Dr. Seth Campbell

Abstract. Glaciers are important freshwater resources which have far reaching impacts on a range of local to global systems and processes, including ecosystems and societies. As global climate continues to change, the response of glaciers has largely been reductions in ice mass and widespread retreat. A high degree of accumulation and ablation occurs in the near surface which is exposed to the atmosphere. The Juneau Icefield (JIF) has, up until the mid-2010s, historically responded climate change anomalously where its main drainage, Taku Glacier (here forward referred to its native name T'aak̲ú K̲wáan Sít'i), has been advancing while all other JIF outlet glaciers have been retreating for years.

In this thesis, I quantify and compare snow water equivalent (SWE) of the annual accumulation between 2012 (pre-retreat) and 2021 (during retreat) with repeated 400 MHz common-offset ground-penetrating radar (GPR) surveys across the southern portion of the Juneau Icefield which includes T'aak̲ú K̲wáan Sít'i and its main tributaries. Because these calculations require assumptions of radio wave velocity which depends on liquid water content and density, both properties that can vary spatially and temporally, I quantify this variability with ground-truthed measurements to determine bulk relative permittivity in the annual accumulation. From

this, I determine the range of liquid water content in the snowpack. I additionally quantify the difference in firn thickness and volume across JIF over this time period from the same GPR dataset and begin to investigate the potential causes of this change.

The SWE in 2012 ranged between 42-688 cm water equivalent (cm w.e.) and in 2021 between 15-570 cm w.e. The depth-density relationship is relatively consistent across JIF, so I conclude that variability in liquid water content is the likely driver for variability in derived relative permittivity. Between 2012 and 2021, JIF experienced widespread firn thinning that resulted in an approximate reduction of firn volume by 51.3 percent. This difference in firn thickness was most highly correlated with marine proximity and elevation. From the investigation into glacier velocity, it is likely that the observed firn thinning was not due to dynamic thinning and was likely a result of increased ablation, decreased accumulation, or increased densification rates.

These decadal-scale observations have implications for the future health of JIF and for interpretations of GPR data in temperate glacier environments. First, such a drastic decrease in firn volume reduces the mass influx to glacier ice and its ability to store short-term melt water while also potentially increasing JIF's susceptibility to contributing more to global sea-level rise. Second, the variability in relative permittivity across the study site suggests potential for high uncertainty in depth (30.5-54.1%) and SWE (32.2-56.2%) calculations due to spatial and, likely, temporal variability in liquid water content when using GPR to determine both variables in a temperate environment.

DEDICATION

To my family and teachers who have encouraged my curiosity and enthusiasm in science.

ACKNOWLEDGEMENTS

To Emma Erwin and Inga Kindstedt, thank you for "reeling me in" and making me feel valued and supported from near and far since the beginning. I credit our pizza nights, "picture this" moments, long skis, and adventures and laughs together for helping me through many of the highs and lows of grad school times.

To my roommates, Zoe Benedict, Inga, Cassie Stirpe, Keegan, Tahi Wiggins, and Jordan Farnsworth, you've seen it all and I'm so grateful for your constant, generous, and kind words of encouragement (and your baked goods too). To my 300D fam, Erin Towns, Keegan Bellamy, and Renée Clavette, thank you for always listening and laughing together – it continues to be a pleasure to navigate grad school and the void with you. To Sydney Baratta, thank you for the many sustaining coffee dates and relentless support. Additionally, thank you to all of those of the UMaine Polar Geophysics team and Icy Lab for both the formal and informal undying encouragement in the glaciology community.

To all of those who I've been fortunate to be in the field with so far including (but not limited to), Jon, Kira Holland, Darren Farley, Pierre Valero, Martin Truffer, Doug Brinkerhoff, Michael Daniel, Victor Devaux-Chupin, Annegret Pohle, Emma, Inga, Renée, James Minifie, Seth, Mari Fromstein, and Erin, thank you for facilitating and participating in an environment of learning that pushes me to be a better scientist, team member, and leader and for experiencing the most amazing of places with me. And thank you to my adventure buddy, 400-friend, for always being up for a radar walk/ski! Thank you to the folks of the Juneau Icefield Research Program for fostering community, curiosity, formative field experiences, and without whom's support, this work would not have been possible.

This work was not done in isolation and I would like to explicitly express my sincere thanks to those who have contributed as coauthors, collaborators, and to preliminary and foundational

TABLE OF CONTENTS

LIST OF TABLES

LIST OF FIGURES

CHAPTER 1

INTRODUCTION

1.1. Background

Global freshwater resources are continually changing which is concerning because glaciers and snow provide meltwater for roughly two billion people or a quarter of the Earth's population. Glaciers hold and release this critical human and environmental resource, driving micro- to macro-scale water resource and ecological processes (Beniston, 2003). Despite this, several variables make it difficult to quantify water flux in glacial systems such as, topographic complexities, unknowns of englacial water storage and movement, and instrumental assumptions and constraints. These broad scale uncertainties are complicated more by a changing global climate.

Alpine glaciers in Alaska and Northwest Canada are experiencing the greatest rates of mass loss and therefore are among the greatest contributors to global sea-level rise, excluding the continental ice sheets and oceanic thermal expansion (Zemp and others, 2019; Hugonnet and others, 2021; Rounce and others, 2023). Temperate glaciers populating much of this zone are incredibly sensitive to temperature change, as they exist at pressure melting point. For example, the Juneau Icefield (JIF) in Southeast Alaska and Northern British Columbia is a temperate glacier system and between 1946-2005, mean annual temperatures in Juneau rose 1.6°C (Criscitiello and others, 2010). With the Parallel Ice Sheet Model modeling the evolution of the Juneau Icefield through the end of this century, Ziemen and others (2016) predict a 58 to 68 percent decrease in ice volume from 2010 volume by the end of the century under the RCP6.0 (+ 2.8°C, globally) emissions scenario. As temperature affects both precipitation type and ablation rate, the future of the Juneau Icefield will likely be tied to these changes.

The accumulation and ablation zones of mountain glaciers are subject to high spatial and temporal variability of mass input and loss, especially in regions with intense topographic relief. This relief creates variations in local to regional weather and climate patterns that impact accumulation and melt. JIF, spanning from sea-level to 1840 m a.s.l., is subjected to both high accumulation and high ablation throughout the year (Roth and others, 2018). T'aaḵú Ḵwáan Sít'i, the main drainage of the southern portion of JIF, and Lemon Creek Glacier have been extensively studied and monitored through the Juneau Icefield Research Program's Mass Balance Program since 1946, providing an extensive 77-year record of glacier change (Pelto and others, 2013; McNeil and others, 2020). Recent work demonstrated that during a summer study period, net shortwave and longwave radiation accounted for the large majority of melting, followed by smaller contributions from latent heat flux and sensible heat flux (Clayton, 2019). The microclimates of this region and large accumulation area ratio (AAR) of T'aaḵú Ḵwáan Sít'i have historically protected the region from mass loss despite increasing atmospheric temperatures, facilitating glacial advance until the mid-2010s when the regional changes in climate began to overwhelm the large AAR effect, ultimately leading to retreat (McNeil and others, 2020).

Similar to precipitation and ablation, what happens to meltwater which travels along the surface or into a glacier is highly variable, spatially and temporally. Liquid water is prevalent englacially, especially in temperate glacier systems, and may 1) runoff from the surface directly, 2) create snow or firn aquifers, 3) travel through englacial channels like crevasses and moulins, and 4) percolate through the snow and firn (Jansson and others, 2003). Near surface meltwater formation, storage, and movement is most susceptible to rapid changes in atmospheric conditions. Liquid water in snow and firn carries latent heat, and increased incidence of rain events (due to rising atmospheric temperatures) densify the snowpack, increasing the overburden pressure on

firn. Increased melt events decrease the survival of winter accumulation, reducing the mass input to firn and glacier ice. As the AAR decreases – primarily driven by rising atmospheric temperatures – less snow survives the melt season, so one would expect to see firn thinning impacting the potential for long-term meltwater storage. Previous research in Greenland suggests that firn can store meltwater in aquifers, buffering its release and resulting in delayed contributions to global sea-level rise (Harper and others, 2012). However, the residence time and volume of snow and firn water storage are both relatively unknown across nearly all glacier systems. For example, despite extensive surveys conducted across the Juneau Icefield since the 1940's, quantitative estimates of liquid water storage, as well as the evolution of firn structure, thickness, and volume changes, have not yet been quantified.

While mass balance surveys via the glaciological method are effective at capturing overall trends of snow accumulation or ablation at point locations which then may be interpolated and extrapolated across the glacier area, these are time- and labor-intensive. Ground-penetrating radar (GPR) surveys are non-destructive, spatially continuous, and a relatively rapid method to evaluate snow and firn thickness and associated properties such as density and water content, and continuity of englacial stratigraphy visualized within snow pits or shallow firn cores (Arcone and others, 1995; Nolan and others, 1995; Arcone, 2002; Dunse and others, 2009; Campbell and others, 2013; Schroeder, 2023). Interpretations of GPR surveys require contextual knowledge and key material assumptions to identify features and appropriate depth. In polar (cold) glacial environments, differences in chemistry and density of snow and firn are the drivers of layer reflections and attenuation rates are small due to minimal scattering, resulting in deep survey (100's of m) capabilities with high frequency (100-900 MHz) GPR antennas (Kovacs 1995). Additionally, radio wave velocities in polar snow, firn, and ice are solely dependent on density meaning that

quantifying radio wave velocities, associated depths of horizons, and calculating volume and SWE in polar glacier snow and firn is relatively trivial if density information is available. By contrast, the existence of liquid water in temperate glacial environments reduces the depth of survey penetration due to scattering and is an additional factor to density which influences radio wave velocities and associated layer depth calculations (Tiuri and others, 1984). To quantify annual accumulation depth and interpret firn evolution over time (thinning or thickening) of a temperate glacier system, it is therefore necessary to consider spatial-temporal variations in density and liquid water content. This thesis focuses on quantifying these variables across JIF in Southeast Alaska and Northern British Columbia.

1.2. Study Site: Juneau Icefield, Alaska

JIF is located on the coast of Southeast Alaska nearest to Juneau, Alaska (Dzantik'i Héeni) and Atlin, British Columbia (Áa Tlein) (Thornton, 2010) (Fig. 1.1). It is considered part of the northern Pacific Coastal Temperate Rainforest existing in a maritime climate (Pelto and others, 2013; O'Neel and others, 2015). Using available image pairs throughout a year and in-situ summer velocity stake measurements, Melkonian and others (2014) concluded that between 2000-2013 that the surface flow velocity of JIF showed seasonal variability but did not display signs of interannual velocity variability. It experiences high accumulation and ablation throughout a year and JIF receives approximately 3-4 m water equivalent (w.e.) each year and modeled precipitation patterns indicate that across the icefield the precipitation varies between 2.5-4.4 m w.e. (Pelto and others, 2013; Roth and others, 2018). During the summer months, melt is prevalent across all elevations (Ramage and others, 2000). This positions JIF well to represent regional impacts of climate change in coastal temperate environments.

T'aa<u>k</u>ú <u>K</u>wáan Sít'i (the T'aakú peoples' glacier, Taku Glacier), which drains most of the southern portion of the Juneau Icefield, is the deepest temperate glacier in North America (Nolan and others, 1995) and is a tidewater glacier protected by a substantial thrust moraine of eroded sediment (Zechmann and others, 2020). There are several tributary branches to the main T'aa<u>k</u>ú <u>K</u>wáan Sít'i which include Southwest Branch (SWB), Northern-Northwest Branch (NWBN), Southern-Northwest Branch (NWBS), Echo Branches Center (ECHO_C) and Right (ECHO_R), Matthes Glacier (MT), and Demorest Glacier (DEM) (Fig. 1.1). Together, the area of the T'aa<u>k</u>ú <u>K</u>wáan Sít'i drainage system is 671 km^2 (Pelto and others, 2013). Between 1989 to 2018, the equilibrium line altitude (ELA) rose from 1115 m a.s.l. to 1308 m a.s.l., resulting in a decreased accumulation area (McNeil and others, 2020). Because T'aa<u>k</u>ú <u>K</u>wáan Sít'i lies in an over-deepened bed, if retreat continues the glacier becomes more susceptible to enhanced melt with the erosion of the terminal moraine and marine intrusion (Nolan and others, 1995; Zechmann and others, 2020).
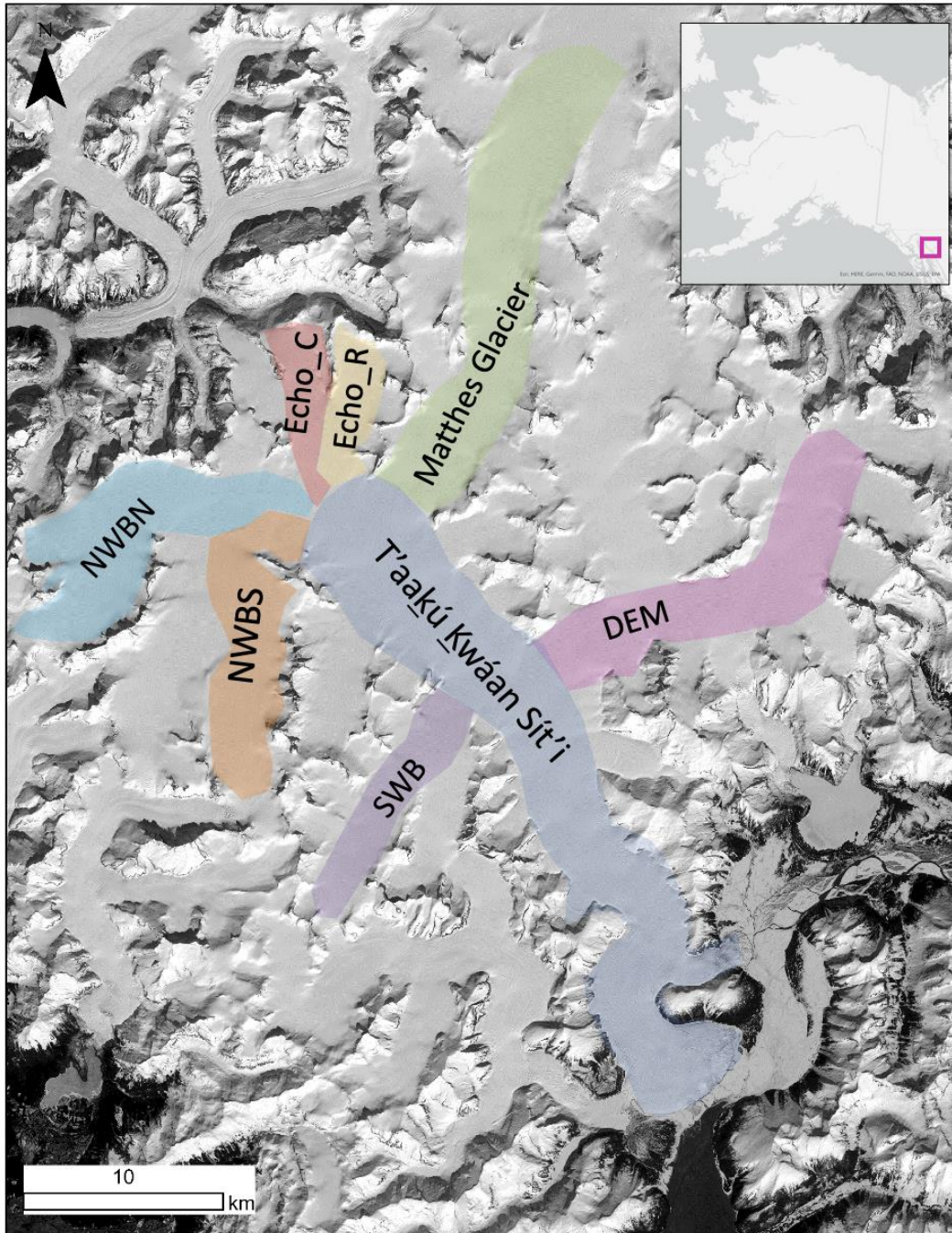
Figure 1.1. Main branches of T'aak̲ú K̲wáan Sít'i, Juneau Icefield (Landsat 8 Imagery Band 8, 04/24/2021). These include Northern-Northwest Branch (NWBN), Southern-Northwest Branch (NWBS), Demorest Glacier (DEM), Southwest Branch (SWB), Matthes Glacier, Echo Glacier-Right (Echo_R), and Echo Glacier-Center (Echo_C).

1.3. Variable Snow Properties and Snow Water Equivalent from Ground-penetrating

Radar across the Juneau Icefield, Alaska (Chapter 2)

Annual accumulation on glaciers and ice sheets is an important input to glacier mass balance and water storage. This accumulation may vary both spatially and temporally in properties including, snow depth, density, liquid water content, and porosity. Such variability is attributed to distance from moisture source, topographic shading, patterns of ablation, avalanching, and wind-redistribution. Quantifying the annual contribution of snowfall to glacier mass balance is typically calculated in terms of snow water equivalent (SWE). Calculating SWE requires knowledge or assumptions of both snow depth and density. It is common to determine snow depth and density with snow mass balance pits. This method, while incredibly specific and potentially representing an elevation band across a study site, only captures discrete point measurements at individual pits.

In contrast, GPR is an effective tool for quantifying winter accumulation depths and other snowpack properties across large lateral distances. It provides a spatially continuous profile of the subsurface and, when used in conjunction with mass balance in-situ measurements, can be used to better quantify SWE variability across a study region. Interpretations of GPR-derived feature depth require assumptions of radio wave velocity. In temperate glaciers such as those of JIF, the radio wave velocity is affected by density and water content (Tuiri and others, 1984; Kovacs, 1994). Because of its sensitivity to the presence of water, GPR has previously been used to discern temperature regimes of glaciers (Campbell and others, 2012a, 2012b) and the presence or absence of water (Campbell and others, 2012a, 2012b; Gerbi and others, 2021). Additionally, from the combination of GPR surveys and extensive ground-truth efforts (via snow pits, or snow and firn cores), it is possible to determine the liquid water content of the snowpack (Tuiri and others, 1984).

GPR has previously been used to quantify SWE on multiple glaciers across Alaska and Western Canada (Campbell, 2014; McGrath and others, 2015; McGrath and others, 2018). The assumption has often been that these SWE surveys were conducted over a dry snowpack and firn. However, recent studies show the presence of water within snow and firn even during winter months across Alaska and Canada (Johnson and Meyer, AGU Abstract 2022). Additionally, on lower elevation glaciers and temperate snowpacks, this "dry" assumption is not valid because melt is observed year-round. Lastly, the timeframe to capture SWE measurements at the end of the accumulation season is quite short meaning that to complete extensive surveys within entirely "dry snowpacks," a large team and optimal weather would be needed to assure successful collection in a short window of time. Snowfall covers approximately half of the northern hemisphere land surface on Earth, annually (Lemke and others, 2007) and SWE estimates across these regions have generally relied on the dry snow assumption. Yet a large percentage of snowfall occurs in temperate environments meaning the dry snow assumption, again, is not likely valid.

During spring and summer months, the temperate JIF snowpack experiences intense ablation and rain-on-snow events resulting in its characteristic wet snowpack with extensive ice lensing. For similar reasons that accumulation depth is variable, it is reasonable to believe the effects of ablation are also spatially and temporally heterogeneous. GPR surveys across JIF must therefore take the variability of liquid water content into consideration for any radargram interpretations, especially concerning the annual accumulation as it is the most susceptible to short-term changes in surface conditions (Clayton, 2019). In chapter 2 of this thesis, I evaluate the combination of extensive GPR survey data from 2012-2021 with ground-truth observations (e.g., snow pit and firn core depth-density measurements) to spatially quantify SWE and spatial variations of density and liquid water content within the snowpack.

1.4. Firn Volume Loss Across the Juneau Icefield, Alaska between 2012 and 2021 (Chapter 3)

Snow that remains after the melt season is referred to as firn. Glacier ice is the product of the densification of snow (100-300 g cm^{-3}) to ice (917 g cm^{-3}). As an input to glacier ice, firn controls mass influx to the glacier. Firn holds both glaciological and ecological importance because of its contribution to glacier ice mass and its capacity to store meltwater during the short-term, ultimately helping to regulate down-glacier runoff (Jansson and others, 2003; Poinar and others, 2019). In temperate and maritime climates, firn typically densifies into glacier ice on a sub-decadal timescale making its persistence year-after-year highly sensitive to short-term climatic conditions. This is in contrast to polar systems where the densification process can take up to hundreds of years because of a lower accumulation rate and less liquid water present in the snow and firnpack (Cuffey and Paterson, 2010).

For snow, or annual accumulation, to go through this densification process, it must still exist at the end of the melt season. This material stage after surviving an ablation season and before densifying into glacier ice, is called firn or neve. Subsequent accumulation seasons will provide an input of fresh snow and, therefore, overburden pressure which aids in the process of firn densification into glacier ice. Percolation of liquid water into the firn will also affect this densification process through the addition of latent heat to the firnpack. If the entire annual snowpack melts during the ablation season, there is no longer an input into the glacier ice, nor any layers insulating the existing firn or glacial ice, putting each at further risk of melt. While firn is actively undergoing processes of densification, there is still pore space where water is able to percolate (before pore close-off depths). So long as there is not a barrier to deeper percolation (e.g., continuous ice lenses), meltwater from the surface is delayed from leaving the englacial system by

occupying the pore space in firn (Culberg and others, 2021). This storage space reduces the rate of down-glacier meltwater flux. Variations in the meltwater flux can have impacts on several of the downstream hydrological and ecological properties including water temperatures, turbidity, and salinity in the area of mixing, and ecological assemblages (Moore and others, 2009; O'Neel and others, 2015). Increased meltwater runoff may highlight important icefield-to-ocean linkages including colder water temperatures, increased turbidity, and decreased salinity in the area of mixing. These important factors are likely to affect micro-to macro scale species within the marine ecosystem, such as phytoplankton and salmonids and especially those that have a narrow range of tolerance (Moore and others, 2009; O'Neel and others, 2015). Therefore, changes in firn extent have implications locally and regionally.

Large firn aquifers have been documented across Greenland, likely buffering Greenland's rapid potential contribution to sea-level rise (Harper and others, 2012). Like Greenland, much of Alaska including JIF also has been observed to maintain firn aquifers. Confirmation of Alaska aquifers includes through satellite observations (Johnson and Meyer, AGU Abstract 2022) as well as GPR surveys (Campbell, 2014) and in-situ firn and ice coring conducted across JIF between 2012-2022 (unpublished). Since retreat began, T'aakú Kwáan Sít'i has also experienced a significant rise in the ELA and likely a thinning of firn across the entire JIF. It is plausible that firn densification rates have also increased. A rise in the ELA, thinning of firn, and more rapid densification rates, each have the potential to significantly impact the health of JIF and down-glacier ecosystems through changing water storage and runoff flux. There is no current published evidence of firn thinning, more rapid densification rates, or changes in meltwater storage for this system. Simply developing a baseline for these properties would be a critical start. In chapter three

of this thesis, I use available GPR and ground-truth observations acquired from across JIF between 2012 and 2021, to estimate firn thickness and volume and differences between study years.

1.5. Common Offset Ground-penetrating Radar (CO GPR)

Common offset ground-penetrating radar (CO GPR) is a powerful tool to understand properties and behavior of the subsurface. Use of GPR in glaciological applications is well-documented and has been used to identify internal reflection horizons with differing electrical properties (e.g. Arcone and others, 1995; Palli, 2003) and to investigate firn stratigraphy (e.g. Arcone, 2002; Campbell and others, 2013; Gascon and others, 2013; Sold and others, 2015). In glacial environments, different electrical properties of these layers may be caused by changes in water content, density, sediment or debris concentration, and chemical composition that impact the relative dielectric permittivity ($\acute{\varepsilon}$) of the material. It is possible to distinguish layers including ice lenses in the snowpack ($\acute{\varepsilon} = 3.15$), the previous year's ablation horizon beneath the annual accumulation, and the transition from firn ($\acute{\varepsilon} = 2.1$-$6$) to glacier ice ($\acute{\varepsilon} = 3.15$). Because ice is not polarized by a magnetic field, the velocity, v, of the radio wave can be expressed in terms of the speed of light, c, and the relative dielectric permittivity, $\acute{\varepsilon}$, by equation 1.1,

$$(1.1) \; v = \frac{c}{\sqrt{\acute{\varepsilon}}} \, .$$

The velocity of a radio wave is therefore affected by the relative permittivity of the layers. I calculate the depth, z, of layers in radargrams using this velocity and two-way travel time (TWTT) to a reflector using equation 1.2,

$$(1.2) \; z = \frac{TWTT * v}{2} \, .$$

In order to determine depth from radio wave velocity, it is necessary to make assumptions about the bulk relative permittivity of a medium (e.g., measuring ice thicknesses generally assume $\acute{\varepsilon} = 3.15$). The relative permittivity of the accumulation and firn layer is influenced on JIF by liquid

11

water content and density. Both increased density and increased water content increase the value of relative permittivity of snow and firn, thus decreasing the radio wave velocity. For temperate glaciers, where both water content and density differences are the primary drivers of a changing relative permittivity especially in the near-surface layers, this assumption is a main limitation and introduces uncertainty into depth calculations.

1.6. Snow Water Equivalent (SWE)

Snow water equivalent (SWE) is a common metric used to assess the annual mass balance of a glacier, water resources, and potential contributions to sea-level rise that relates the depth of snow to the depth of water it would be if it were liquid water. Calculations of SWE derived from ground-penetrating radar rely on the assumption of the bulk radio wave velocity traveling through the snowpack. This assumption introduces uncertainty to these calculations because, in temperate glaciers, the radio wave velocity is affected by density and water content – both properties that exhibit spatial and temporal variability. SWE calculations determine how much water a section of snow, firn, or ice holds – importantly, if it all melted, how much it would individually release into the surrounding environment, potentially contributing to sea-level rise. SWE is calculated by measuring the density (ρ_{snow}) and depth of the snow (z_{snow}) with respect to the density of water (ρ_{water}) via equation (1.3):

$$(1.3)\ SWE = \frac{z_{snow} * \rho_{snow}}{\rho_{water}}$$

SWE can be estimated using snow pits and extrapolating the data at those point measurements across the entire glacier. The downside of the snow pit method is that it is both time and labor intensive and also may miss some of the spatial heterogeneity of the snowpack and over- or underestimate the SWE because these are point measurements. GPR, in conjunction with snow pit analysis, for SWE improves our ability to account for this variability by collecting snow depth

data along track, creating thousands of data points across many kilometers. Together, these methods improve our estimates of SWE.

As previously mentioned, accurate calculations of depth to horizons in radargrams relies on an accurate determination of the radio wave velocity (equations 1, 2). Previous work addresses this limitation through ground-truthing or density-dependent determinations of bulk radio wave velocities or have considered low liquid water content in snow to apply a constant radio wave velocity across study sites (e.g., Gascon and others, 2013; Miège and others, 2013; Sold and others, 2015; McGrath and others, 2018). This method may over or underestimate the true SWE of larger areas or more temperate glacier environments where liquid water is spatially variable. My ultimate goal of chapters 2 and 3 are to contribute to our understanding of spatial and temporal changes in snowpack properties (density and water content) and firn and reduce uncertainties in these variables to better constrain changing snow and firn across Alaska temperate glacier regions.

1.7. Conclusions and Future Work (Chapter 4)

In Chapter 4 of this thesis, I discuss conclusions from the above chapters and the limitations of this thesis which lead into future recommended research.

CHAPTER 2

VARIABLE SNOW PROPERTIES AND SNOW WATER EQUIVALENT FROM

GROUND-PENETRATING RADAR ACROSS THE

JUNEAU ICEFIELD, ALASKA

2.1. Abstract

Quantifying snow accumulation as snow water equivalent (SWE) across large glacier systems is important for improving mass balance and sea-level rise contribution estimates. In North America, there is high uncertainty in current SWE estimates that need to be quantified. It is possible to collect continuous snowpack measurements with ground-penetrating radar (GPR) though interpretations of these data have typically required a necessary assumption of spatially homogenous snowpack properties and associated radio wave velocity for interpretations. I analyzed two years of extensive, repeated ground-penetrating radar (GPR) surveys to assess the spatial and temporal variability of snow properties and accumulation across the Juneau Icefield, Alaska in 2012 and 2021. I use GPR with summer mass balance surveys to calculate snow water equivalent (SWE) values and liquid water content. Results show variability in accumulation depth but relative consistency in patterns of accumulation. Trends in depth-density do not vary outside of the mean density values since the 1950s. Calculated liquid water content ranges from 0-19 percent. Calculated relative permittivity and associated radio wave velocities within the snow across the study site suggest potential for high uncertainty in depth (30.5-54.1 %) and SWE (32.2-56.2 %) due to spatial and, likely, temporal variability in liquid water content when using GPR to determine SWE in this temperate environment. Future work should focus on constraining this spatial and likely temporal variability in liquid water content to better apply GPR to SWE estimates in this region.

2.2. Background

Alaskan mountain glaciers currently account for approximately 20 percent of global contributions to sea-level rise, excluding the Greenland and Antarctic Ice Sheets and thermal expansion of the oceans (Hugonnet and others, 2021; Rounce and others, 2023). Snow water equivalent (SWE) is a common metric used to assess the annual mass balance of a glacier, water resources, and potential contributions to sea-level rise. Estimating the SWE of the annual accumulation requires determining the depth and density of the snowpack. SWE is typically calculated by digging snow pits and extracting depth-density measurements. Measurements from multiple snow pits are then interpolated or extrapolated across the region of interest. SWE across Alaskan glaciers is highly variable (McGrath and others, 2015).

One tool to improve on estimates of SWE across large geographic areas, is the use of GPR. GPR is widely applicable in glaciological contexts and its use is well-documented in determining bed depth and topography, englacial stratigraphy, accumulation and firn depth, and SWE (Arcone and others, 1995; Nolan and others, 1995; Arcone, 2002; Dunse and others, 2009; Campbell and others, 2013; Schroeder, 2023). GPR has previously been used to calculate SWE and functions to extend the spatial scale of studies as users can collect tens to hundreds of kilometers of data in a single field season to account for variability of snow distribution across larger areas (Bradford and others, 2009; McGrath and others, 2015). Calculations of SWE derived from GPR rely on making an assumption of the bulk radio wave velocity traveling through the snowpack to calculate depth (2.1, 2.2). This assumption introduces uncertainty to these calculations because, in temperate glaciers, the radio wave velocity is affected by density and water content – both properties that exhibit spatial and temporal variability. Understanding how density and liquid water content vary spatially is crucial to interpretations of depth from GPR-derived measurements.

The Juneau Icefield (JIF), one of Alaska's largest icefields, is currently shrinking and losing mass much like most other glacier systems across Alaska (Larsen and others, 2015; Berthier and others, 2018; McNeil and others, 2020). JIF spans from the northern Pacific Coastal Temperate Rainforest to higher, inland elevations, and exists in a maritime climate (O'Neel and others, 2015; Pelto and others, 2013). Due to the establishment of field stations across JIF since the 1950s, this area provides an opportunity to study variations in snow properties across a large spatial area (e.g., Connor, 2009; Pelto and others, 2013). Annually, JIF receives approximately 3-4 m water equivalent (w.e.) and modeled precipitation patterns indicate that the precipitation varies between 2.5-4.4 m w.e. (Pelto and others, 2013; Roth and others, 2018). On JIF, up to 18 snow pits are dug annually on T'aakú Kwáan Sít'i and are used to calculate SWE over an area of 671 km^2 (Pelto and Miller, 1990).

Because JIF is a temperate glacial system existing at the pressure melting point throughout the ice, it is sensitive to changes in atmospheric temperature. Melt is especially prevalent during the summer months of June, July, and August (JJA) with supraglacial melt ponds and streams observed in the accumulation zone. Melt and refreeze cycles throughout the year are recorded in the annual snowpack as continuous and discontinuous ice lenses observable in snow pits or in ground-penetrating radar (GPR) surveys. T'aakú Kwáan Sít'i (the T'aakú peoples' glacier, Taku Glacier) is the main drainage for the southern portion of the Juneau Icefield and has an area of 671 km^2 (Pelto and others, 2013). There are several branches that flow into T'aakú Kwáan Sít'i, including Matthes Glacier, Echo Glacier, Northern-Northwest Branch, Southern-Northwest Branch, Southwest Branch, and Demorest Glacier (Fig. 2.1). T'aakú Kwáan Sít'i was one of the last glaciers in this region to stop advancing (Criscitiello and others, 2010; McNeil and others, 2020). T'aakú Kwáan Sít'i is a tidewater glacier that is protected by a substantial thrust moraine of

eroded sediment. However, between 1989 to 2018, the equilibrium line altitude rose from 1115 m

a.s.l. to 1308 m a.s.l., resulting in a decreased accumulation area ratio (0.85 to 0.57) and between

2013-2018, the glacier terminus retreated ~59 m (McNeil and others, 2020). Because

T'aaḵú Ḵwáan Sít'i lies in an over-deepened bed, if retreat continues, the thrust moraine is eroded,

or a terminal lake develops, the glacier becomes more susceptible to enhanced melt with the

erosion of the terminal moraine and marine intrusion (Nolan and others, 1995; Zechmann and

others, 2020). Since T'aaḵú Ḵwáan Sít'i is the main drainage of this portion of the icefield and

spans a range of elevations, its changes are largely indicative of the health of JIF.

By constraining snow properties such as snow density and water content as it relates to

relative permittivity, uncertainties related to estimates of SWE can be reduced when calculating

annual accumulation on JIF. Here, I utilize GPR in conjunction with snow pit measurements to

further constrain SWE estimates. Depth and density data from numerous snow pits across JIF from

2012 and 2021 are used to better inform interpretations of extensive, repeated 400 MHz GPR

surveys to calculate SWE and to quantify the variability in liquid water content across the study

site.

2.3. Methods

2.3.1. Snow Pits

In 2012 and 2021, the Juneau Icefield Research Program extracted 18 and 13 summer mass balance

pits, respectively, as part of its long-standing mass balance program (Pelto and others, 2013). Mass

balance pits were dug through the annual accumulation layer to the previous summer surface, top

of the firn layer, or to blue ice. Typically, snow pit depths reached between 3-5 m. Depth-density

measurements were sampled from the north-facing wall at each pit at 10 cm intervals using a 500

cm^3 sampling cylinder. Any observable ice lenses or ice pipes through the snowpack were

recorded. Density data collected from all snow pits during respective years were collated and then averaged across each 10 cm depth interval to yield the average and standard deviations of density with depth across JIF. After plotting the depth versus density of snow, an exponential line of best fit equation was fitted to the data to provide an estimate of density with depth across JIF. This method is repeated each study year for all the snow pits on JIF with all available data including that from Llewellyn and Lemon Creek Glaciers.

2.3.2. Ground-penetrating Radar

2.3.2.1. Field Collection To determine the spatial variability of snowpack depth, I analyzed approximately 150 km of GPR surveys across JIF in July 2012 and that were repeated in July 2021 (Fig. 2.a). These used a Geophysical Survey Systems Incorporated (GSSI) SIR-3000 control unit in 2012 and a GSSI SIR-4000 control unit in 2021 coupled with a GSSI model 5103 400 MHz antenna. Surveys were conducted using snow machines and towing the antenna on a sled at speeds of 3-7 km h^{-1}. In 2021, the SIR-4000 was directly linked to a Garmin GPSMap78 handheld GPS for georeferencing. I georeferenced the 2012 data by relating GPS points recorded every 50 meters on a Garmin GPSMap 62stc to the associated markers recorded in the radar profiles. I estimate horizontal positional error of $\pm$ 3 m. These transects were collected along the centerline of each glacier and radar lines spanned from below to above the equilibrium line altitude and passed adjacent to the mass balance pits across JIF. Additionally, several cross sections were surveyed. Data were collected with a time window of 250-400 ns, 2048 samples per scan, and 24 scans per second.
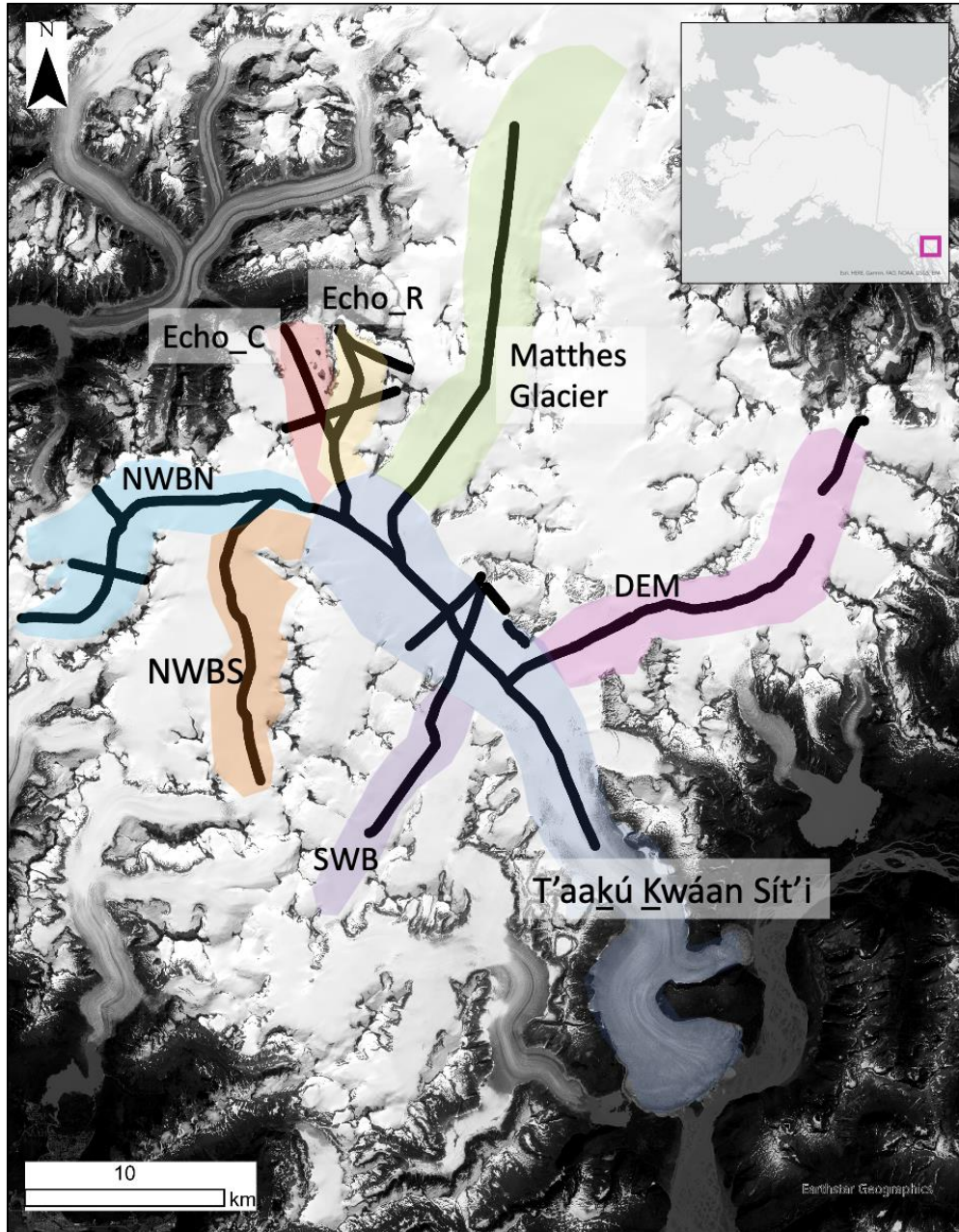
Figure 2.1. Main branches of T'aaḵú Ḵwáan Sít'i, Juneau Icefield (Landsat 8 Imagery Band 8).

These include Northern-Northwest Branch (NWBN), Southern-Northwest Branch (NWBS),

Demorest Glacier (DEM), Southwest Branch (SWB), Matthes Glacier, Echo Glacier-Right

(Echo_R), and Echo Glacier-Center (Echo_C).

2.3.2.2. Post-Processing Using GSSI's proprietary software, RADAN version 7, all GPR profiles were time-zero corrected, distance normalized, and stacked. Additionally, some profiles were filtered with a low pass of 800 MHz and a high pass of 100 MHz if there was noise apparent in the radargrams. The 2012 profiles were distance normalized as a result of the GPS reference method. The 2021 profiles were distance normalized using readgssi, an open-source python package (https://github.com/iannesbitt/readgssi.git). The annual accumulation and firn boundary is identified as the most spatially-continuous horizontal reflection horizon and was observed cross-cutting several upcutting firn layers in some profiles. From each GPR transect, two-way travel time (TWTT) data are converted to depth beneath the snow surface. From independent picks from multiple individuals and the vertical resolution of this antenna, I estimate an uncertainty in picked horizons to be 0.1 m.

In order to compare the same spatial extent of the GPR transects for 2012 and 2021, an Inverse Distance Weighted interpolation was performed with respect to the 3 nearest points. This interpolation method balances spatial correlation between points and computational load by weighting points closer to the interpolated point more than those farther away. Direct comparisons between years are computed with these data across a shared spatial extent.

2.3.2.3. Ground truth efforts To convert the GPR data from TWTT (ns) to depth (z), an assumption is made for the value for bulk average velocity of the radio wave (v) through the snowpack, which is then used to calculate depth with Equation 2.1,

$$(2.1)\ z = \frac{TWTT * v}{2}$$

and velocity is defined with Equation 2.2 where c is the speed of light (0.3 m ns[-1]) and $\acute{\varepsilon}$ is relative permittivity.

$$(2.2)\ v = \frac{c}{\sqrt{\acute{\varepsilon}}}$$
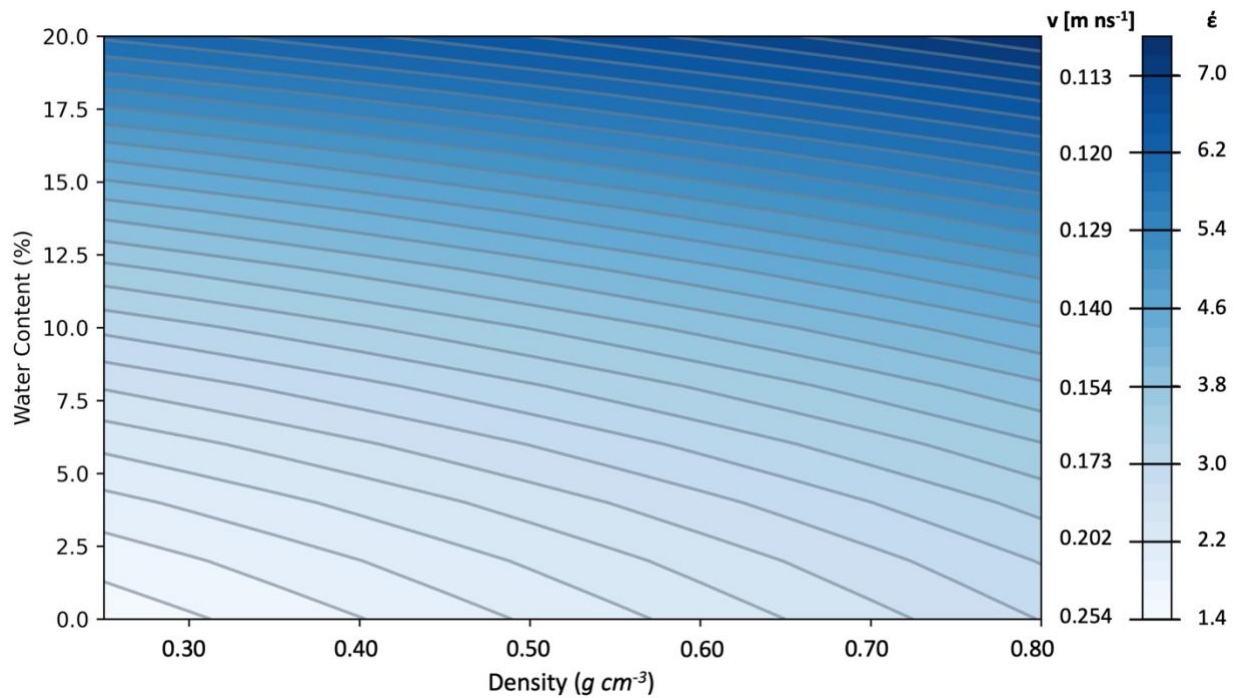
Figure 2.2. Comparison of water content (%) and snow density (g cm⁻³) where colors represent relative permittivity ($\acute{\epsilon}$) and radio wave velocity (v) variations. This plot is based on empirical relationships presented in Tiuri and others (1984).

The radio wave velocity is controlled by the relative permittivity of the snowpack. In a temperate glacier environment such as JIF, the relative permittivity is determined by the density and water content of the snow (Kovacs and others, 1995). The relationship between density, water content, and relative permittivity is shown in Fig. 2.2 and is based on the empirical relationships presented in Tiuri and others (1984) and Sihvola and Tiuri (1986).

To determine how the density and water content vary across JIF, the mass balance pits and several additional shallow (3-5 m) snow cores were collected using a Kovacs corer. This provides an additional ground-truth accumulation depth measurement used to convert TWTT to depth. Ground-truthing was necessary to determine in-situ depth of annual snow accumulation, z, and to

use these measurements to improve assumptions of relative permittivity (έ) and, thus, radio wave velocity. έ was calculated at each ground truth point by combining and rearranging equations 2.1 and 2.2, where c is the speed of light (0.3 m ns^{-1}) (2.3).

$$(2.3)\ έ = (\frac{c*TWTT}{2z})^2$$

The range of radio wave velocities calculated from Equation 2.3 are used as bounds for TWTT-depth conversions. Snow depths are calculated using the mean, minimum, and maximum relative permittivity each year to provide a range of depths which represent the upper and lower potential limits of the snowpack depth.

Generally, ground-truth data were collected on the same day as radar surveys. Because of the time required to excavate some pits (up to 7.1 m deep), any ground-truth data collected 1-2 days before or after surveying, required calculating a simple linear regression ablation rate. I excluded ground-truth data from any snow pits collected more than 3 days after corresponding radar surveys if sufficient ablation rate data were lacking. To reconcile the difference in temporal coherence between radar collection days and snow pit collection days, I used a simple ablation calculation. At 3 snow pit locations, TKG3, TKG5, and TKG7 along the centerline of T'aak̲ú K̲wáan Sít'i, ablation stakes were deployed for several days during July 2012. I calculated an average rate of ablation across those days by dividing the change in surface height by the number of days the stakes were left out. For the pit locations, TKG3, TKG5, and TKG7, where the temporal coherence between radar and snow pit collection was +/- 1 day, this simple average ablation was applied to the recorded snowpit values. For days when the radar was collected before the pit (i.e., the depth to the bottom of the annual accumulation was greater during radar collection than in snow pit collection), the ablation rate was applied in the opposite direction (+ accumulation). For example, if the pit were measured to be 400 cm deep the day after radar was collected with an

ablation rate of 5 cm per day, the value used for radiowave velocity calculations was 405 cm. The opposite is true for days when radar data were collected following the day of snowpit collection. For the two ground-truth sites that did not have ablation stakes near them, SWB1 and SWB2, ablation rates were calculated using the closest stake correlating with elevation or proximity to stake. For sites where the temporal coherence was greater than 3 days, I dropped these cases from the ground-truth analysis because I was unable to reliably rectify the ablation in these areas. This coherence was less of an issue for the 2021 dataset, where the main outlier was site MG2 with the lag in collection times was 14 days. This difference could not be reliably rectified either, and this case was dropped from the ground-truth analysis.

2.3.3. Snow Water Equivalent

SWE across JIF was calculated by integrating the equation for line of best fit for the combined pit data density profile, (z), (Section 2.3.1.) with respect to depth from zero (surface) to the depth of the annual accumulation, z, to capture the density differences throughout the snow column (Section 2.3.2.). Equation 2.4 represents the general equation structure. For the respective years, SWE was calculated under the following scenarios: mean, minimum (maximum radio wave velocity and depth), and maximum (minimum radio wave velocity and depth) relative permittivity to provide bounds for the range of observed conditions.

$$(2.4) \; SWE = \int_0^z \rho(z) \, dz$$

2.3.4. Liquid Water Content

The liquid water content of the snowpack was calculated at each ground truth point using the empirical relationship between density (ρ_d), water content (W), and relative permittivity of dry, wet, and measured snow ($\acute{\varepsilon}_d$, $\acute{\varepsilon}_w$, $\acute{\varepsilon}_s$) derived in Tuiri and others, 1984 (2.5, 2.6).

$$(2.5) \; \acute{\varepsilon}_d = 1 + 1.7\rho_d + 0.7{\rho_d}^2$$

$$(2.6) \quad \acute{\varepsilon}_s = (0.10W + 0.80W^2)\acute{\varepsilon}_w + \acute{\varepsilon}_d$$

The value for snow density (ρ_d) was averaged at each individual pit from the mass balance depth-density profiles in each year. The values for $\acute{\varepsilon}_s$ were calculated in Section 2.3.2. for each ground truth point. I solve for liquid water content, W, at each pit with bounds of average density ± 1 standard deviation and use a value of 88 for $\acute{\varepsilon}_w$.

2.4. Results

2.4.1. Snow Pits

The annual accumulation layer of the summer mass balance pits reached a maximum depth of 7.10 m in 2012 and 5.80 m in 2021. The average annual layer depths were 5.52 (± 0.94 m) and 4.22 ($\pm$ 0.88 m) for 2012 and 2021, respectively. Overall, there were a total of 18 pits in 2012 and 13 pits in 2021. The mean density of samples for all snow pits was 0.556 g cm^{-3} (± 0.030 g cm^{-3}) and 0.562 g cm^{-3} (± 0.025 g cm^{-3}) for 2012 and 2021, respectively. Within the annual snowpack, both continuous and discontinuous ice lenses were observed with most 0.5-1.5 cm thick and rare cases as thick as 3-8 cm. The density of samples follows the expected trend of increasing density with depth (Fig. 2.3). Equations describing the relationship between density and depth for each year are $\rho_{2012}(z)=0.40278z^{0.05668}$ ($R^2=0.855$) and $\rho_{2021}(z)=0.44984z^{0.04089}$ ($R^2=0.663$).
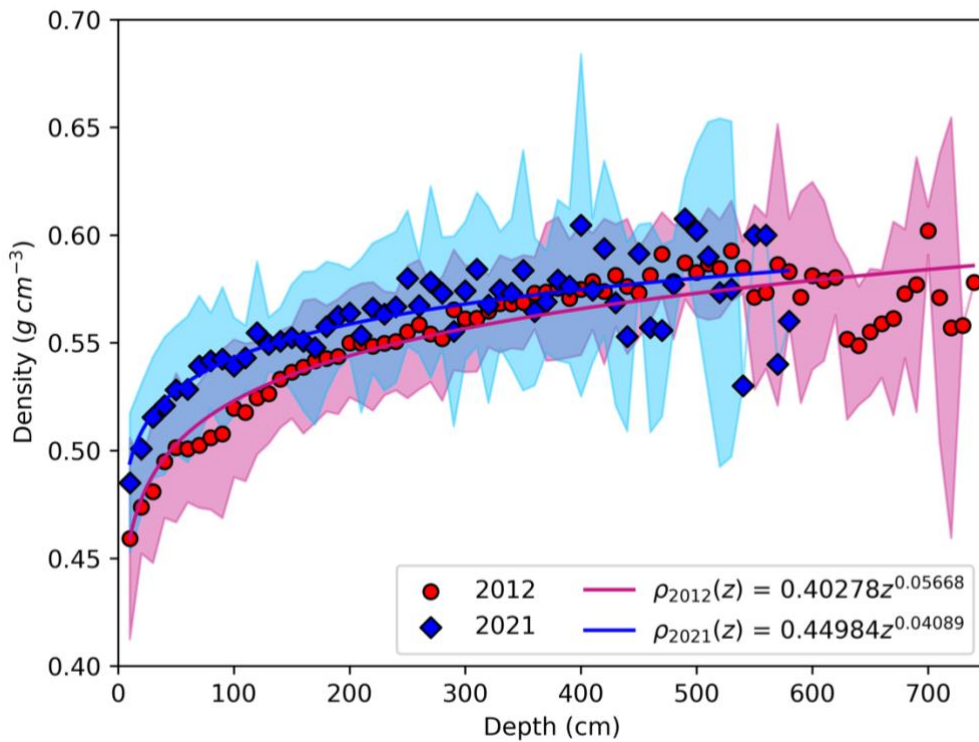
Figure 2.3. Average snow densities shown at 10 cm intervals for summer mass balance pits in 2012 (red circles) and 2021 (blue diamonds). A line of best fit is included for each data set with envelopes representing one standard deviation from the mean for each year.

2.4.2. Ground-penetrating Radar

I identify the annual accumulation (AA), firn-ice transition (F-I), and firn (F) in radargrams from 2012 and 2021 (Fig. 2.4). In 2012, annual accumulation depths ranged between 2.38 m and 12.0 m with a mean of 5.46 m (s.d. = 1.60 m). For these calculations, I used the average value of calculated relative permittivity of 2.28 and applied this to the entire dataset for this year. In 2021, accumulation depths ranged between 0.60 m to 9.88 m with a mean of 3.45 m (s.d. = 1.44 m) and an average relative permittivity of 3.66 applied across the dataset. I include the range of calculated annual accumulation depths when assuming different relative permittivity values in Table 2.1.
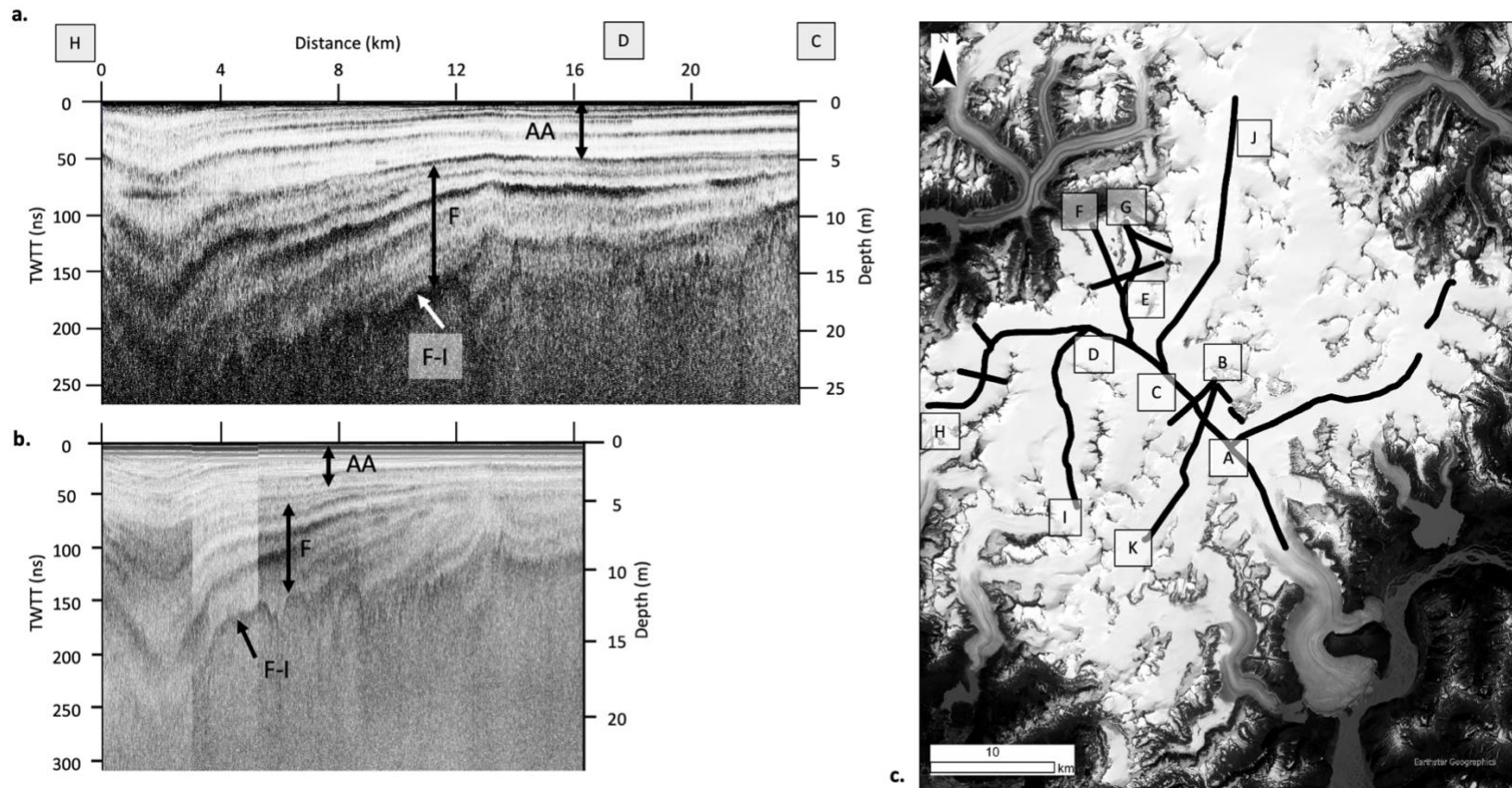
Figure 2.4. 400 MHz radargrams from repeated sections of Northern-Northwest Branch in (a.) 2012 and (b.) 2021. Depth displayed with each year is calculated with the average relative permittivity of 2.28 and 3.66 for 2012 and 2021, respectively, from ground truth points. Interpretations of the annual accumulation (AA) horizon, firn (F) layers, and the firn-ice (F-I) interface are displayed. (c.) Reference map for survey locations.

	Mean Depth (m)			Total Range in Depths across JIF (m)		
Year/$\acute{\varepsilon}$	z_{Min} ($\acute{\varepsilon}_{max}$)	z_{Mean} ($\acute{\varepsilon}_{avg}$)	z_{Max} ($\acute{\varepsilon}_{min}$)	Min ($\acute{\varepsilon}_{max}$)	Mean ($\acute{\varepsilon}_{avg}$)	Max ($\acute{\varepsilon}_{min}$)
2012	5.19 (2.62)	5.55 (2.28)	7.06 (1.42)	1.50 - 11.3	2.38 - 12.0	2.04 - 15.3
2021	2.74 (6.31)	3.59 (3.66)	4.77 (2.08)	0.46 - 7.52	0.60 - 9.88	0.80 - 13.1

Table 2.1 Comparing the range of GPR-derived annual-accumulation depths for 2012 and 2021 based on the mean, high, and low values for calculated relative permittivity ($\acute{\varepsilon}$) for the 150 km of radar transects.

2.4.2.1. Ground Truth of Relative Permittivity and Snow Thickness A total of eighteen snow pits or snow cores were extracted as ground truth points (8 from 2012 and 10 from 2021) were collected in less than 3 days of corresponding GPR surveys and used for calculating relative permittivity values. I estimate ~11.25-14.52 cm of uncertainty from the maximum of 3 days surface melt due to local ablation rates measured from local ablation stakes. I excluded 6 ground truth points that were measured more than 3 days after radar collection. For 2012, the maximum, mean, and minimum relative permittivity values were 2.62, 2.28, and 1.42, respectively. For 2021, these values were 6.31, 3.66, and 2.08, respectively. These values correspond with radio wave velocity ranges of 0.252-0.185 m ns^{-1} in 2012 and 0.208-0.119 m ns^{-1} in 2021. There is no dominant spatial trend observed in these values (Fig. 2.5).

2.4.3. Snow Water Equivalent

In 2012 and 2021, I found that areas closer to the coast had higher SWE values which, increased with increasing elevation. SWE values were amongst the highest across JIF on the Northern Northwest Branch, Southern Northwest Branch, and Southwest Branch and ranged between 201-686 cm w.e. and 100-566 cm w.e. across these branches for the respective average calculated relative permittivity of 2.28 (2012) and 3.66 (2021) (Fig. 2.6). More inland, the relative increase in SWE with elevation is less apparent in 2021 than in 2012 (Table 2.3). SWE values increase 200-280 cm w.e. from lower elevation on T'aakú Kwáan Sít'i to higher elevation on Matthes Glacier. Low values of SWE are observed closer to the terminus of T'aakú Kwáan Sít'i, on both branches in Echo Basin, and on Demorest Glacier. In general, SWE values were higher in 2012 than in 2021 where the mean SWE, calculated with the mean relative permittivity for each year, was 106 cm w.e. greater in 2012 than in 2021. These trends remain consistent across all calculated SWE values, even with the range of relative permittivity values observed with all 2021 values over 100 cm w.e. lower than the same time in 2012 (Table 2.2). The mean difference between years for each of the individual branches ranged between 59 cm w.e. (NWBS) and 133 cm w.e. (Matthes-Taku) (Table 2.3).
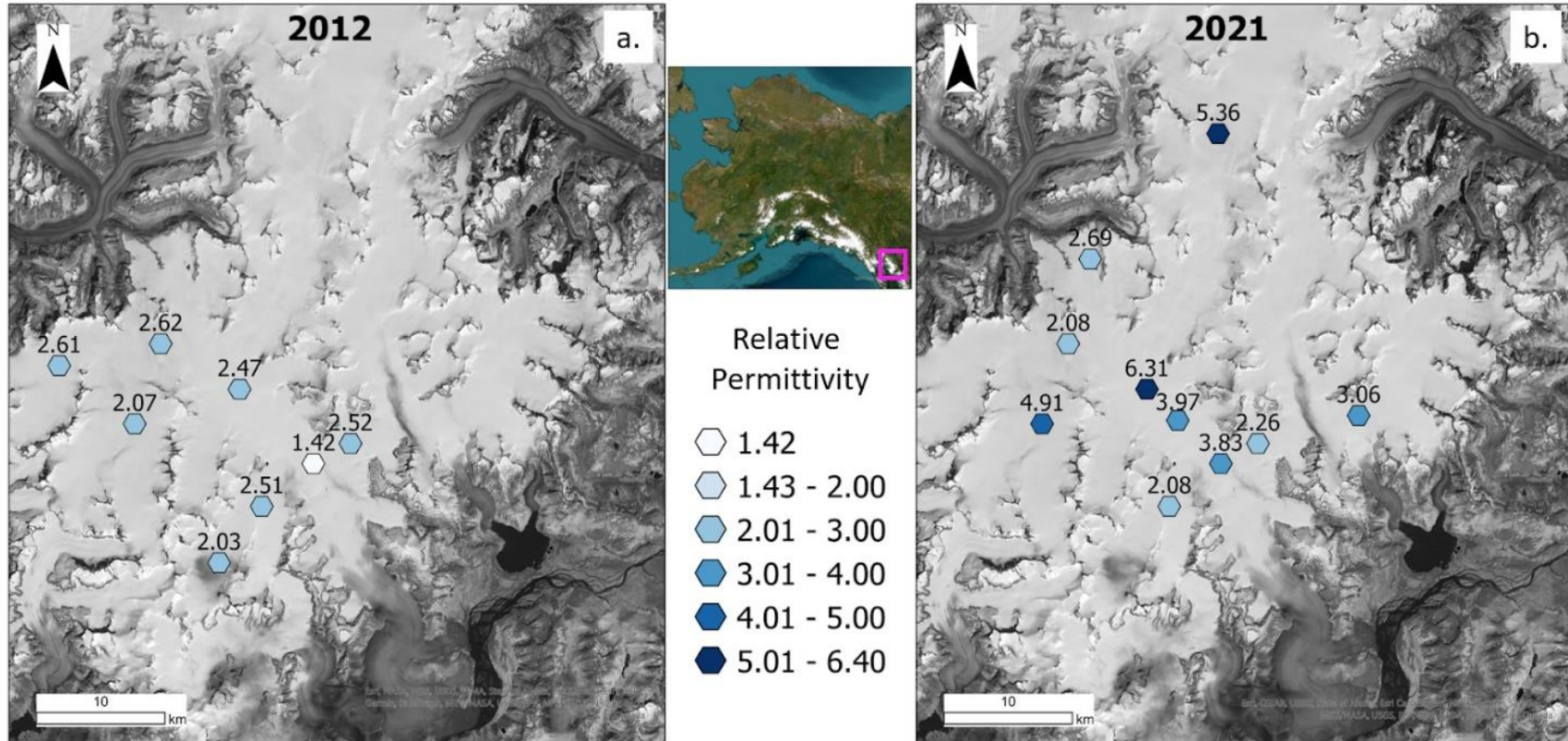
Figure 2.5. Calculated relative permittivity values in (a) 2012 and (b) 2021 for each ground truth point. Locations of ground-truth points are represented by hexagons shaded in colors corresponding with relative permittivity values.
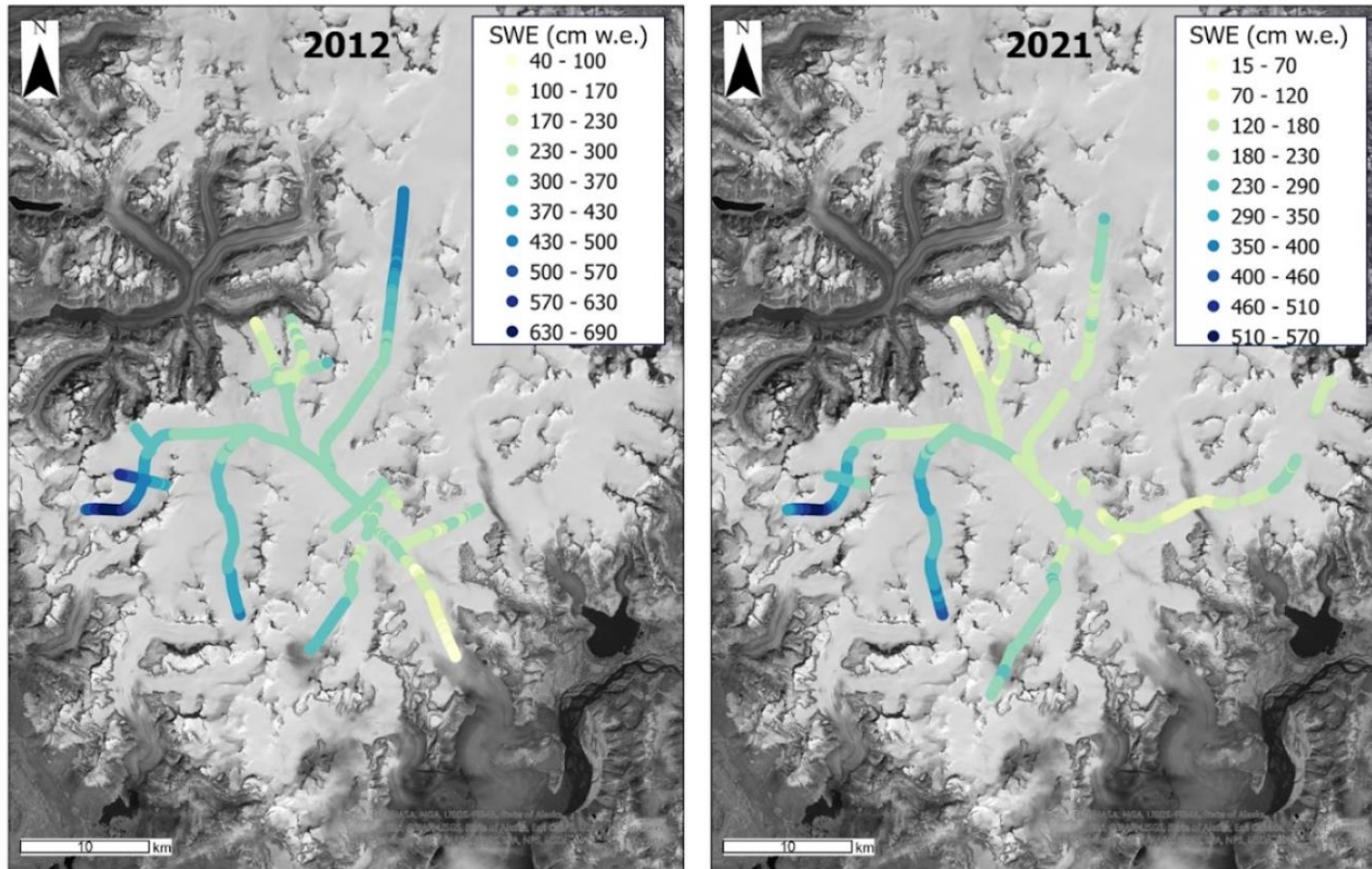
Figure 2.6. Snow water equivalent (SWE) estimates for (a) 2012 and (b) 2021, based upon the mean calculated relative permittivity for 2012 (2.28) and 2021 (3.66). Lower values in SWE are displayed in light yellows with increasing values of SWE in darker shades of blue. Note the difference in SWE scale between (a) and (b). Landsat 8 (Band 8) imagery shows snow-covered glaciers in white and bedrock in gray, with the exception of Taku terminus (blue ice, gray color) and medial moraines.

Year/έ	Mean SWE (cm w.e.) across JIF			Total Range in SWE (cm w.e.) across JIF		
	SWE_{Min} ($έ_{max}$)	SWE_{Mean} ($έ_{avg}$)	SWE_{Max} ($έ_{min}$)	SWE_{Min} ($έ_{max}$)	SWE_{Mean} ($έ_{avg}$)	SWE_{Max} ($έ_{min}$)
2012	283 (2.61)	304 (2.28)	391 (1.41)	115 – 639 (2.61)	124 – 686 (2.28)	159 – 884 (1.41)
2021	149 (6.31)	198 (3.66)	266 (2.08)	23 – 426 (6.31)	30 – 566 (3.66)	41 – 759 (2.08)

Table 2.2. Comparison of the range of annual-accumulation snow water equivalent (SWE) for 2012 and 2021 based on the mean, high, and low values for calculated relative permittivity (έ) for the shared extent of radar surveys. Note the inverse relationship between έ with velocity and depth.

	2012		2021	
Main Branches	Mean (cm w.e.)	Range (cm w.e.)	Mean (cm w.e.)	Range (cm w.e.)
Demorest	233	130 - 251	119	93 - 132
SWB	270	201 - 339	186	100 - 237
Echo - Center	201	123 - 265	94	59 - 134
Echo - Right	233	188 - 282	137	110 - 198
Matthes - Taku	298	182 - 461	165	31 - 233
NWBS	319	232 - 480	260	145 - 458
NWBN	397	247 - 686	274	146 - 566

Table 2.3. Mean and range of snow water equivalent values (SWE, cm w.e.) by years and respective branches listed in order of ascending mean elevation for the shared survey extent.

2.4.4. Liquid Water Content

Calculated liquid water content varied between 0-19%. in 2021 and 0-5.2 percent in 2012 across the study site (Fig. 2.7). The liquid water content was not consistent between years, nor was there a consistent trend (increase/decrease) at the same locations. Of the five locations with liquid water calculations in both 2012 and 2021, three of them (TKG5, TKG3, C161) experienced an increase in liquid water content at the time of surveys while the other two (DG1, TKG7) experienced a decrease. In 2012, there does appear to be a trend of increasing liquid water content with elevation. There is not a similar trend in 2021.
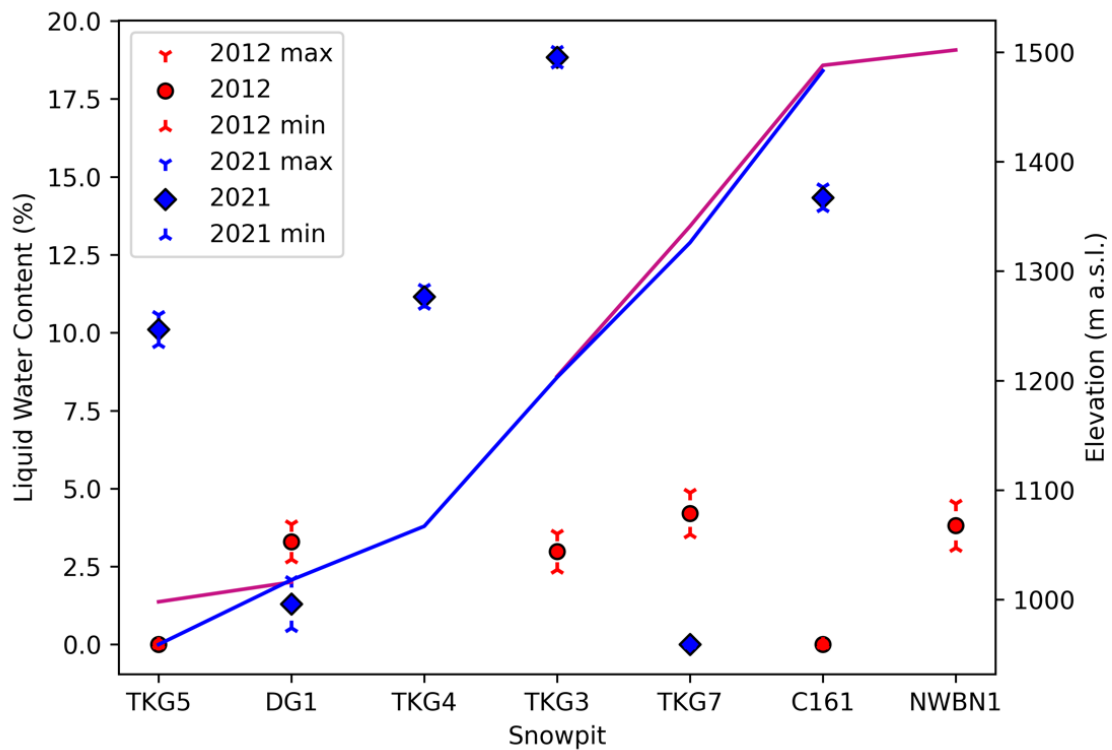
Figure 2.7. Calculated of liquid water content (LWC, %) at each snowpit site and elevation (m a.s.l.) for 2012 (red circles, red line) and 2021 (blue diamonds, blue line). Range of potential LWC noted with carets calculated with one standard deviation of density.

32

2.5. Discussion

2.5.1. Annual Accumulation Depth and SWE

I present depths and SWE to encompass the range of values possible from GPR surveys depending on the snow conditions when they were surveyed. Consistent throughout the survey, I observed patterns in snow depth and SWE that are likely a result of climatological and topographical factors such as elevation and proximity to a moisture source (Maurer and others, in review). I observe an inverse relationship between distance from the ocean and snow accumulation depth and SWE. These trends are most notable for marine proximal (coastal) branches of JIF. Specifically, the Northern Northwest Branch, Southern Northwest Branch, and Southwest Branch had consistently higher snow depths and SWE than more interior glaciers that were surveyed on JIF. While this study does not include temperature and precipitation directly, other studies have shown a relationship between temperature and precipitation and SWE (Hamlet and others, 2005).

Elevation is an important factor for SWE values and I observe generally higher values of SWE at elevations above 1500 m a.s.l. (Fig. 2.8). The impact of elevation may be amplified for marine-proximal glaciers where the high elevation areas are also those closest to the coast, thereby naturally receiving more precipitation than JIF regions distal from the coast. There is a divergence of normalized SWE on Matthes-Taku where there are much higher values at ~1500-1800 m a.s.l. in 2012 than there are in 2021. It is unclear what causes this divergence, but suspect variations in dominant wind patterns or ablation between 2012 and 2021 may have contributed to this divergence.
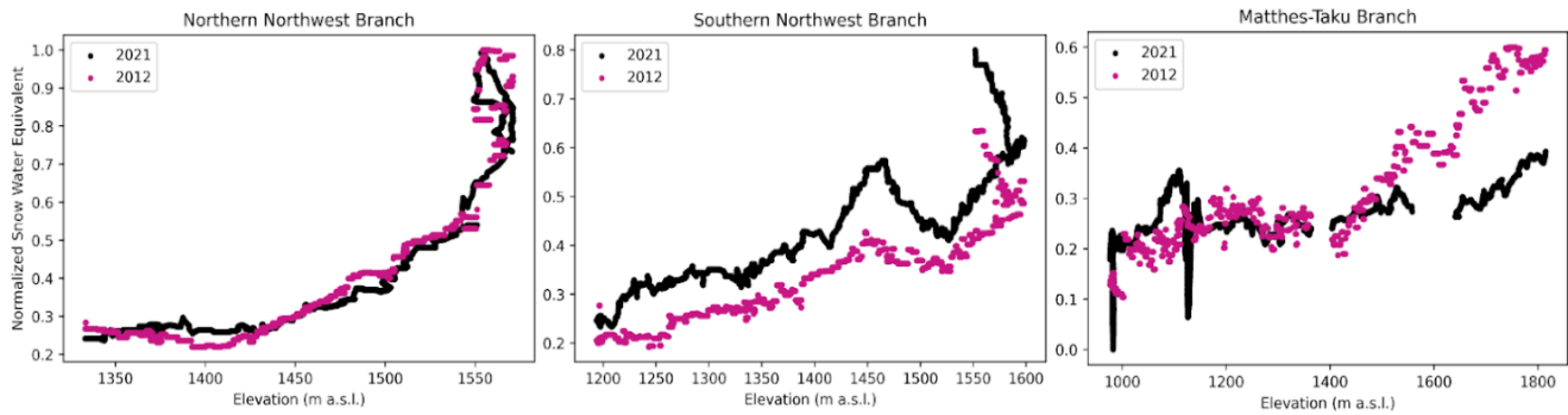
Figure 2.8. Normalized SWE values [0, 1] for (a) Northern Northwest Branch, (b) Southern Northwest Branch, and (c) Matthes-Taku

Branch for 2012 (pink) and 2021 (black). Values are plotted against surface elevation (m a.s.l.). Note the difference in scale for the

normalized SWE values (a-c)

2.5.2. Variability in Relative Permittivity

I attribute the range of calculated relative permittivity in 2012 and 2021 to liquid water content within the snowpack. Water has a relative permittivity of 80-88 (88 for water close to the freezing point, which is therefore used in these calculations) compared to dry snow (1.4-2.2). Water results in strong scattering when interacting with radio waves. These depth-density results fall within the expected variability in density previously measured at this location (LaChappelle, 1954; Pelto and Miller, 1990). Because differences in relative permittivity in this glaciological context are due to differences in density and water content, depth-density trends follow a similar pattern and are relatively consistent, and the process of densification takes (weeks to months) longer than the process of meltwater production and percolation through snow (hours to days), I conclude that this variability must be due to spatial variability in water content. Given such high spatial variability, I conclude that there is also likely substantial temporal variability of meltwater in this temperate snowpack, as observed in other studies in the Swiss Alps and Western Norway (Techel and Pielmeier, 2011; Hart and others, 2011). This variability is likely representative of JIF snowpack during the summer months with high ablation and rain-on-snow events.

GPR is a useful tool to rapidly extend point-based measurements across large spatial extents (10s to 100s of kms) of SWE in a non-destructive manner. However, GPR users must be cautious with annual accumulation estimates because assumptions about radio wave velocity and relative permittivity are necessary for depth-based measurements of snow in a temperate glacial or snow-covered environment.

Calculating depth from the calculated relative permittivity leads to differences in interpreted depths of up to 30.5 percent in 2012 and 54.1 percent in 2021. These differences introduce substantial uncertainty into SWE calculations (32.2-56.2 percent) by GPR (Fig. 2.9). To
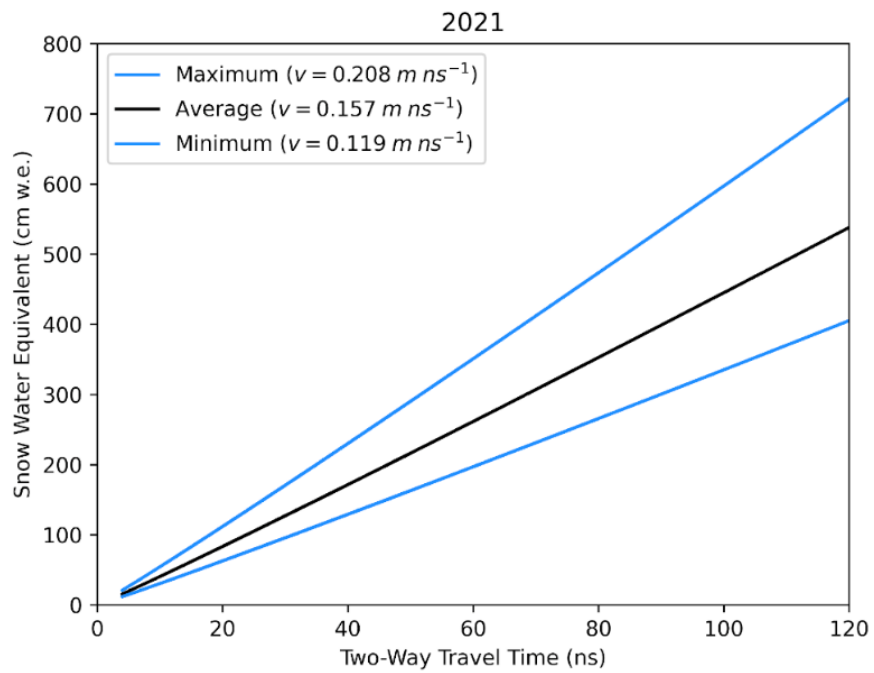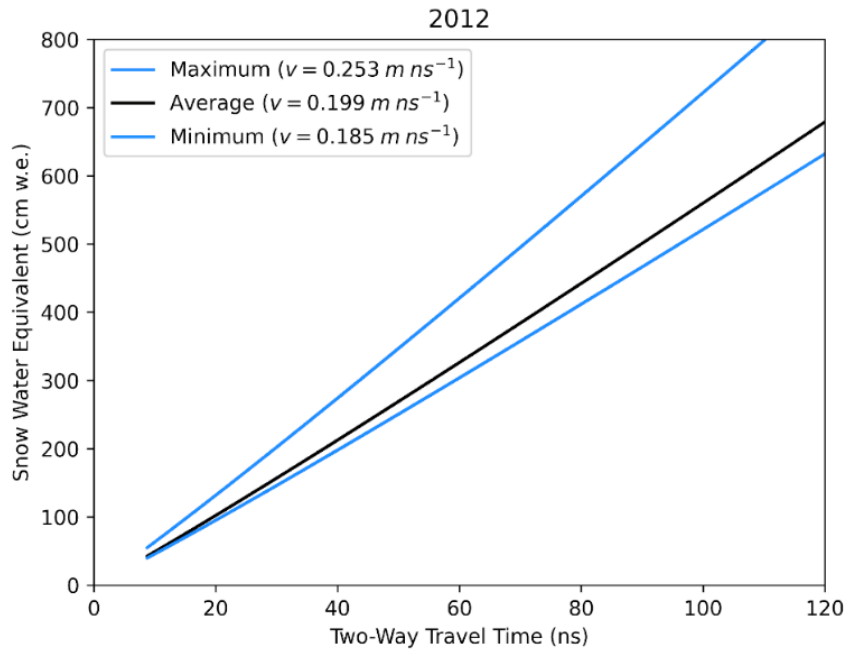
Figure 2.9. Range of possible SWE values based on the range of relative permittivity calculated

for (a) 2012 and (b) 2021.
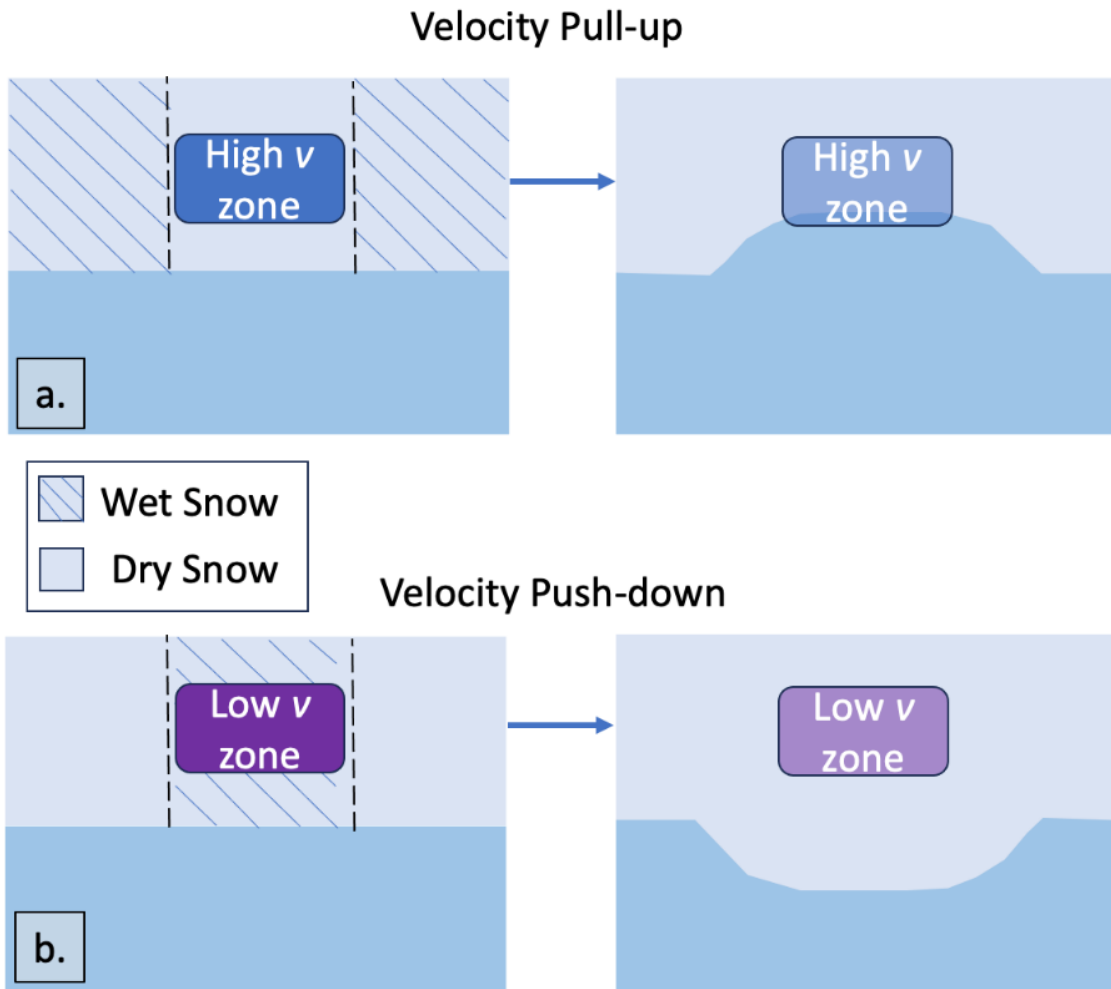
Figure 2.10. Schematic representation of the effect of low and high velocity zones on the appearance of layers in radargrams resulting in (a) velocity pull-up or (b) velocity push-down.

remedy this situation, I recommend ground-truth points via snow pits or coring at least at the end-point of GPR surveys and potentially in the middle of survey lines if there are substantial changes in topography along the transect, such as more than 300 m of elevation change, rolling topography, or sudden increases or decreases in wind shading. Examples of factors which may spatially and temporally influence snowpack relative permittivity include (but are not limited to) elevation change, aspect, and solar barriers such as nunataks (which may shield the sun and reduce melt).

2.5.3. Liquid Water Content

The calculated liquid water content values from these GPR surveys coupled with depth-density measurements are variable spatially and temporally, ranging between 0 and 19% of the total volume. This variability in liquid water content may impact interpretations of layer depths where incidences of wet/dry snow create a low/high velocity zone resulting in artificially lowered/raised horizons (Fig. 2.10). At TKG3, TKG4, TKG5, and C161 in 2021, the percent liquid water content is greater than the typical range of 0-9 percent water content observed in other temperate snow studies (Colbeck, 1973; Fountain 1989; Arcone, 2002; Techel and Pielmeier, 2011). However, Arcone (2002) points out that his study suggests the dominant water control is via imbibition and Colbeck (1973) points out that there is still significant pore volume space available for meltwater storage in snowpack. Pore space in dry snow can be estimated by reorganizing the following observed equation 2.7 (DeWalle and Rango, 2009),

$$(2.7) \; \rho_s = \rho_i(1 - \phi) + \rho_w \phi S_w$$

where:

ρ_s = density of the snowpack (kg m^{-3})

ρ_i = density of ice (917 kg m^{-3})

ρ_w = density of liquid water (1000 kg m^{-3})

ϕ = porosity of snowpack (m^3 of pore space per m^3 of snowpack volume)

S_w = water saturation (m^3 of liquid water per m^3 of pore space)

In the case of dry snow, the second term cancels leaving an easy estimate of snow porosity:

$$(2.8)\ \rho_s = \rho_i(1 - \phi)$$

The average density of snow across JIF during these study years is roughly 558 kg m^{-3} which results in an estimate of 39% porosity. This value would leave plenty of room to accommodate the maximum estimated meltwater calculated here. Assuming the maximum water content observed via combined GPR and ground-truth methods is 20%, I estimate 50% porosity, again easily accommodating the meltwater I calculated. This said, while we have carefully measured meltwater content via snow pits and GPR to extend point measurements into a spatially continuous dataset, future work could include in-situ measurements of meltwater content in the snowpack via methods such as a snow fork coupled with density measurements. This said, these values are within the range of standard literature so I can use this porosity derivation to calculate a first-order estimate of total potential water storage across JIF by integrating porosity across the total glacier watershed and thickness of the snowpack.

The high water content values I calculated suggest that water storage on JIF in many cases is far greater than that accounted for solely via imbibition. It is likely that the ice lenses within the snow and impermeable firn below the snowpack both greatly impact this water storage. Some of the discrepancy between the values in this study versus others may be in the time of year that these data are collected. All of the 2012 and 2021 data are collected in mid-July where temperatures are consistently above freezing and rain-on-snow events are possible. Both of these factors may increase the liquid water content that remains in the snow when these surveys are conducted.

Evidence of ice lensing is prevalent across JIF supporting that there are large-scale meltwater or rain events where water percolates deeper into the snowpack before refreezing into an ice lens.

The spatial variability in the liquid water content could vary depending on the time of day of radar transects and the meteorological conditions prior to surveying. For example, the day before the radar survey of Taku and Matthes Glacier in 2021, there was a rain on snow event. Should this be the main impetus for higher liquid water content values on T'aakú Kwáan Sít'i (TKG3, TKG4, and TKG5), this would mean the snowpack shows high short-term sensitivity to precipitation (and melt). The spatial variability between the snow pit sites also supports an increased sampling density of ground truth points. Because in the same year, within a week to 10 days, there is variability in liquid water content between 0 to 19 percent it cannot be assumed that the conditions are the same across an entire study site.

Such sensitivity has implications for GPR surveys with the goal of surveying the near surface. Because interpreting depth from GPR surveys depends on accurate assumptions or measurements of density and water content, such short-term sensitivity observed herein would require higher temporal sampling density of these ground truth points.

2.5.4. Limitations and Future Work

We cannot make any assertions about changes between years being trends (or not), given that these two datasets represent endpoints of nearly a decade in time for variables (snow thickness, density, water content, SWE) that exhibit high spatial and temporal variability. It is possible that warmer surface temperatures contribute to this difference in water content and density between years. Yet, it is also possible that variations of water content occur due to annual, daily, or even shorter controlling factors such as high daily temperatures or rain on snow events. In addition, the degree of variability between the survey years at the same location demonstrates I cannot make an

assumption of the same conditions between years even if surveys occur at the same time as years prior.

2.6. Conclusions

I combined data 150 km GPR data and depth and density data from 31 snow pits across JIF collected in July 2012 and 2021 to assess the variability in snow properties and calculate SWE. Depth density trends across JIF within and between years are relatively consistent and liquid water content ranges from 0-19%. From these two years of extensive, repeated GPR surveys, I observe high variability in calculated relative permittivity and water content across JIF resulting in potential for high uncertainty in depth (30.5-54.1 %) and SWE (32.2-56.2 %) when using GPR to determine SWE. I demonstrate that SWE estimations from GPR require extensive ground truth campaigns in this temperate, coastal environment due to the spatial variability in liquid water content in the snowpack. Future work should include quantifying this spatial and, likely, temporal variability in water content at a higher resolution to better determine SWE from GPR.

As the climate continues to change, the prevalence of liquid water within annual accumulation may increase, potentially complicating the interpretation of GPR in other Alaskan and Western Canada glaciers and likely more polar glaciated areas like Greenland and other Arctic glacier systems. Temperate glacier systems are amongst those predicted to lose mass and contribute the most to global sea-level rise in the next century as they have a higher sensitivity to temperature increases (Oerlemans and others, 2005; Rounce and others, 2023). Both ground-penetrating and airborne radar surveys are common in high latitude glacier and ice sheet surveys. Temperatures are rising faster at the poles than at the mid-latitudes, especially in the Northern Hemisphere. In recent years, there have been multiple incidences of rain-on-snow events at Summit Station in Greenland (Xu and others, 2022). For future interpretations of ground-based

and airborne radar surveys of these areas to have accurate interpretations of depth and SWE, it is important to conduct ground-truth campaigns as close as possible to the time of surveying and across as large of a spatial scale as possible.

CHAPTER 3

FIRN VOLUME LOSS ACROSS THE JUNEAU ICEFIELD, ALASKA

BETWEEN 2012 AND 2021

3.1. Abstract

Repeat 400 MHz ground-penetrating radar (GPR) transects collected in 2012 and 2021 across the southern portion of the Juneau Icefield in Southeast Alaska showed significant firn thinning across the study site. T'aak̲ú K̲wáan Sít'i and all tributary branches experienced on average a 3.10 ± 1.73 m decrease in firn thickness. Random forest regression and linear regression analyses reveal the difference in firn thickness across the Juneau Icefield is most correlated with marine proximity and positive atmospheric temperature difference between firn accumulation periods, variables related to accumulation and ablation patterns. Firn volume has decreased by over 50 percent during the study period. Such a decrease will have implications for the future mass balance and meltwater storage capacity and increases the Juneau Icefield's vulnerability to current and future climate change.

3.2. Background

Firn is an important component in any glacier system as it is the surviving accumulation that densifies into glacier ice. Firn densification processes, including grain-boundary sliding, pressure sintering, and compression, have been well-documented in polar firn (Herron and Langway, 1980; Maeno and Ebinuma, 1983; Alley, 1987; Wilkinson, 1988; Stevens and others, 2020). Temperate firn densification is much less well-constrained. While undergoing its metamorphosis from snow to glacier ice, firn retains some porosity where air or water can move through. Firn has a profound influence on englacial hydrology due to its porosity as it stores meltwater temporarily where, in its absence, glacier ice at the surface is more impervious, acting as a conduit for more immediate

43

runoff (aside from at the small-scale grain boundaries and larger scale flow pathways such as crevasses and moulins which can retain water) (Fountain, 1996; Jansson and others, 2003). The meltwater storage capacity of firn depends on its porosity and layer thickness (Fountain, 1996). The short-term meltwater storage that firn and firn aquifers provide is a means to conserve mass for a slightly longer time and reduce immediate meltwater runoff flux to downstream ecosystems (Beniston, 2003; de Woul and others, 2006). Increased meltwater runoff may highlight important icefield-to-ocean linkages including colder water temperatures, increased turbidity, and decreased salinity in the area of mixing. These important factors are likely to affect micro- to macro-scale species within the marine ecosystem, such as phytoplankton and salmonids and especially those that have a narrow range of tolerance (Moore and others, 2009; O'Neel and others, 2015). Further, depending upon the bed geometry and topographic constraints, the evolution of the firn limit impacts a glacier's terminus behavior (Mercer, 1961).

Meltwater and persistent firn aquifers have been observed in firn in many glaciated areas including, the Juneau Icefield (Verboncoeur and others, AGU Abstract 2019; Case and Kingslake, AGU Abstract 2020; Johnson and Meyer, AGU Abstract 2022), Svalbard on Holtedalfonna, Yukon Territory (Christianson and others, 2015) on the upper Seward (Sharp, 1951) and Kaskawulsh Glaciers (Ochwat and others, 2021), the Greenland Ice Sheet (Koenig and others, 2013; Kuipers Munneke and others, 2014; Forster and others, 2014), and on the Antarctic Peninsula (Mongomery and others, 2020; van Wessem and others, 2021). This process has been estimated to reduce the immediate impacts of melt from the Greenland Ice Sheet on contributions to global sea-level rise (Harper and others, 2012).

Both ground-penetrating and airborne radar have been proven to be effective methods to study firn evolution and firn aquifers (Arcone and others, 1995; Campbell and others, 2013;

Gascon and others, 2013; Sold and others, 2015; Miège and others, 2016; Chu and others, 2018; Miller and others, 2020). Ground-penetrating radar (GPR) detects layers of different electromagnetic properties. In a temperate glacier environment these differences are due to density, water content, and chemical composition, albeit chemical stratification is less likely than in Polar glaciers due to meltwater influence (Campbell and others, 2012a; Winski and others, 2012). The top of the firn layer, or previous summer ablation horizon, is a distinguishable layer in most radargrams. The lower boundary of the firn layer, or the firn-ice transition, is easy to identify near the equilibrium line altitude and becomes more difficult to identify in high elevation and accumulation areas, likely due to a more gradual depth-density gradient at higher elevations (Fig. 3.1).

Firn loss is a physical manifestation of a negative mass balance. In glacier systems experiencing prolonged negative mass balance and already experiencing retreat, it is expected that any further decrease in firn thickness and associated firn volume to exacerbate existing glacier behavior. This decrease in mass influx and associated meltwater storage capacity influences the system dynamics dependent upon existing bed, hydrological, and terminus conditions (Mercer, 1961).

T'aak̲ú K̲wáan Sít'i (the T'aak̲ú peoples' glacier, Taku Glacier) drains much of the southern portion of the Juneau Icefield (JIF) and its 671 km² area (Pelto and others, 2013). It drains mainly into the Taku Inlet to the southeast of JIF and it is currently protected by its terminal thrust moraine from more intense frontal ablation (Zechmann and others, 2020). Unlike many glaciers in Alaska, at the beginning of the study period in 2012, T'aak̲ú K̲wáan Sít'i was still advancing. By the end of the study period, in 2021, T'aak̲ú K̲wáan Sít'i officially had entered into retreat. This retreat is related to changes in the long-term mass balance of the system where there had been a decreased

rate in area increase for the decades preceding retreat (McNeil and others, 2020). This change in behavior may be linked to one or a combination of dynamic thinning, increased firn densification, or increased surface ablation (Kuippers Munneke and others, 2015). By understanding the behavior of the firn across JIF, it may be possible to discern which of these is contributing the most to the overall decrease in mass balance.

The objectives of this study are to (1) quantify firn extent and thicknesses for 2012 and 2021 from GPR and ground-truth where feasible, (2) determine any spatial and temporal trends in the thickness and distribution of firn, and (3) calculate changes in firn volume between study years.

3.3. Methods

To (1) quantify firn extent and layer thicknesses for 2012 and 2021 from ground-penetrating radar and (2) determine any spatial and temporal trends in the thickness and distribution of firn, I use GPR to discern layer thicknesses and spatial analyses to determine significance. To (3) estimate firn volume change, I differenced layer thickness calculated from the 2021 data from thickness calculated using the 2012 data across the shared spatial extent.

3.3.1. Ground-penetrating Radar (GPR)

3.3.1.1. Data Collection and Processing

We collected repeat common-offset GPR transects across JIF in 2012 and 2021. These data were collected with a Geophysical Survey Systems Incorporated (GSSI) 400 MHz model 5103 antenna and SIR-4000 control unit (2021) or SIR-3000 (2012) along the same GPS tracks in both years. To quantify the firn layer thickness, I performed several basic radar processing steps. Each respective branch of radar data across the icefield was time-zero corrected, distance normalized, stacked, and bandpass filtered with a low pass of 800 MHz and a high pass of 100 MHz. The 2012 transects were distance normalized through GPS track correlation at 50 m intervals. The 2021

transects were distance normalized using readgssi, an open-source python package (https://github.com/iannesbitt/readgssi.git). I identified and manually delineated the annual accumulation (AA) and firn-ice transition (F-I) horizons in the radargrams. When referencing the AA layer, I mean the accumulation that remains at the time of GPR data collection. Data collection does not occur at the end of the water year; instead, due to logistical constraints, it is collected during July concurrent with the Juneau Icefield Research Program's field program.

3.3.1.2. Interpretations and Assumptions

We interpret the firn layer as that which resides between the depth of the annual accumulation and of the firn-ice transition. The annual accumulation layer is characterized by continuous horizons that cross-cut deeper horizons (interpreted as previous ablation surfaces). I followed this AA horizon throughout the radargram from below the equilibrium line altitude (ELA) to higher elevation regions to delineate the top of the firn layer. Then, I follow the divergence where deepest layers dip away from the AA layer up-glacier as the lowest discernable horizon and interpret this to be the firn-ice transition. It is easier to interpret the firn-ice transition (F-I), at lower elevations because the bottom of the AA horizon intersects the ELA and associated F-I horizon as an unconformity. Up-glacier of the ELA, the interpreted F-I transition is clearly visible internal stratigraphy beneath the annual accumulation layer for most of the icefield. Several other englacial layers become visible at higher elevations between the interpreted F-I transition and bottom of the AA horizon as well. At the highest elevation sites of JIF, the F-I transition often is difficult to manually identify as it is a less stark transition. I interpret this smaller change in magnitude to result from a more gradual depth-density boundary between firn and glacier ice (Fig. 3.1.). Areas where it was difficult or impossible to confidently identify these horizons were excluded from these results and analysis.

47
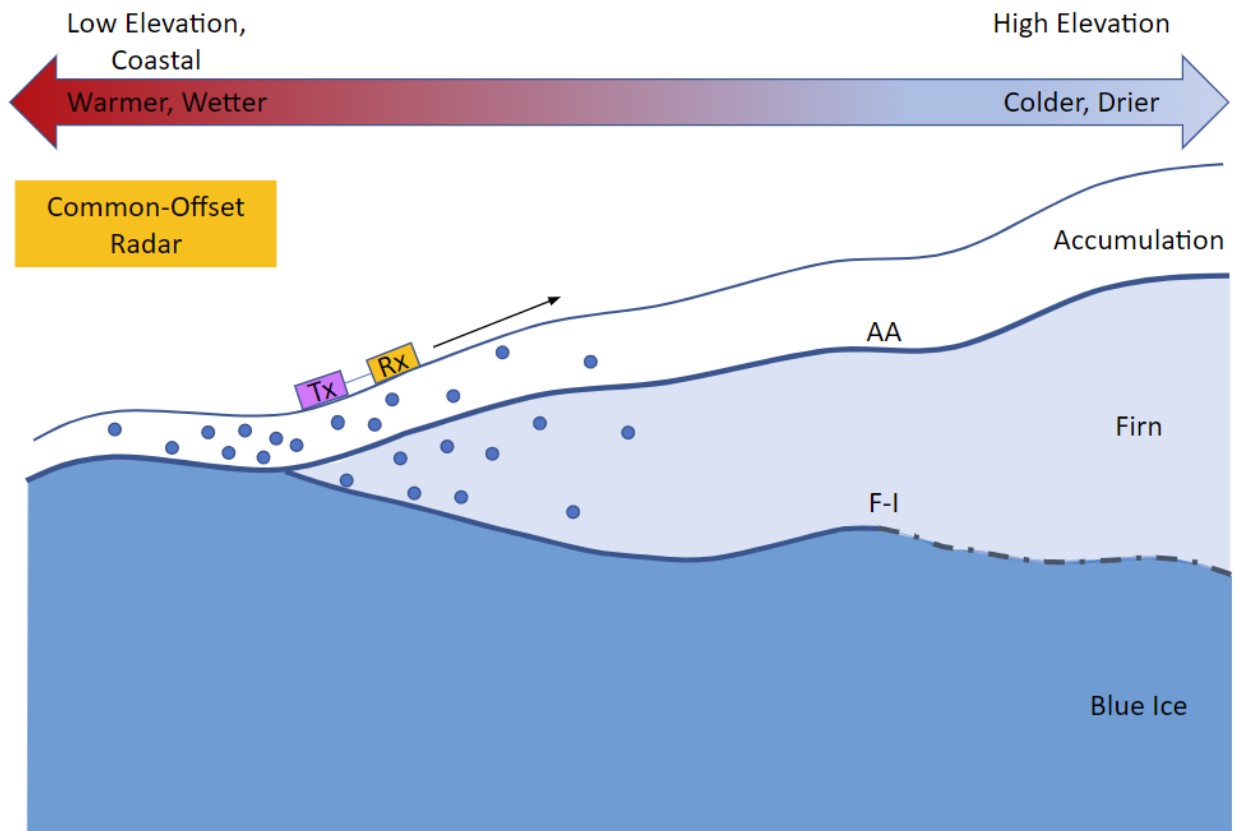
Figure 3.1. Schematic representation of common-offset ground-penetrating radar surveys in a temperate ice environment with representations of the annual accumulation (AA) and firn-ice transition (F-I) layer delineations.

To determine the net two-way travel time (TWTT) within the firn layer alone, I calculated the difference of the TWTT of the respective layers (F-I – AA). This net TWTT and the assumed bulk relative permittivity of the firn is then applied to Equation 3.1 to determine the thickness of the firn layer, z, in each year across all of the profiles,

$$(3.1) \ z = \frac{TWTT * v}{2}$$

where v is the radio wave velocity through the firn. In this case, I use the interpretation of common midpoint surveys collected on JIF in 2015 to determine the bulk relative permittivity of the firn. These surveys were collected using two 400 MHz model 5103 antennas with a SIR-4000 control unit at 5 cm and 10 cm intervals. As such, I use a velocity of 0.122 m ns^{-1} ($\acute{\varepsilon}$ = 6) for all firn thickness calculations. Although this value is at the high end of the values presented in Chapter 2, it is a reasonable assumption given is (1) the result of this deeper, in-situ common midpoint survey which is the only in-situ measurement available in this location, (2) firn is expected to be denser than the accumulation layer and extensive firn aquifers have previously been observed in this study site (Verboncoeur and others, AGU Abstract 2019; Case and Kingslake, AGU Abstract 2020; Johnson and Meyer, AGU Abstract 2022), and (3) that this value falls within the range of the correlated refractive indices presented for wet firn on Bagley Icefield (Arcone, 2002). Available data do not yet allow for an analysis of the spatial variability in relative permittivity of firn and this is recommended for future studies to consider.

The thickness values for each year were interpolated across the spatial extent of JIF using the Inverse-Distance Weighting (IDW) method with respect to the three closest reference points. This spatial interpolation method preserves the true values of the known data and interpolates between points based on the distance between the unknown location and a number of the closest known points. This results in rasters of the 2012 firn layer thickness and 2021 firn layer thickness.

To determine the change in firn thickness across the same spatial extent, I subtracted the 2012 firn thickness raster from the 2021 firn thickness raster to create one firn difference raster where negative values indicate a local decrease in firn thickness over the time period and positive values indicate an increase in firn thickness.

3.3.2. Firn Volume

To estimate firn volume, I created an area that encompasses the overlap between surveys in both 2012 and 2021. For each year, I buffered the survey transects on the glacier centerlines by 1 km on each side, except for those on Echo Glacier which were buffered by 0.5 km on each side since the glacier is narrower than the other main tributary branches. I also buffered the cross sectional transects by 0.5 km. These boundaries were chosen as opposed to the total surface area of the glaciers because this closely-bounded area is more likely to capture the firn volume without being subject to more severe uncertainties with interpolation along more linear features of the input radar transects especially considering the lack of strong predictive power of regression or deep learning techniques for firn thickness (Maurer and others, in review). I then clipped the resulting geospatial raster layers using the intersect tool on ArcGIS Pro to maintain only the area covered by both the 2012 and 2021 datasets, therefore maintaining a constant surface area over which to compare volume change between 2012 and 2021 (Fig. 3.2). I created a triangulated irregular network (TIN) from the raster data representing the depth of firn for both years with a Z tolerance of 0 and a Z factor of 1, meaning that the TIN should match the input raster exactly. I calculated firn volume above the reference plane with the Polygon Volume tool using a reference height of 0, therefore calculating the volume of firn where values are greater than zero for each year. Finally, I calculated the difference between the firn volume in 2012 from that of 2021 to estimate firn volume change over this study period.

Additionally, I repeated these steps with an IDW raster of the difference in firn thickness between 2012 and 2021. As opposed to the individual years of firn thickness rasters, this one included both positive and negative values (not just positive values). This consideration meant calculating the volume both above and below the reference plane (positive and negative values) where the volume above the reference plane represents firn volume increase and that below the reference plane represents volume loss. The sum of these, where volume increase is positive and decrease is negative, represents the overall change in firn volume over the study period.

3.3.3. Analysis and Trends

3.3.3.1. Spatial and Temporal Trends

To determine any spatial and temporal trends in the thickness and distribution of firn, I generated descriptive statistics for both years of data and the calculated change for the entire spatial extent. To evaluate the spatial variability, I calculated descriptive statistics for each individual branch. This division of data presents an idea of how the mean, standard deviation, and range compares between branches. I calculated and identified the areas with higher and lower percent change in firn thickness. To determine the temporal variability, I compared the 2012 and 2021 firn thickness descriptive statistics and calculated the percent change in firn at each point.

3.3.3.2. Evaluating Covariance
Snow accumulation, ablation, firn thickness, and firn extent are influenced by multiple variables. I assessed the relative importance of several of these variables that may impact changes in firn on JIF for each point using a random forest regression model. The purpose of implementing this regression is to assess the relative importance and correlation of each variable and is not for prediction purposes. I ran the random forest regression model using the RandomForestRegressor from sci-kit learn (Pedregosa and others, 2011). This model was run with the following parameters: 1,000 trees, a 75/25 percent training/testing split, and a random state =
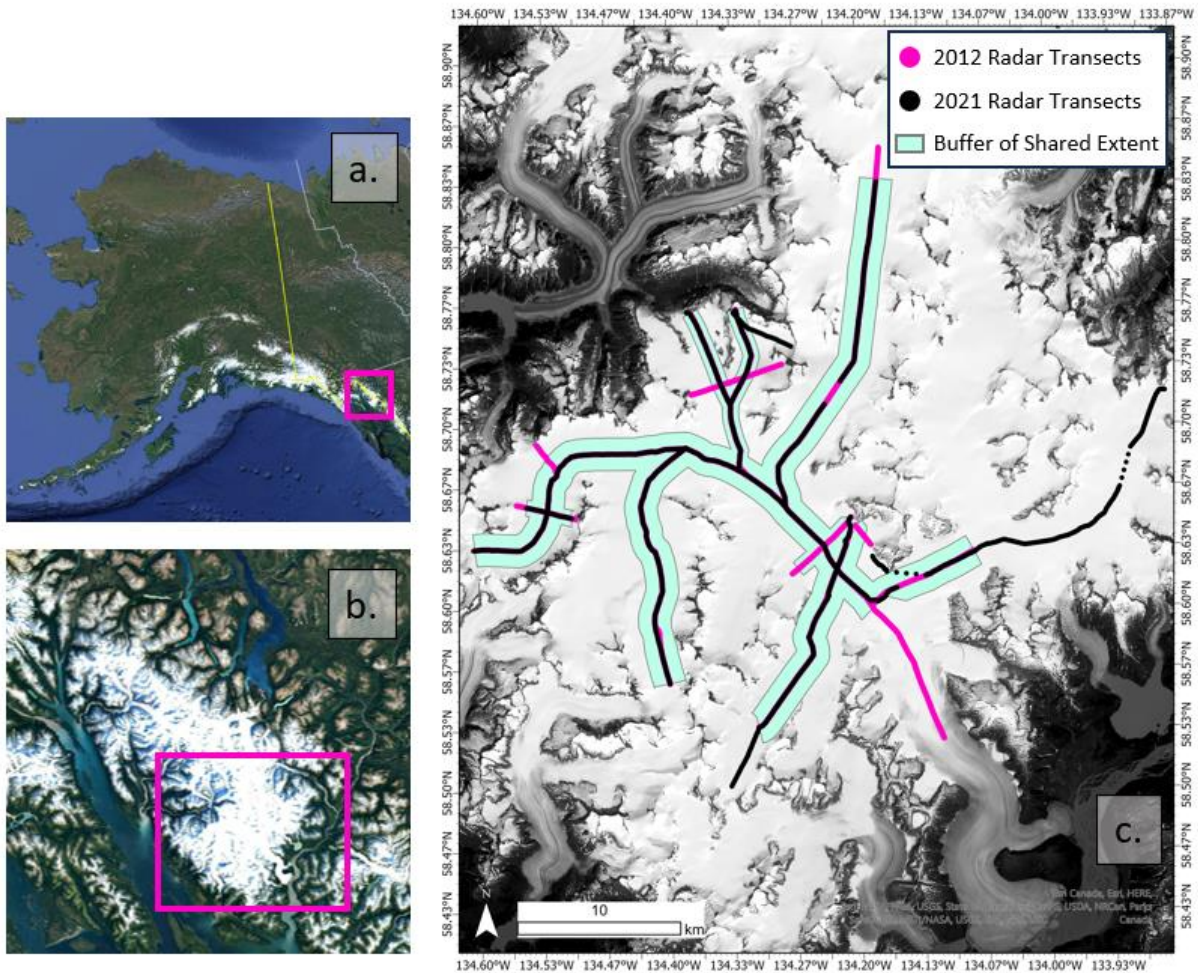
Figure 3.2. (a) Study site relative to Alaska and Northwest Canada (pink box). (b) Study site in relation to the Juneau Icefield (JIF), highlighting the southern portion (pink box). (c) Surface area over which firn volume is calculated (seafoam green) created from the shared buffered area of the radar transects collected in 2012 (pink) and 2021 (black).

42. I ran multiple random forest regressions to identify the variables with the greatest relative importance by first assessing the entire suite of variables, then iteratively excluding the variable with greatest relative importance in the next run. These results then informed the subsequent linear regression analyses to evaluate the individual variable correlation with the difference in firn thickness.

These variables include, elevation, distance from a moisture source, slope, curvature, proximity to exposed bedrock, and difference in the average number of positive degree days (PDDs) seasonally in the 5 water years preceding the accumulation during the radar collection years. These variables were chosen to consider position, surface characteristics, and ablation at each point.

3.3.3.2.1. Positional Variables The positional variables include elevation and distance from a moisture source. Elevation influences both temperature and precipitation and distance from a moisture source impacts precipitation patterns. Elevation is determined using a digital elevation model (DEM) of JIF generated by the Polar Geophysical Center at 10 m resolution. I reprojected this raster from NSIDC Sea Ice Polar Stereographic North Projection to UTM Zone 8N to match that of the GPR transects. Elevation data are extracted to each data point across JIF. Points are representative of individual scans in the GPR transects. Distance from a moisture source is calculated from the delineation of the coastline closest to JIF as per methods in Maurer and others (in review). This coastline borders the Favorite Channel and Gastineau Channel. I use the Near tool in the Analysis Toolbox on ArcGIS Pro to calculate the planar distance from each point on JIF to the delineated coastline.

3.3.3.2.2. Surface Variables The surface variables include slope and curvature. Slope was calculated using the same DEM used for elevation data. I used the Slope tool in the 3D Analyst

Toolbox on ArcGIS Pro to calculate a raster of slope across the study site, then extracted the values at each point. Curvature, the rate of change of the slope, was also calculated from this DEM but using the Curvature tool in the 3D Analyst Toolbox on ArcGIS Pro.

3.3.3.2.3. Ablation Variables The ablation variables considered are proximity to exposed bedrock and seasonal changes in the number of positive degree days during 5 water years preceding the survey years. These variables impact the amount of heat entering the system. I defined proximity to exposed bedrock as the minimum distance from each point to the edge of the glacier as outlined by the Randolph Glacier Inventory 6.0 for Alaska (RGI60). To do so, I first merged the extent of all of the glacier polygons on JIF into one polygon and then created a second polygon that encompassed the entire JIF. Using the Erase tool (Analysis toolbox), I erased areas of the second polygon that contained the glacier area to result in a rock outcrop polygon. With the Near tool (Analysis toolbox), I calculated the minimum distance from each point to the exposed bedrock.

The metamorphosis of snow to glacier ice on a temperate glacier occurs on a sub-decadal scale. Changes in the seasonal number of positive degree days during the 5 water years preceding the survey years are anticipated to impact the ablation potential of snow and firn. This was calculated using the National Weather Service and National Oceanic and Atmospheric Administration's Climate and Past Weather NOWData for daily average temperature at the Juneau International Airport (8 m a.s.l.). For 2012, this includes 2006-07, 2007-08, 2008-09, 2009-10, and 2010-11 encompassing every day between 01 September 2006 to 31 August 2011. For 2021, these are 2015-16, 2016-17, 2017-18, 2018-19, and 2019-20 which include every day from 01 September 2015 to 31 August 2020. These data were compiled into daily seasonal temperatures (DJF, MAM, JJA, SON) at the airport for the 5 years preceding 2012 and 2021. I used the elevations at each point extracted from the Polar Geophysical Center DEM to calculate the daily

temperature at all points using a lapse rate of -5℃ km⁻¹ (McNeil and others, 2020). For each point, I summed the number of positive degree days, which I define as any day with a temperature above 0℃, and then took the average of these days per season at each point. This was done for both the 2012 and 2021 seasonal data. Finally, I calculated the difference between the average number of positive degree days per season leading up to 2012 from those leading up to 2021 to calculate the difference in the number of positive degree days at each point per season.

Additionally, I summed the average number of positive degrees per season and annually for each of these preceding 5-year periods. I then took the difference of the numbers of positive degrees between 2012 and 2021 at each point to approximate the degree of heat difference.

3.4. Results

3.4.1. Ground-penetrating Radar

3.4.1.1. 2012 Results. Clear horizons were visible in the radar transects in 2012. Multiple horizons were discernible within the interpreted firn layer. Cross-sectional transects showed the U-shaped nature of the firn layer moving away from the sidewalls (Fig. 3.3). Longitudinal centerline profiles displayed increasing two-way travel time between the interpreted annual accumulation layer and the firn-ice transition layer. The interpreted firn-ice transition layer was often wavy in character and most clear at lower elevations and more difficult to discern at higher elevations up-glacier.

At the time of data collection, the average thickness of firn in 2012 was 5.78 m ± 2.86 m. Total firn thicknesses ranged between 0 to 14.32 m. Areas with the thickest firn both on average and overall in 2012 include, Matthes-Taku (6.19 m ±3.76 m), Northern-Northwest Branch (7.16 m ± 1.27), and Southern-Northwest Branch (3.76 m ± 1.56 m) (Fig. 3.4). Demorest Glacier had the lowest average firn thickness (3.19 m ± 1.10 m). These thickness values were calculated using a relative permittivity of 6.
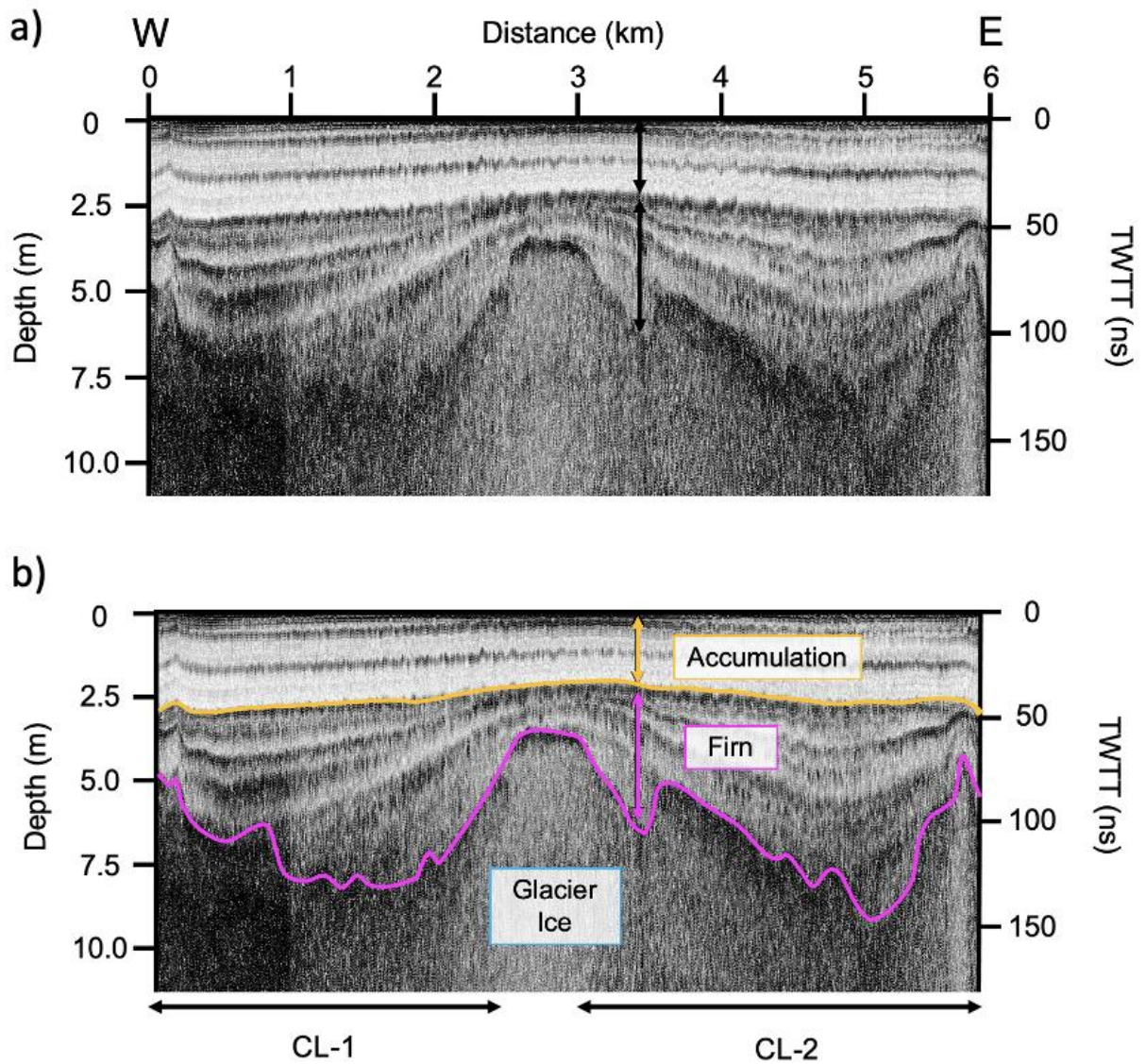
Figure 3.3. (a) Radargram of Echo Branch cross-section across Echo Centerline 1 (CL-1) and Echo Centerline 2 (CL-2). Depth (left) calculated using a relative permittivity of 6 and two-way travel time (TWTT, right). (b) Interpretations of the accumulation layer and the firn-ice transition.
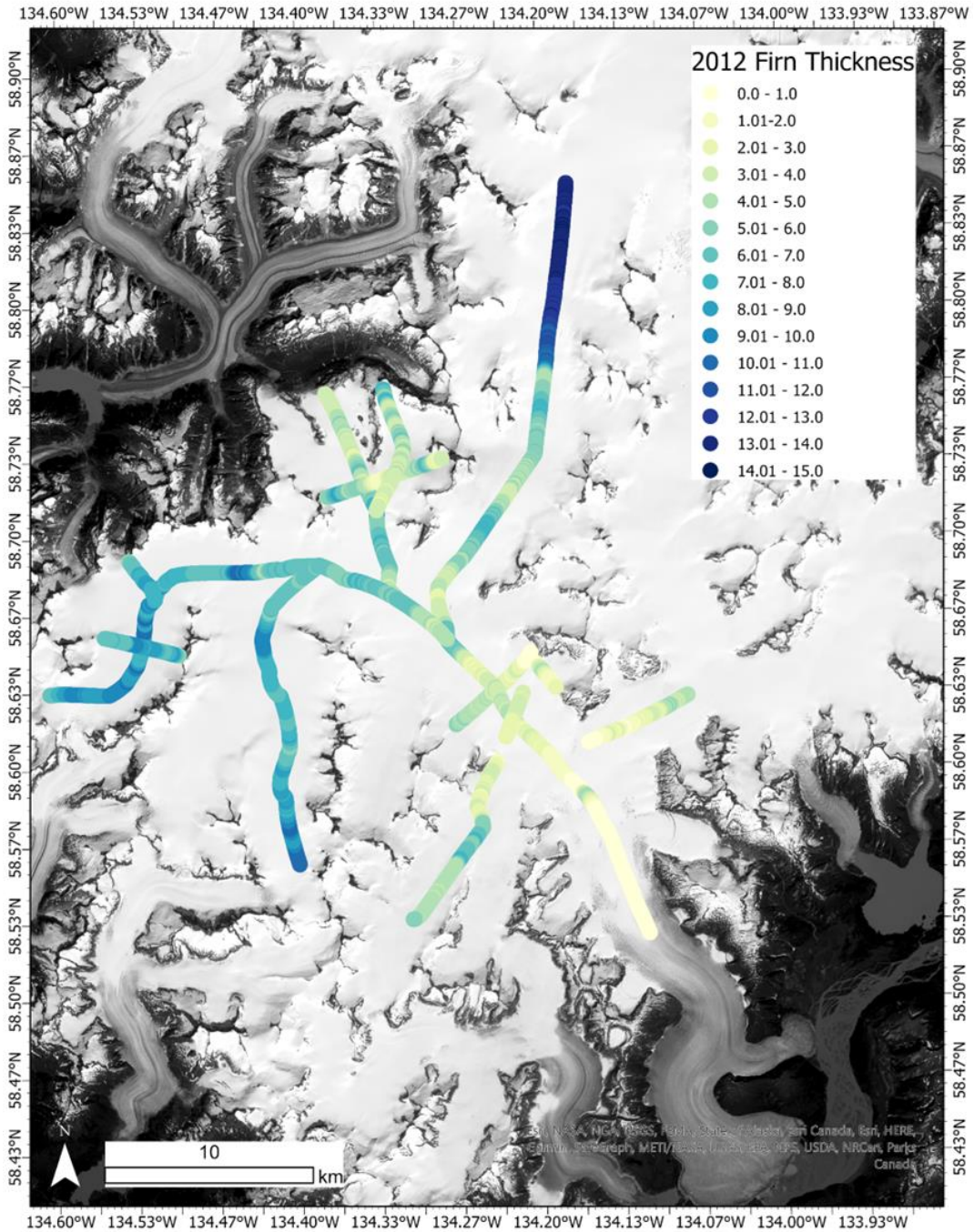
Figure 3.4. Firn thickness (m) along radar transects in 2012 using a relative permittivity of 6. Color scale represents low values in light yellow and increases in tones of greens to blues for higher values.

3.4.1.2. 2021 Results. Multiple horizons were visible within the interpreted firn layers for all of the transects with firn. Transects collected moving up-glacier and across an ice divide, including Northern-Northwest branch, Southwest Branch, and Matthes-Taku, showed general trends of increasing horizon two-way travel time of the interpreted firn layer moving up-glacier. This was not a linear increase and was more undulatory in nature. Near the interpreted ice divide, there are the longest two-way travel times defining the firn layer before they then decrease again moving away from the divide.

The average thickness of the firn in 2021 was 2.95 ± 2.31 m (Table 3.1). Areas with the greatest amount of firn include, Northern-Northwest Branch (5.77 ± 1.29 m), Southern-Northwest Branch (3.79 ± 1.31 m), and Echo-Right (2.37 ± 1.60 m) (Fig. 3.5). These thickness values were calculated using a relative permittivity of 6. Notably, within the shared study extent, Demorest Glacier had no firn in 2021.
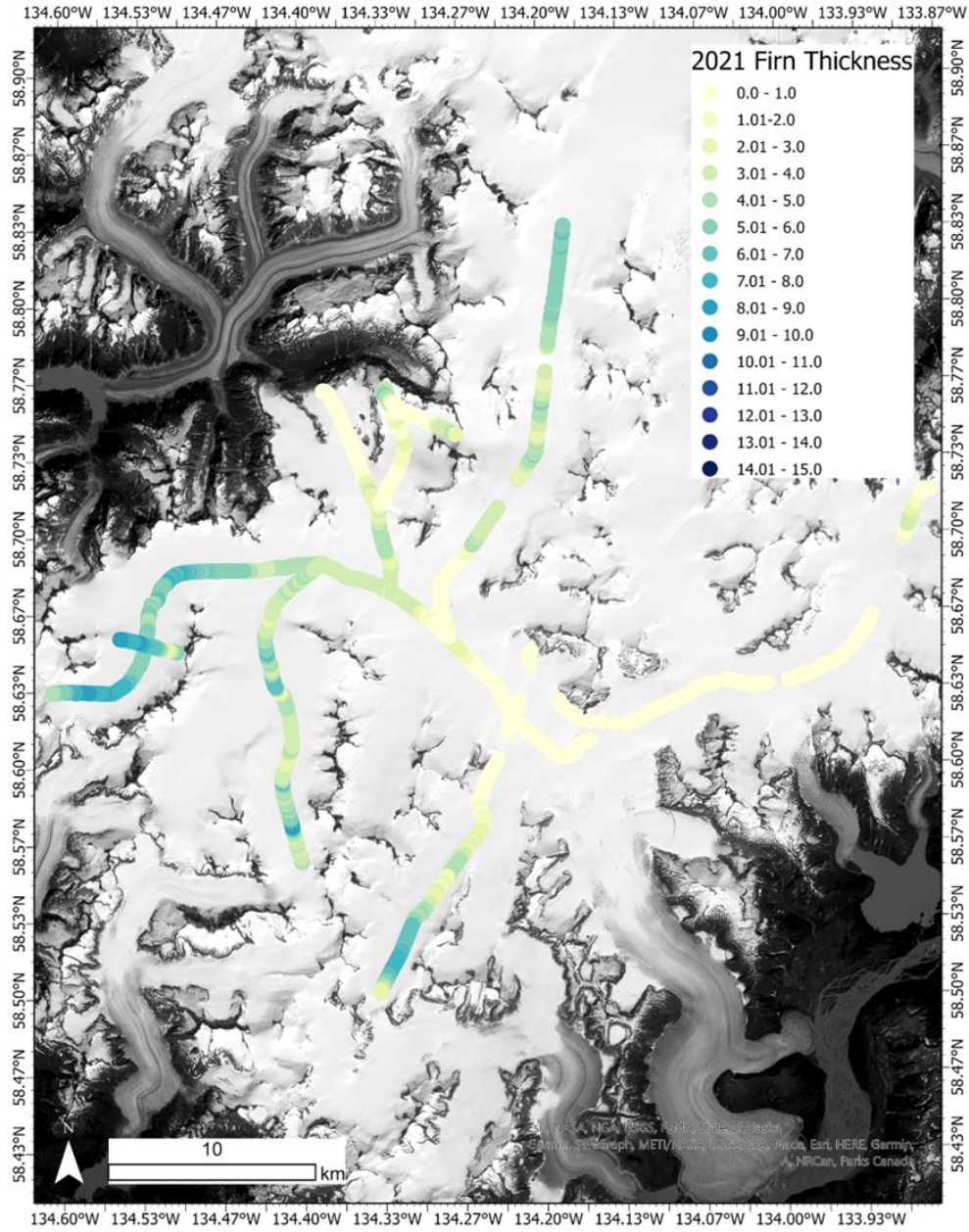
Figure 3.5. Firn thickness (m) along radar transects in 2021 using a relative permittivity of 6. Color scale represents low values in light yellow and increases in tones of greens to blues for higher values.
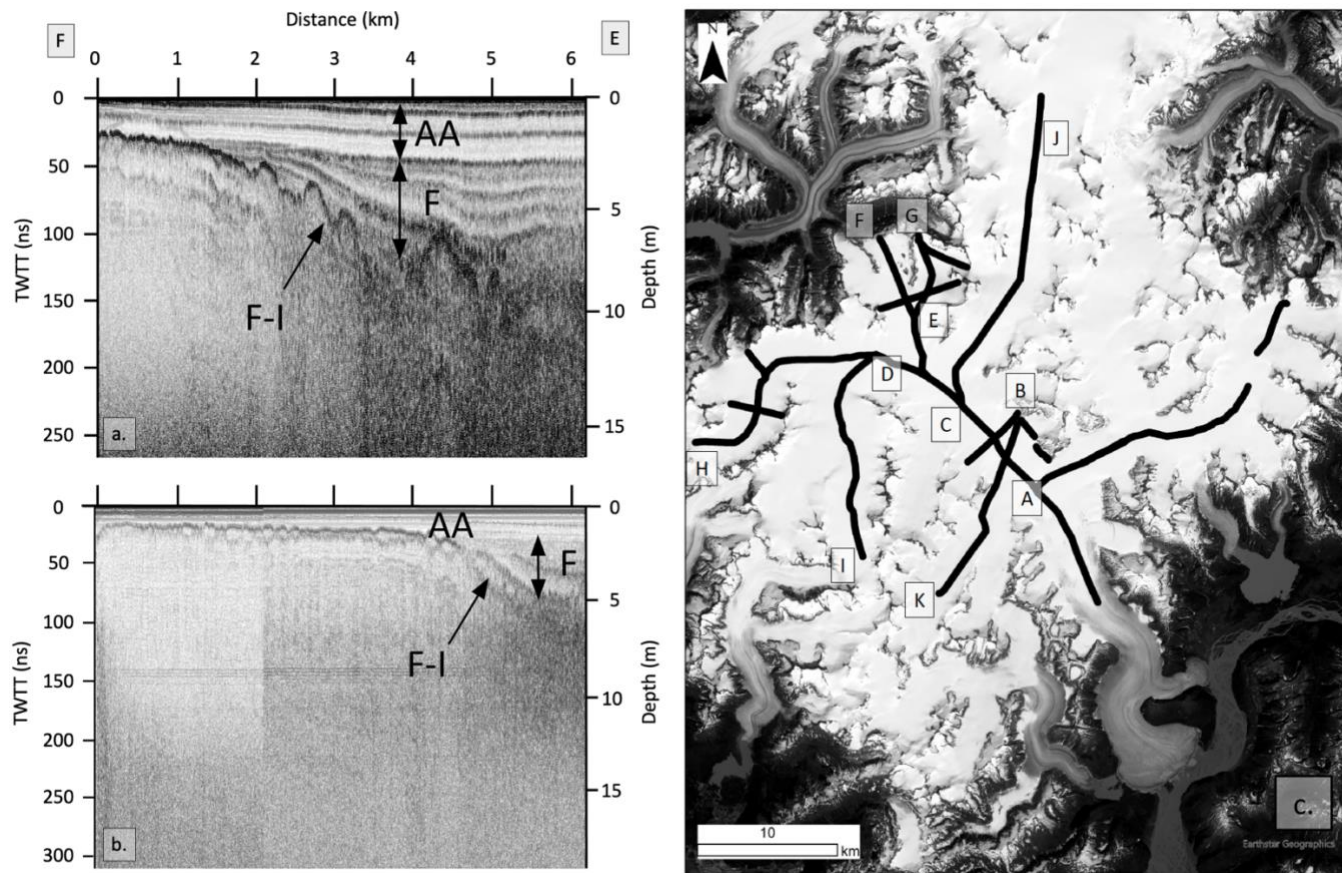
Figure 3.6. 400 MHz centerline profiles of Echo Glacier – Center in (a) 2012 and (b) 2021. Depths are interpreted with a relative permittivity of 6 (v = 0.122 m ns^{-1}) and interpreted annual accumulation (AA), firn (F), and firn-ice transition (F-I) are indicated. (c) Location of profile relative to the southern portion of the Juneau Icefield is from F to E.
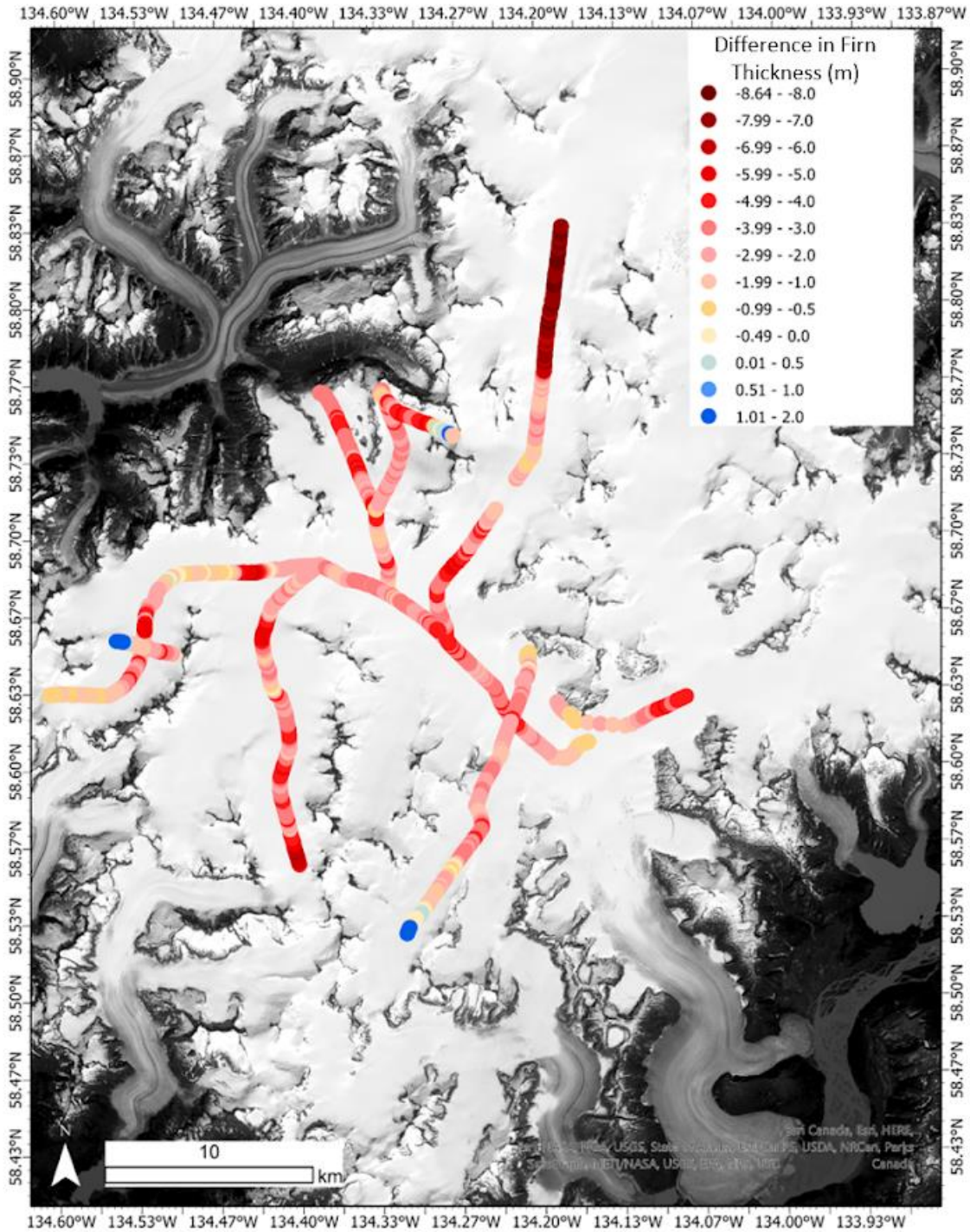
Figure 3.7. Change in firn thickness across JIF between 2012 and 2021 ($\acute{\epsilon} = 6$) where light blues indicate an increase in firn thickness and reds indicate a decrease in firn thickness (darker reds with increasing magnitude).
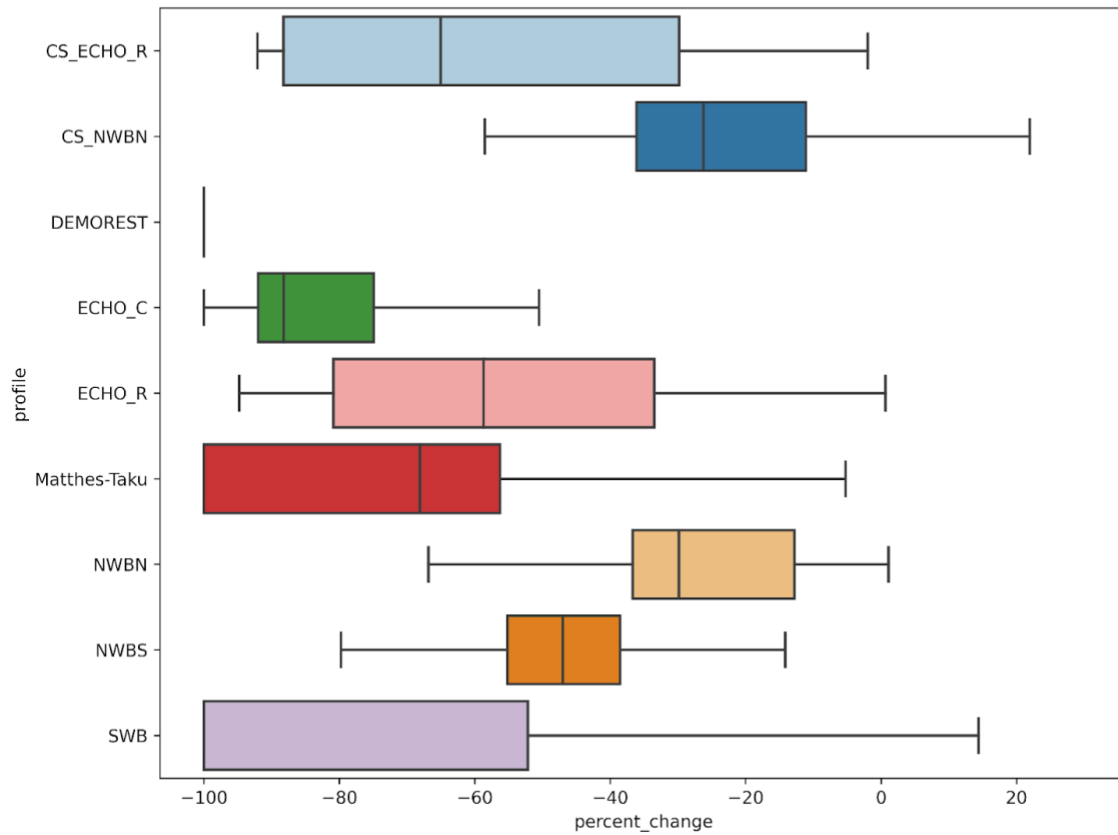
Figure 3.8. Box and whisker plot of percent change (2012 to 2021) in firn thickness across the surveyed areas of the Juneau Icefield separated by tributary branches and cross-sections (Echo-Right Cross-Section (CS_ECHO_R), Northern-Northwest Branch (CS_NWBN), Demorest Glacier, Echo Glacier-Center (ECHO_C), Echo Glacier-Right (ECHO_R), Matthes-Taku Glaciers, Northern-Northwest Branch (NWBN), Southern-Northwest Branch (NWBS), and Southwest Branch (SWB).

	2012 (m)	2021 (m)	Difference (m) (2021-2012)	Percent Change (%)
Mean	6.04	2.95	-3.10	-58.2
Standard Deviation	2.76	2.31	1.73	30.3
Minimum	0.00	0.00	-8.64	-100
25%	3.95	0.35	-3.96	-90.4
50%	5.93	3.26	-2.90	-55.8
75%	7.52	4.59	-1.99	-35.8
Maximum	14.32	8.52	1.45	29.9

Table 3.1. Descriptive statistics for firn thickness, firn thickness change, and percent change for the shared extent of 2012 and 2021 radar transects. Data coverage of the same spatial extent.

Year	Firn Volume ($10^8 \, m^3$)	Total Surface Area for Calculation ($10^8 \, m^2$)
2012	10.5	1.69
2021	5.11	1.66
Difference (2021 - 2012)	-5.41	
IDW of Difference in Firn Thickness	-5.20	1.66

Table 3.2. Firn volume and surface area of calculation in 2012 and 2021 from individual years. Additionally, firn volume and surface area of calculation for an IDW raster of difference in firn depth.
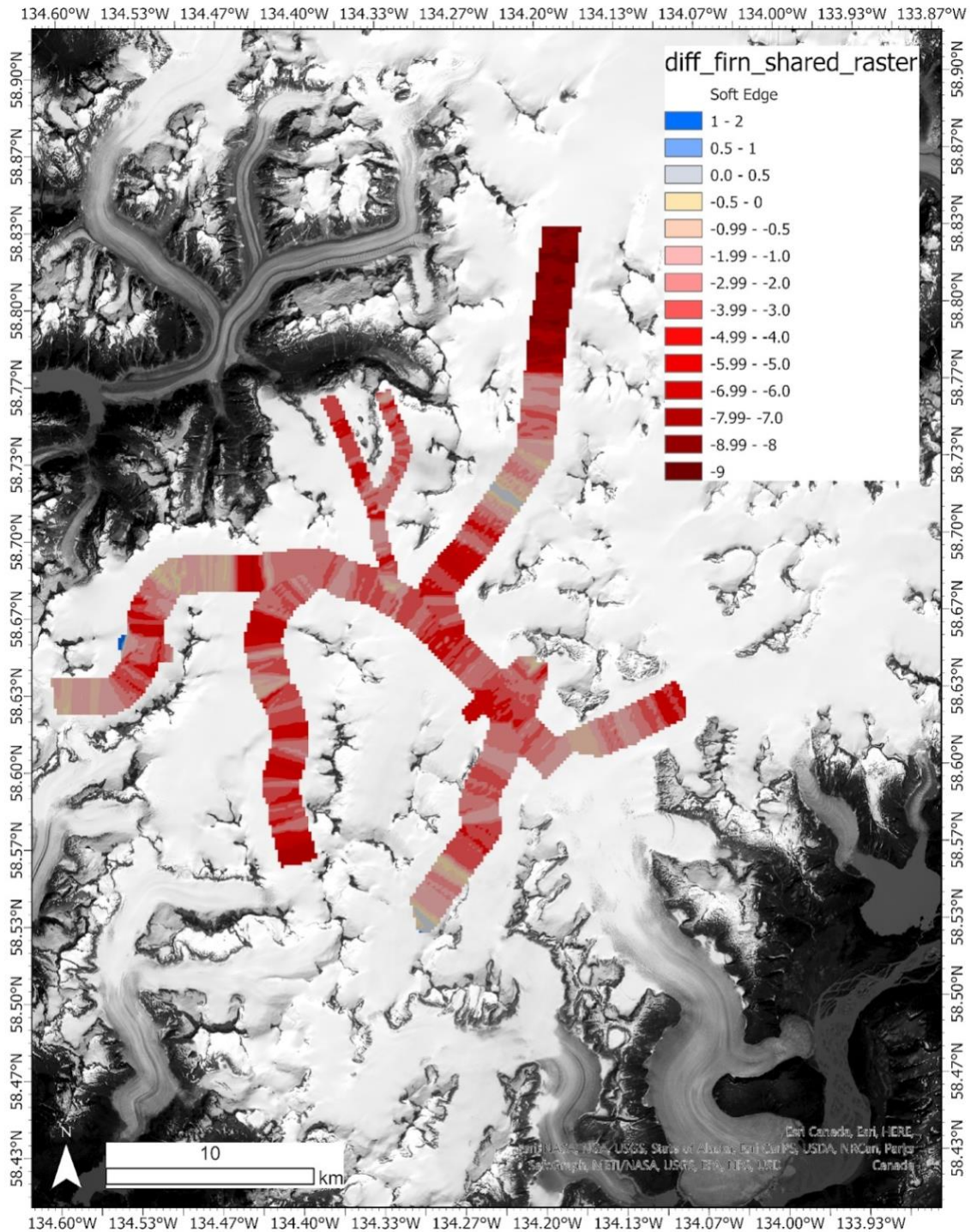
Figure 3.9. Difference in firn depth across which firn volume calculations are made.

3.4.1.3. Change in Firn. Compared to 2012, the 2021 radargrams showed an overall decrease in thickness and extent of firn in all centerline transects (Fig. 3.6, Figs. A.1-A.4). An example of this is Figure 3.6 where the firn line on Echo Glacier-Right has moved 3.5 km upglacier between 2012 and 2021. Additionally, the firn layer has decreased ~5m at its thickest point. Where firn still exists in the 2021 surveys, the shape of the firn layers appear similar to that at the same location in 2012.

Across the study site, there was an average difference in firn thickness of -3.10 ± 1.73 m (Fig. 3.7). The general trend shows an overall decrease in firn across JIF with an average percent change between 2012 and 2021 of -58.2 percent (Table 3.1). Areas that experienced the greatest average percent decrease include Demorest Glacier (100 percent), Echo Glacier-Center (80.9), Southwest Branch (71.8), and Matthes-Taku (71.2) (Fig. 3.8, Table B.2). The Northern-Northwest Branch centerline and cross section and Southern-Northwest Branch experienced firn loss at a lower local percent change than other areas.

3.4.2. Firn Volume

Firn volume was calculated over a total surface area of $1.66 *10^8$ m^2 with interpolated depths to the shared extent buffer (Fig. 3.9). The estimated volume of firn across the study site in 2012 and 2021 is $10.5*10^8$ m3 and $5.11*10^8$ m^3, respectively (Table 3.2). This decrease represents a loss of 51.3% of firn volume over a decade.

3.4.3. Analysis and Trends

3.4.3.1. Random Forest Regression

Multiple regressions were performed by selectively removing or including variables to determine importance with each iteration. Relative importance from the random forest analysis revealed that, of the input variables, marine proximity (relative importance = 0.67) has the greatest impact on the predictive power of the regression. After marine proximity, the variables with greatest

importance were as follows, difference in annual positive degrees, elevation, and distance to exposed bedrock determined from elimination of the previous most influential variable. Most random forest regressions had a mean absolute error of 0.01 to 0.03 m. One, considering only difference in positive degree days seasonally and difference in annual positive degrees, had a mean absolute error of 0.18 m.

3.4.3.2. Positional Variables

Elevation had the third greatest relative importance of the included variables in the random forest regression. This random forest regression considered the entire suite of available data where there were no missing values. A linear regression of the difference in firn thickness between 2012 and 2021 with elevation yielded a weak negative correlation (R^2=0.0622) where, as elevation increases there is an increase in firn loss. This relationship is most evident at higher elevations (>1600 m a.s.l.) and otherwise there is not much of a trend observed across JIF. When this is broken down into a linear regression by the individual tributaries and cross-sections, differences in firn thickness on Demorest Glacier (R^2=0.2905), Matthes-Taku (R^2=0.2492), Northern-Northwest Branch cross-section (R^2=0.1773) had the highest correlation with elevation, though opposite directional relationships (Fig. B.5). The remaining profiles in order of decreasing correlation, Northern-Northwest Branch, Southern-Northwest Branch, Echo Glacier-Right, Southwest Branch, and Echo Glacier Cross section, had R^2 values <0.1.

Marine proximity was the most impactful variable in the random forest regression in predicting the difference in firn between 2012 and 2021. In a simple linear regression, difference in firn thickness has a weak negative relationship with marine proximity (R^2=0.1408). The farther from the coastline (least proximal) a point is, the greater the loss in firn thickness. When broken down into tributaries and cross sections, the correlation is strongest for Demorest Glacier

(R^2=0.6858), Northern-Northwest Branch cross section (R^2=0.5509), Echo Glacier-Right Cross Section (R^2=0.5509), and Matthes-Taku (R^2=0.2687). The remaining branches and cross sections have generally stronger correlations with marine proximity than with elevation as follows, Echo Glacier-Right (R^2=0.1366), Southern-Northwest Branch (R^2=0.0960), Southwest Branch (R^2=0.0869), Northern-Northwest Branch (R^2=0.0514), and Echo Glacier-Center (R^2=0.0021) (Fig. B.6).

3.4.3.3. Surface Variables

Slope and curvature were amongst the variables with the least relative importance in the random forest regression. In a linear regression, changes in firn thickness essentially show no correlation slope (R^2=0.0016) or curvature (R^2=0.0087). When broken out into separate branches and cross-sections, most of the surveyed areas center around curvature of 0 and slopes between 1-2º.

3.4.3.4. Ablation Variables

Distance from exposed bedrock had the fourth most importance in predicting firn thickness change, with less relative importance in the random forest regression than the positional variables, though higher than the surface variables. A linear regression shows a weak negative relationship between difference in firn thickness and distance to exposed bedrock, where the farther from the side walls a point is, the greater the decrease in firn thickness between years (R^2=0.0701). The areas with the greatest correlation between the difference in firn thickness and distance from exposed bedrock were Southwest Branch (R^2=0.2115), Southern-Northwest Branch (R^2=0.2058), and Echo Glacier-Right cross section (R^2=0.1729). Some correlation was observed for Matthes-Taku (R^2=0.1285), Northern-Northwest Branch (R^2=0.1195), while relatively none was observed for Demorest Glacier (R^2=0.0668), Echo Glacier-Right (R^2=0.0458), Echo Glacier-Center (R^2=0.0457), and Northern-Northwest Branch cross section (R^2=0.0450) (Fig. B.7).

Difference in average positive degrees had the second greatest importance in predicting firn thickness change outside of marine proximity. In a linear regression, this variable has a very weak correlation with difference in firn thickness ($R^2=0.0458$). That said, the relationship between these variables amongst individual branches was much greater for Demorest Glacier ($R^2=0.2931$), Matthes-Taku ($R^2=0.2088$), and Northern-Northwest Branch cross section ($R^2=0.1777$). Most of the other branches and cross-sections had similar or weaker correlation coefficients than the overall dataset, Northern-Northwest Branch ($R^2=0.0956$), Echo Glacier-Right ($R^2=0.0221$), Southern-Northwest Branch ($R^2=0.0202$), Echo Glacier-Center ($R^2=0.0105$), Echo Glacier-Right cross-section ($R^2=0.0060$).

Across the entire study site, all areas experienced an increase in the average number of positive degree days per season between the 2006-2011 period and the 2015-2020 period. There were no points where there was an average decrease. Areas below 1500 m a.s.l. experienced the greatest number of increased average positive degree days between the firn accumulation seasons.

3.5. Discussion

3.5.1. Firn Volume

Over about a decade of time, JIF has lost approximately over 50 percent of its firn volume. This scale of loss has implications for the future of JIF as a whole. The loss of this important input to glacier ice will decrease the overall ice volume and likely means that the contributions to sea-level rise from JIF are likely to increase. With less of this layer to buffer both the ice from the atmosphere and downstream ecosystems from rapid meltwater discharge, this loss could become a trend. Though drastic, because of the short residence time of firn in this area, this decrease in firn is likely due to decadal or sub-decadal trends in accumulation and ablation and thus are not irredeemable (without considering any effect on feedback loops).

It is possible to derive surface velocity from feature tracking and image pairing with the Inter-mission Time Series of Land Ice Velocity and Elevation (ITS_LIVE) dataset. A time series analysis of these available data from 1985-2018 demonstrate that the centerline velocity of T'aaḵú Ḵwáan Sít'i has not varied substantially outside of one standard deviation of the mean historical velocities (Fig. 3.10). I interpret this as a consistent velocity field trend through time and consider that observed changes are not likely to be the effect of increased dynamic thinning. Therefore, I do not attribute the observed firn thinning to dynamics and hypothesize it is more likely a combination of potential factors such as, increased ablation, decreased accumulation, or increased rate of firn densification. Gaps in the availability of calculated surface velocity limit these conclusions.

It is interesting to see such a drastic change in the firn volume on JIF especially considering the main outlet glacier of this portion of the icefield was advancing until the mid-2010s. If this difference in firn volume is a trend related to the initiation of retreat of T'aaḵú Ḵwáan Sít'i, it is likely a trend that is occurring for other Alaskan alpine glaciers and icefields where retreat has been ongoing. I would expect that perhaps more dramatic changes or trends might emerge in these systems too. In addition, modeling results suggest that despite some firn thickening at high elevations on the Greenland Ice Sheet, accelerated coastal firn thinning has been observed between 1980 and 2014 attributed to increased surface melt (Kuipers Munneke and others, 2015).
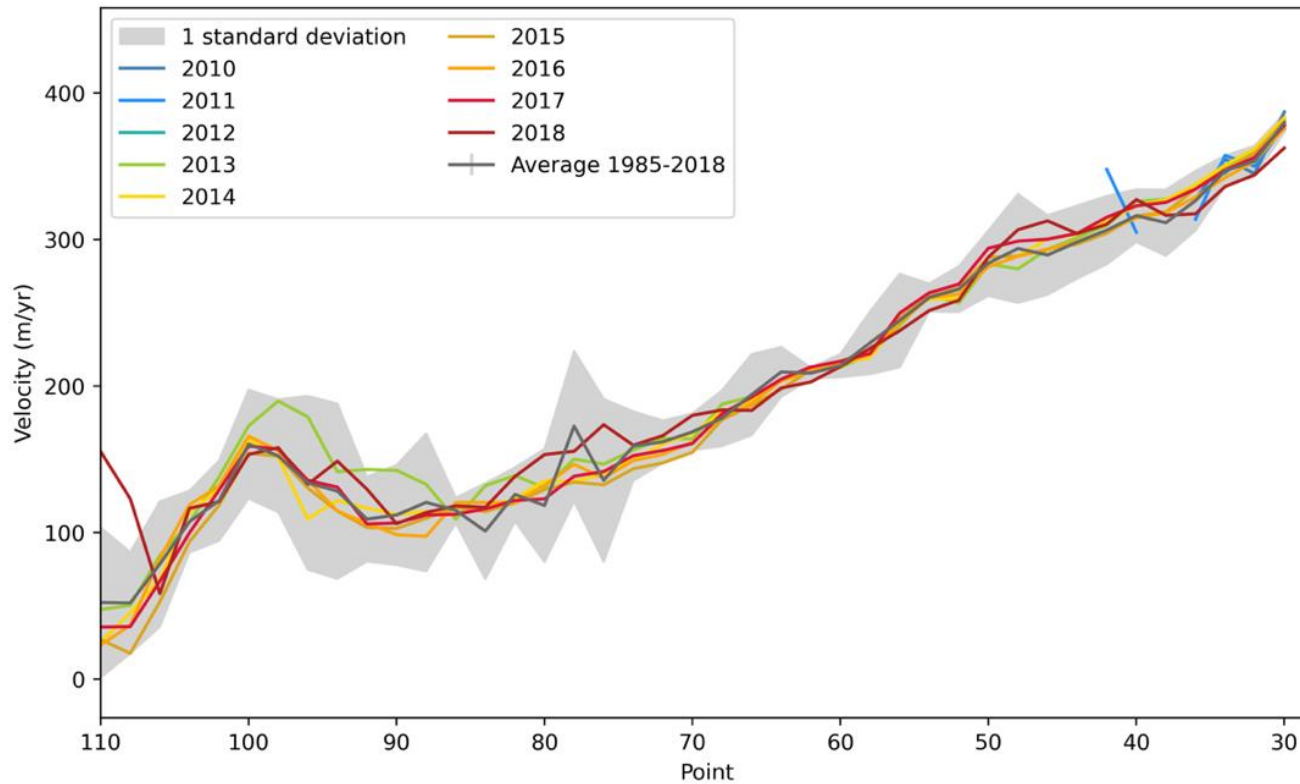
Figure 3.10. Average of the annual velocities with one standard deviation (grey) between 1985-2018 at each point along T'aaḵú Ḵwáan Sít'i and Matthes Glacier where data are available. Individual years of data near the time period of interest (2010-2018) are plotted in increasingly warm colors in more recent years. Point 110 on the left corresponds to the head of Matthes Glacier which flows into Taku Glacier where point 30 is nearest to the terminus.

3.5.2. Analysis and Trends

3.5.2.1. Positional Variables Because both marine proximity and elevation influence accumulation, these variables are most akin to representing accumulation patterns across the icefield in lieu of annual measurements of the entire study area. It then makes sense that these are the variables that have the greatest influence on the predictions of the random forest regression, given that firn existence depends first on there being accumulation. Areas that are most marine proximal maintained more firn, lost less firn than areas that were less marine proximal. This trend makes sense where less snow might fall further from the moisture source due to rain shadowing and more snow falls closer to the moisture source both due to moisture source proximity and rapid orographic uplift. With this difference in initial inputs, even with uniform ablation, areas with greater accumulation would maintain and develop more firn.

The direction of the relationship between elevation and difference in firn thickness is different than one might expect. As opposed to there being more firn loss at low elevations, with an increase in elevation, there is more firn loss at high elevations. One potential explanation for this relationship is that areas low in elevation and close to the ELA had little firn to begin with in the initial 2012 survey year. Hence, any loss or complete disappearance in firn could be lesser in magnitude than to higher elevation areas.

3.5.2.2. Surface Variables

Slope and curvature had little influence or impact on the change in firn thickness between years, which makes sense given that these are surface expressions and not necessarily indicative of firn thickness in this study area where there are not intense slopes. Perhaps firn thickness could be more heavily influenced in areas with greater variability and magnitude of slope or curvature, but this was not observed on JIF.

3.5.2.3. Ablation Variables

Distance from exposed bedrock and difference in positive degree days both showed moderate relative importance on the difference in firn thickness between 2012 and 2021, according to the random forest regression. Though a weak relationship, the further a point from exposed bedrock, the greater the loss in firn thickness is observed. Perhaps this is an effect of shading, wind drifting, or avalanching onto the areas closer to valley side walls allowing for less firn loss. But, equally so, this effect could be similar to that of elevation where areas close to the sidewalls generally have less firn to begin with due to longwave radiation from the bedrock. Further, more detailed analyses in these bedrock-proximal regions would be useful to elucidate the specific causes.

The difference in average annual positive degrees between firn accumulation seasons had an unexpected relationship with the difference in firn thickness between years for the overall dataset. Instead of increases in the average annual positive degrees being correlated with greater firn loss, the opposite is true. This could potentially be explained by the elevation dependence of temperature calculations at each point (Figs. A.5, A.8). Similar to how lower elevation areas had low relative firn thickness when compared to the rest of the study site, these highest elevation regions experienced the greatest increase in the number of positive degree days and in the annual average difference of positive degrees between firn accumulation seasons.

3.5.2.4. Smaller-scale Relationships

Overall, there was no individual variable that was strongly correlated with the difference in firn thickness across JIF between 2012 and 2021 when considering the entire surveyed area. That said, when the data was broken into individual tributaries and cross sections, multiple variables correlated with firn thickness difference. However, correlation varied across the icefield and were

both positive and negative for the same variable depending on the tributary. This suggests that smaller-scale relationships are impactful (Figs. A.5-A.11).

3.5.3. Assumptions and Limitations

Calculations of firn thickness in each year are based on the assumption that the relative permittivity of temperate firn across JIF is 6 ($v = 0.122$ m ns^{-1}). From the common midpoint surveys (CMP) conducted in 2015, it is reasonable to apply this relative permittivity to the firn layer. However, the CMP surveys were spatially and temporally constrained to a relatively small regions and time period and the properties of firn that affect relative permittivity (i.e., density and water content) are likely spatially and temporally variable. More refined estimates of firn volume and meltwater capacity would benefit from reduced uncertainties in water content, depth-density profiles, and changes to these two properties over time, across JIF. Despite the likely large quantitative uncertainties in firn volume derived from differencing the 2012 from the and 2021 data, the firn thickness reduction is obvious from the data, qualitatively (Fig. 3.6 and Figs. A.1-A.4).

Additionally, it is important to acknowledge that this is not a time series analysis. Instead, it is a change analysis with two endpoints. This constrains my ability to make conclusions about how fast change is occurring. There is only an absolute change demonstrated, instead of incremental change. This may overlook some of the firnpack evolution. That said, by being influenced by multi-year processes, firn existence, thickness, and volume does hold an indication of multi-year trend.

3.5.4. Implications

Within a decade of time, this drastic change in firn volume is concerning and likely connected to the regional shift towards lower annual mass balances and overall mass loss (Berthier and others,

2018; Rounce and others, 2023). Over 50 percent loss in firn volume over a decade reduces contributions to ice volume and will likely continue or exacerbate glacier retreat in the region.

Because firn itself is an important component of glacier structure and hydrology, its overall decrease in thickness and volume has implications for englacial and proglacial hydrology. Such a decrease in firn reduces the glacier system's ability to buffer runoff. In a smaller column of firn over glacier ice, it would be expected that water would move more quickly through this column than one of greater depth. This could increase the potential for local flooding and have implications for the future of JIF.

Because the terminus is currently protected by its proglacial shoal, changes in meltwater discharge may outweigh the balance between sediment flux contributing to terminus protection and meltwater flux that may erode this protection (Zechmann and others, 2020). Recent modeling of Eklutna Glacier in Southcentral Alaska demonstrates the increase in annual discharge and a decreasing mass balance with warmer temperatures (Geck and others, 2021).

As T'aaḵú Ḵwáan Sít'i retreats, it may also develop into a lake-terminating glacier, potentially exacerbated by meltwater runoff. Such a change could have profound impacts on glacier mass loss and dynamics (Truffer and Motyka, 2016) and downstream ecosystems. One example is Yakutat Glacier which is a low elevation, lake-terminating glacier located in southeast Alaska and is about half the area of T'aaḵú Ḵwáan Sít'i with similar mean annual precipitation. Though lower elevation than JIF, modeling results predict substantial retreat and thinning through the rest of the century (Trüssel and others, 2015). Llewellyn, Mendenhall, Gilkey and other glaciers draining from JIF have each resulted in the formation of lakes at their termini, potentially acting as a positive feedback loop that further enhances glacier retreat.

The effect of JIF firn thinning on englacial and downstream hydrology will evolve over time. In the short-term, it might expected to see increased incidence of saturated firn aquifers and surface runoff during the peak melt season. This meltwater flux could infuse colder water and more eroded sediment into the downstream ecosystem, affecting species sensitive to water temperature, sediment flux, and turbidity. In the long-term, should T'aakú Kwáan Sít'i recede or erode its terminal moraine becoming a marine or lake-terminating glacier in an over-deepened bed, this could then reduce the influx of meltwater and entrained sediment to Taku Inlet. The transition from a protected terminus to a lake or marine-terminating glacier might introduce more potential for melt to the system. In an over-deepened bed, this presents the potential to affect ice dynamics through increased subglacial meltwater movement, marine (or lake terminating) ice cliff instability with active calving, and increased ice velocity.

While firn albedo is lower than snow, it is still higher than glacier ice. In this way, it protects glacier ice from direct insolation where it exists. With thinner firn there is less of a buffer between the atmosphere and glacier ice. This has the potential to increase the system's sensitivity to instances of extreme temperatures and melt.

Ziemen and others (2016) predict a 58 to 68 percent decrease in ice volume from 2010 JIF ice volume by the end of the century under the RCP6.0 (+ 2.8ºC, globally) emissions scenario modeled with the Parallel Ice Sheet Model. Overall, such extensive firn thinning increases JIF's vulnerability to climatic change and may be the start to more rapid JIF retreat in the near future.

3.6. Conclusions and Remaining Questions

Analysis of firn thickness across the Juneau Icefield in 2012 and 2021 from repeated 400 MHz GPR surveys revealed there has been an overall firn thinning across the study site. This firn thinning has resulted in a calculated firn volume loss of 51.3 percent over the study period.

Analysis from both random forest regression relative importance and linear regression of variables that may explain this decrease in firn thickness showed that marine proximity, annual difference in positive temperature degrees, and elevation, were the most well-correlated variables, though these relationships varied across tributaries.

Firn thinning may occur through one or a combination of decreased accumulation or increased ablation, increased dynamic thinning, and an increased rate of firn densification. Future research should consider quantifying the other potential causes of firn thinning. This would include the rate of firn densification in temperate glacier systems over short, near annual timescales and in-situ measurements of surface velocity over multiple times during the years to determine any possible impact of dynamic thinning on firn thickness. Additionally, future studies should seek to limit assumptions in regard to the relative permittivity of the firn spatially and temporally by performing extensive ground truthing campaigns. This includes more detailed analysis of spatial and temporal variations in depth-density profiles and meltwater stored within the firn. Finally, it is worth considering a continuation of these repeated surveys to see the development of firn through time, and to better understand temperate firn processes.

CHAPTER 4

CONCLUSIONS & FUTURE WORK

4.1. Conclusions

This research focused on examining the spatial and temporal properties of snow and quantifying snow water equivalent and firn volume across the Juneau Icefield between 2012 and 2021. The basis of this analysis was built upon repeated 400 MHz ground-penetrating radar (GPR) surveys across the southern portion of the Juneau Icefield (JIF) collected with the Juneau Icefield Research Program in 2012 and 2021.

4.1.1. Variable Snow Properties and Snow Water Equivalent from Ground-penetrating Radar Across the Juneau Icefield, Alaska (Chapter 2)

Snow water equivalent (SWE) is one way to quantify and monitor the annual mass balance of glaciers, water resources, and potential contributions to sea-level rise. SWE across Alaskan glaciers, which outside of the polar continental ice sheets are experiencing the greatest degree of mass loss, is highly variable (Hugonnet et al., 2021; McGrath et al., 2015).

In Chapter 2, I presented the results of analysis of the annual accumulation in 2012 and 2021 from GPR surveys and mass balance snow pits to assess the snow water equivalent and liquid water content across JIF. Density trends with respect to depth are similar across JIF within and between years. Ground-truth efforts for assessing bulk radio wave velocity and relative permittivity of the snowpack suggest widespread variability in liquid water content across the study site and annually. This variability has the potential to result in high uncertainty in depth and SWE calculations from GPR. Accumulation, measured in SWE, at the time of surveys was greater in 2012 than in 2021. Overall, this research demonstrates that in temperate and maritime glacial

systems, estimating SWE requires extensive ground-truth campaigns to account for the spatial variability in liquid water content in the snowpack.

4.1.2. Firn Volume Loss Across the Juneau Icefield, Alaska between 2012 and 2021 (Chapter 3)

Firn is a crucial part of glacier systems as it is the snow accumulation that remains after the ablation season and over time densifies into glacier ice. Additionally, it acts as short-term meltwater storage which buffers runoff release to downstream water reservoirs or resources. How much firn accumulates and remains after each year serves as a multi-year record of recent accumulation and ablation trends.

In Chapter 3, with the same common-offset GPR dataset, I focused on the changes in firn thickness, volume, and meltwater storage capacity of the surveyed portion of JIF. Significant firn thinning was observed across the entire study site, with very few small areas of firn thickening, between the initial survey year in 2012 and the repeated survey in 2021. This resulted in an estimated over 50 percent decrease in firn volume over this decade. Changes in firn thickness were most correlated with variables related to accumulation patterns, namely marine proximity and elevation. Subsequent analyses of recent meteorological data revealed that firn accumulation period, the five water years preceding the surveys, in 2021 showed a positive change in the number of positive degree days for every day of the year when compared to the firn accumulation period for the 2012 surveys.

4.2. Limitations

These conclusions are limited to relative change analysis as opposed to trend analysis because this research considers two years of data that serve as end points to the time period of interest. Thus, this does not allow for attribution of specific changes between 2012 and 2021 directly to climatic change, though this is certainly a possible impetus for melt-influenced variability in liquid water

content during the summer, variability in large-scale accumulation patterns and snow water equivalent, as well as, decreases in firn volume.

As Chapter 2 outlines, for better interpretation of GPR data on temperate glaciers in a changing climate, it is crucial to conduct extensive ground-truthing campaigns to inform and validate any assumptions for radio wave velocity to calculate depth. While this was feasible and implemented for work with the annual accumulation layer, this was not the case with the firn layer. As accumulation at this study site can be 3-5 m of snow or more to excavate before reaching firn, it is difficult to determine the thickness of the firn layer itself through the methods available during data collection. While a common midpoint survey is a great tool to determine radio wave velocities at a point location, it's limited in implementation to point location much like firn coring. As such, the difference in firn thickness between years is subject to some added uncertainty and conclusions drawn from this should include this as a caveat.

From available data, it is not possible to discern exactly what is the main cause of firn thinning, especially as firn accumulation and survival is subject to multi-year timescales. Firn thinning may be caused by decreased snow accumulation, increased ablation, increased rate of firn densification, dynamic thinning, or a combination of these factors. Observed thinning does not appear to be due to dynamic thinning. Understanding which of these additional factors is the dominant cause for firn thinning in this region would have implications for better predicting glacier behavior.

4.3. Remaining Questions and Future Work

Future studies should consider a higher degree of temporal resolution for repeated surveys if the goal is to conduct time series analysis. This might include data collection along repeated survey tracks within the same season or in years in closer succession.

To better ground-truth layer thicknesses and radio wave velocities, future research might consider using firn coring at the sites of mass balance pits to record density and depth of the firn. An additional step-up from this to provide a more continuous and non-destructive acquisition of radio wave velocity variation and firn depth simultaneously would be to use a multi-offset ground-penetrating radar instrument at the same or similar frequency. This continuous information would better inform assumptions for radio wave velocity, water content, and density in temperate firn, reducing the uncertainty of depth calculations (Meehan and others, 2021). Additionally, because liquid water content can exhibit temporal variability, there remains a question of how variable this property is on different timescales. This could be examined with repeated common-offset or multi-offset surveys on a shorter temporal timescale of hours, days, or weeks.

Future work considering the factors related to firn thinning should consider a similar approach to addressing ground-truthing radio wave velocities in temperate firn: firn coring and multi-offset radar, for the aforementioned reasons. An additional consideration would be to use an ultra-high frequency Autonomous phase-sensitive Radio Echo Sounder (ApRES) to measure strain rate in the firn.

Finally, this study focused entirely on the Juneau Icefield, AK and it would be interesting to expand these efforts to other areas to potentially upscale these conclusions or better quantify uncertainty in methods between regions.

REFERENCES

Alley RB (1987) Firn densification by grain-boundary sliding: a first model. *J Phys Colloq*, **48**(C1), 249-256 (doi:10.1051/jphyscol:1987135)

Arcone SA, Lawson D, Delaney A (1995) Short-pulse radar wavelet recovery and resolution of dielectric contrasts within englacial and basal ice of Matanuska Glacier, Alaska, U.S.A. *J Glaciol*, **41**(137), 68-86 (doi:10.3189/S0022143000017779)

Arcone SA (2002) Airborne-radar stratigraphy and electrical structure of temperate firn: Bagley Ice Field, Alaska, U.S.A. *J Glaciol*, **48**(161), 317-334 (doi:10.3189/172756502781831412)

Beniston M (2003) Climatic Change in Mountain Regions: A Review of Possible Impacts. *Climatic Change*, **59**, 5–31 (doi:10.1023/A:1024458411589)

Berthier E, Larsen C, Durkin WJ, Willis MJ, Pritchard ME (2018) Brief communication: Unabated wastage of the Juneau and Stikine icefields (southeast Alaska) in early 21st century. *Cryosphere*, **12**, 1523-1530 (doi:10.5194/tc-12-1523-2018)

Bradford JH, Nichols J, Mikesell TD, Harper JT (2009) Continuous profiles of electromagnetic wave velocity and water content in glaciers: an example from Bench Glacier, Alaska, USA. *J Glaciol*, **50**(51), 1-8 (doi:10.3189/172756409789097540)

Campbell S, Kreutz K, Osterberg E, Arcone S, Wake C, Introne D, Volkening K, Winski D (2012a) Melt regimes, stratigraphy, flow dynamics and glaciochemistry of three glaciers in the Alaska Range. *J Glaciol*, **58**(207), 99-109 (doi:10.3189/2012JoG10J238)

Campbell S, Kreutz K, Osterberg E, Arcone S, Wake C, Volkening K, Winski D (2012b) Flow dynamics of an accumulation basin: a case study of upper Kahiltna Glacier, Mount McKinley, Alaska. *J Glaciol*, **58**(207), 185-195 (doi:10.3189/2012JoG10J233)

Campbell S, Balco G, Todd C, Conway H, Huybers K, Simmons C, Michael V (2013) Radar-detected englacial stratigraphy in the Pensacola Mountains, Antarctica: implications for recent changes in ice flow and accumulation. *Ann Glaciol*, **54**(63), 91-100 (doi: 10.3189/2013AoG63A371)

Campbell SW (2014) Determining Basin Geometry, Stability, and Flow Dynamics of Valley Glaciers with Ground-penetrating Radar [Doctoral Dissertation, University of Maine]

Case E and Kingslake J (2020) Observations and modeling of a stacked firn aquifer on a temperate, high-accumulation icefield, Abstract (C050-06W) presented at 2020 AGU Fall Meeting, 1-17 Dec.

Christianson K, Kohler J, Alley RB, Nuth C, van Pelt WJJ (2015) Dynamic perennial firn aquifer on an Arctic glacier. *Geophys Res Lett*, **42**(5), 1418-1426 (doi:10.1002/2014GL062806)

Chu W, Schroeder DM, Siegfried MR (2018) Retrieval of Englacial Firn Aquifer Thickness From Ice-Penetrating Radar Sounding in Southeastern Greenland. *Geophys Res Lett*, **45**(21), 11770-11778 (doi:10.1029/2018GL079751)

Clayton WS (2019) Measurement of unsaturated meltwater percolation flux in seasonal snowpack using self-potential. *J Glaciol*, **68**(267), 25-40 (doi:10.1017/jog.2021.67)

Colbeck SC (1973) Theory of Metamorphism of Wet Snow. *Cold Regions Research and Engineering Laboratory* (DA Project 4A061102B52E)

Connor C (2009) Field glaciology and earth systems science: The Juneau Icefield Research Program (JIRP), 1946-2008, in Whitmeyer SJ, Mogk DW, Pyle EJ (eds.) Field Geology Education: Historical Perspectives and Modern Approaches: Geological Society of America Special Paper 461, 173-184 (doi:10.1130/2009.2461(15))

Criscitiello AS, Kelly MA, Tremblay B (2010) The Response of Taku and Lemon Creek Glaciers to Climate. *Arct Antarct Alp Res*, **42**(1), 34-44 (doi:10.1657/1938-4246-42.1.34)

Cuffey KM and Paterson WSB (2010) The Physics of Glaciers, Fourth Edition. *Elsevier* (ISBN: 978-0-12-369461-4)

de Woul M, Hock R, Braun M, Thorsteinsson T, Jóhannesson T, Halldórsdóttir (2006) Firn layer impact on glacial runoff: a case study at Hofsjökull, Iceland. *Hydrol Process*, **20**(10), 2171-2185 (doi:10.1002/hyp/6201)

DeWalle DR and Rango A (2009) Principles of Snow Hydrology. *Cambridge University Press* (ISBN:9780511535673)

Dunse T, Schuler TV, Hagen JO, Eiken T, Brandt O, Høgda KJ (2009) Recent fluctuations in the extent of the firn area of Austfonna, Svalbard, inferred from GPR. *Ann Glaciol,* **50**(50), 155-162 (doi: 10.3189/172756409787769780)

Forster RR, Box JE, van den Broeke MR, Miège C, Burgess EW, van Angelen JH, Lenaerts JTM, Koenig LS, Paden J, Lewis C, Gogineni SP, Leuschen C, McConnell JR (2014). Extensive liquid meltwater storage in firn within the Greenland ice sheet. *Nature*, **7**, 95-98 (doi:10.1038/ngeo2043)

Fountain AG (1989) The Storage of Water in, and Hydraulic Characteristics of, the Firn of South Cascade Glacier, Washington State, U.S.A. (1989) *Ann Glaciol*, **13**, 69-75 (doi:10.3189/S0260305500007667)

Fountain AG (1996) Effect of snow and firn hydrology on the physical and chemical characteristics of glacial runoff. *Hydrol Process*, **10**, 509-521 (doi:10.1002/(Sici)1099-1085(199604)10:4<509::Aid-Hyp389>3.0.Co;2-3)

Gascon G, Sharp M, Burgess D, Bezeau P, Bush ABG (2013) Changes in accumulation-area firn stratigraphy and meltwater flow during a period of climate warming: Devon Ice Cap, Nunavut, Canada. *J Geophys Res*, **118**(4), 2380-2391 (doi:10.10022/2013JF002838)

Geck J, Hock R, Loso MG, Ostman J, Dial R (2021) Modeling the impacts of climate change on mass balance and discharge of Eklutna Glacier, Alaska, 1985-2019. *J Glaciol*, **67**(265), 909-920 (doi:10.1017/jog.2021.41)

Gerbi C, Mills C, Clavette R, Campbell S, Bernsen S, Clemens-Sewall D, Lee I, Hawley R, Kreutz K, Hruby K (2021) Microstructures in a shear margin: Jarvis Glacier, Alaska. *J Glaciol*, **67**(266), 1163-1176 (doi:10.1017/jog.2021.62)

Harper J, Humphrey N, Pfeffer WT, Brown J, Fettweis X (2012) Greenland ice-sheet contribution to sea-level rise buffered by meltwater storage in firn. *Nature*, **491**, 240-243 (doi:10.1038/nature11566)

Hamlet AF, Mote PW, Clark MP, Lettenmaier DP (2005) Effects of Temperature on Snowpack Trends in the Western United States. *J Clim*, **18**, 4545-4561 (doi:10.1175/JCLI3538.1)

Hart JK, Rose KC, Martinez K (2011) Temporal englacial water content variability associated with a rapidly retreating glacier. *Earth Surf Process Landf*, **36**(9), 1230-1239 (doi:10.1002/esp.2148)

Herron MM and Langway CC (1980) Firn Densification: An Empirical Model. *J Glaciol,* **25**(93), 373-385 (doi:10.3189/S0022143000015239)

Hugonnet R, McNabb R, Berthier E, Menounos B, Nuth C, Girod L, Huss M, Dussaillant I, Brun F, Kääb A (2021) Accelerated global glacier mass loss in the early twenty-first century. *Nature*, **592**, 726-731 (doi:10.1038/s41586-021-03436-z)

Jansson P, Hock R, Schneider T (2003) The concept of glacier storage: a review. *J Hydrol*, **282**(1-4), 116-129 (doi:10.1016/S0022-1694(03)00258-0)

Johnson AC and Meyer FJ (2022) Detection of glacier firn aquifers across Alaska using time series of Sentinel-1 SAR, Abstract (C22F-0825) presented at the 2022 AGU Fall Meeting, 12-16 Dec.

Koenig LS, Miège C, Forster RR, Brucker L (2013) Initial in situ measurements of perennial meltwater storage in the Greenland firn aquifer. *Geophys Res Lett*, **41**(1), 81-85 (doi:10.1002/2013GL058083)

Kovacs A, Gow AJ, Morey RM (1995) The in-situ dielectric constant of polar firn revisited. *Cold Reg Sci Technol*, **23**(3), 245-256 (doi:10.1016/0165-232X(94)00016-Q)

Kuipers Munneke P, Litenberg SRM, van den Broeke MR, van Angelen, Forster RR (2014)
Explaining the presence of perennial liquid water bodies in the firn of the Greenland Ice
Sheet. *Geophys Res Lett*, **41**(2), 476-483 (doi:10.1002/2013GL058389)

Kuipers Munneke P, Ligtenberg SRM, Noël BPY, Howat IM, Box JE, Mosley-Thompson E,
McConnell JR, Steffen K, Harper JT, Das SB, van den Broeke MR (2015) Elevation
change of the Greenland Ice Sheet due to surface mass balance and firn processes, 1960-
2014. *Cryosphere*, **9**, 2009-2015 (doi:10.5194/tc-9-2009-2015)

LaChapelle ER (1954) Snow Studies on the Juneau Icefield. *Dept of Exploration and Field
Research, American Geographical Society*, Report No. 9 (AD 028874)

Larsen CF, Burgess E, Arent AA, O'Neel S, Johnson AJ, Kienholz C (2015) Surface melt
dominates Alaska glacier mass balance. *Geophys Res Lett*, **42**(14), 5902-5908
(doi:10.1002/2015GL064349)

Lemke P, Ren JF, Alley RB, Allison I, Carrasco JF, Flato G, Fujii Y, Kaser G, Mote P, Thomas
RH, Zhang T (2007) Observations: Changes in Snow, Ice and Frozen Ground. In: *Climate
Change 2007: The Physical Science Basis. Contribution of Working Group I to the Fourth
Assessment Report of the Intergovernmental Panel on Climate Change*. [Solomon S, Qin
D, Manning M, Chen Z, Marquis M, Averyt KB, Tignor M, Miller HL (eds.)]. Cambridge
University Press, United Kingdom and New York, NY, USA, pp. 337–383.

Maeno N and Ebinuma T (1983) Pressure Sintering of Ice and Its Implication to the
Densification of Snow at Polar Glaciers and Ice Sheets. *J Phys Chem*, **87**, 4103-4110
(doi:10.1021/j100244a023)

Maurer J, Mannello M, Schild K, Zhu Y, Campbell S (in review) Upscaling of Existing
Ground-Penetrating Radar Surveys with Artificial Neural Networks in Temperate Glacial
Environments. *J Glaciol*

McGrath D, Sass L, O'Neel S, Arendt A, Wolken G, Gusmeroli A, Kienholz C, McNeil C (2015)
End-of-winter snow depth variability on glaciers in Alaska. *J Geophys Res*, **120**, 1530-
1550 (doi:10.1002/2015JF003539)

McGrath D, Sass L, O'Neel S, McNeil C, Candela SG, Baker EH, Marshall H (2018) Interannual
snow accumulation variability on glaciers derived from repeat extensive ground-
penetrating radar surveys. *The Cryosphere*, **12**, 3617-3633 (doi:10.5194/tc-12-3617-2018)

McNeil C, O'Neel S, Loso M, Pelto M, Sass L, Baker EH, Campbell S (2020) Explaining mass
balance and retreat dichotomies at Taku and Lemon Creek Glaciers, Alaska. *J Glaciol*,
66(258), 530-542 (doi:10.1017/jog.2020.22)

Meehan TG, Marshall HP, Bradford JH, Hawley RL, Overly TB, Lewis G, Graeter K, Osterberg
E, McCarthy F (2021) Reconstruction of historical surface mass balance, 1984-2017 from

GreenTrACS multi-offset ground-penetrating radar. *J Glaciol*, **67**(262), 219-228 (doi:10.1017/jog.2020.91)

Mercer J (1961) The Response of Fjord Glaciers to Changes in the Firn Limit. *J Glaciol*, **3**(29), 850-858 (doi:103189/S0022143000027222)

Miège C, Forster RR, Bruker L, Koenig LS, Solomon DK, Paden JD, Box JE, Burgess EW, Miller JZ, McNerney L, Brautigam N, Fausto RS, Gogineni S (2016) Spatial extent and temporal variability of Greenland firn aquifers detected by ground and airborne radars. *J Geophys Res*, **121**(12), 2381-2398 (doi:10.1002/2016JF003869)

Miller O, Solomon DK, Miège C, Koenig L, Forster R, Schmerr N, Ligtenberg SRM, Legchenko A, Voss CI, Montgomery L, McConnell JR (2020) Hydrology of a Perennial Firn Aquifer in Southeast Greenland: An Overview Driven by Field Data. *Water Resources Res*, **56**(8), e2019WR026348 (doi:10.1029/2019WR026348)

Montgomery L, Miège C, Miller J, Scambos TA, Wallin B, Miller O, Solomon DK, Forster R, Koenig L (2020) Hydrologic Properties of a Highly Permeable Firn Aquifer in the Wilkins Ice Shelf, Antarctica. *Geophys Res Lett*, **47**(22), e2020GL089552 (doi:10.1029/2020GL089552)

Moore RD and 7 others (2009) Glacier change in western North America: influences on hydrology, geomorphic hazards and water quality. *Hydrol. Process.,* **23**, 42-61 (doi:10.1002/hyp.7162)

Nolan M, Motyka RJ, Echelmeyer K, Trabant DC (1995) Ice-thickness measurements of Taku Glacier, Alaska, U.S.A., and their relevance to its recent behavior. *J Glaciol*, **41**(139), 541-553 (doi:10.3189/S0022143000034870)

Ochwat N, Marshall S, Moorman B, Criscitiello A, Copland L (2021) Meltwater Storage in the firn of Kaskawulsh Glacier, Yukon: meltwater effects, densification, and the development of a perennial aquifer. *The Cryosphere*, 2021-2040 (doi:10.5194/tc-15-2021-2021)

Oerlemans J, Bassford RP, Chapman W, Dowdeswell JA, Glazovsky AF, Hagen JO, Melvold K, De Ruyter de Wildt M, van de Wal RSW (2005) Estimating the contribution of Arctic glaciers to sea-level change in the next 100 years. *Ann Glaciol*, **42**, 230-236 (doi: 10.3189/172756405781812745)

O'Neel S, Hood E, Bidlack AL, Fleming SW, Arimitsu ML, Arendt A, Burgess E, Sergeant CJ, Beaudreau AH, Timm K, Hayward GD, Reynolds JH, Pyare S (2015) Icefield-to-Ocean Linkages across the Northern Pacific Coastal Temperate Rainforest Ecosystem. *Biosci*, **65**(5), 499-512 (doi:10.1093/biosci/biv027)

Pedregosa F, Varoquaux G, Gramfort A, Michel V, Thirion B, Grisel O, Blondel M, Prettenhofer P, Weiss R, Dubourg V, Vanderplas J, Passos A, Cournapeau D,Brucher M, Perrot M, Duchesnay E (2011) Scikit-learn: Machine Learning in Python. *J Mach Learn Res*, **12**, 2825-2830

Pelto M and Miller MM (1990) Mass Balance of the Taku Glacier, Alaska from 1946 to 1986. *Northwest Sci*, **64**(3), 121-130

Pelto M, Kavanaugh J, McNeil C (2013) Juneau Icefield Mass Balance Program 1946-2011. *Earth Syst Sci Data*, **5**, 319-330 (doi:10.5194/essd-5-319-2013)

Poinar K, Dow CF, Andrews LC (2019) Long-Term Support of an Active Subglacial Hydrologic System in Southeast Greenland by Firn Aquifers. *Geophys Res Lett*, **46**(9), 4772-4781 (doi:10.1029/2019GL082786)

Roth A, Hock R, Schuler TV, Bieniek PA, Pelto M, Aschwanden A (2018) Modeling Winter Precipitation Over the Juneau Icefield, Alaska, Using a Linear Model of Orographic Precipitation. *Front Earth Sci*, **6**(20) (doi:10.3389/feart.2018.00020)

Rounce DR, Hock R, Maussion F, Hugonnet R, Kochtitzky W, Huss M, Berthier E, Brinkerhoff D, Compagno L, Copland L, Farinotti D, Menounos B, McNabb RW (2023) Global glacier change in the 21st century: Every increase in temperature matters. *Science*, **379**(6627), 78-83 (doi:10.1126/science.abo1324)

Schroeder DM (2023) Paths forward in radioglaciology. *Ann Glaciol*, 1-5 (doi:10.1017/aog.2023.3)

Sihvola A and Tiuri M (1986) Snow Fork for Field Determination of the Density and Wetness Profiles of a Snow Pack. *IEEE Trans Geosci Remote Sens*, **GE-24**(5), 717-721 (doi:10.1109/TGRS.1986.289619)

Sharp M (1951) Meltwater behavior in firn on upper Seward Glacier, St. Elias Mountains, Canada. Union Géodésique et Géophysique Internationale - Association Internationale d'Hydrologie Scientifique, 1, 246-251

Sold L, Huss M, Eichler A, Schwikowski M, and Hoelzle M (2015) Unlocking annual firn layer water equivalents from ground-penetrating radar data on an Alpine glacier. *The Cryosphere* **9**, 1075-1087 (doi:10.5194/tc-9-1075-2015)

Stevens CM, Verjans V, Lundin JMD, Kahle EC, Horlings AN, Horlings BI, Waddington ED (2020) The Community Firn Model (CFM) v1.0. *Geosci Model Dev*, **13**, 4355-4377 (doi:10.5194/gmd-13-4355-2020)

Techel F and Pielmeier C (2011) Point observations of liquid water content in wet snow – investigating methodical, spatial, and temporal aspects. *Cryosphere*, **5**, 405-418 (doi:10.5194/tc-5-405-2011)

Thornton TF (2010) Haa Leelk'w Has Aani Saax'u/Our Grandparents' Names on the Land. *University of Washington Press* (ISBN: 9780295988580)

Tiuri M, Sihvola A, Nyfors E, Hallikaiken M (1984) The complex dielectric constant of snow at microwave frequencies. *IEEE J Ocean Eng*, **9**(5), 377-382 (doi: 10.1109/JOE.1984.1145645)

Truffer M and Motyka RJ (2016) Where glaciers meet water: Subaqueous melt and its relevance to glaciers in various settings. *Rev Geophys*, **54**(1), 220-239 (doi:10.1002/2015RG000494)

Trüssel BL, Truffer M, Hock R, Motyka RJ, Huss M, Zhang J (2015) Runaway thinning of the low-elevation Yakutat Glacier, Alaska and its sensitivity to climate change. *J Glaciol*, **61**(225), 65-75 (doi:10.3189/2015JoG14J125)

van Wessem JM, Steger CR, Wever N, van den Broeke MR (2021) An exploratory modelling study of perennial firn aquifers in the Antarctic Peninsula for the period 1979-2016. *The Cryosphere*, **15**, 695-714 (doi:10.5194/tc-15-695-2021)

Verboncouer H, Stock J, Muhlheim R, Bingham E, Constantini W, Dryak MC, Armstrong R, Campbell SW, Brazo J (2019) Characterization of a Shallow Firn Aquifer at the Matthes-Llewellyn Glacier Divide, Juneau Icefield, Alaska, Abstract (C13C-1307) presented at 2019 AGU Fall Meeting, 9-13 Dec.

Wilkinson DS (1988) A Pressure-sintering Model for the Densification of Polar Firn and Glacier Ice. *J Glaciol*, **34**(116), 40-45 (doi:10.3189/S0022143000009047)

Winski D, Kreutz, Osterberg E, Campbell S, Wake C (2012) High-frequency observations of melt effects on snowpack stratigraphy, Kahiltna Glacier, Central Alaska Range. *Hydrol Process*, **26**, 2573-2582 (doi:10.1002/hyp.9348)

Xu M, Yang Q, Hu X, Liang K, Vihma T (2022) Record-breaking rain falls at Greenland summit controlled by warm moist-air intrusion. *Environ Res Lett*, **17**(4), 044061 (doi:10.1088/1748-9326/ac60d8)

Zechmann JM, Truffer M, Motyka RJ, Amundson JM, Larsen CF (2020) Sediment redistribution beneath the terminus of an advancing glacier, Taku Glacier (T'aak̲ú K̲wáan Sít'i), Alaska. *J Glaciol*, **67**(262), 204-218 (doi:10.1017/jog.2020.101)

Zemp M, Huss M, Thibert E, Eckert N, McNabb R, Huber J, Barandun H, Machguth H, Nussbaumer SU, Gärtner-Roer I, Thomson L, Paul F, Maussion F, Kutuzov S, Cogley (2019) Global glacier mass changes and their contributions to sea-level rise from 1961-2016. *Nature*, **568**, 382-386 (doi:10.1038/s41586-019-1071-0)

Ziemen FA, Hock R, Aschwanden A, Khroulev C, Kienholz C, Melkonian A, Zhang J (2016) Modeling the evolution of the Juneau Icefield between 1971 and 2100 using the Parallel Ice Sheet Model (PISM). *J Glaciol*, **62**(231), 199-214 (doi:10.1017/jog.2016.13)

	DJF	MAM	JJA	SON	Annual
Mean	2.2	12.9	0.2	4.5	19.8
Standard Deviation	1.4	4.0	0.3	1.2	6.0
Minimum	0.2	6.4	0.0	2.2	11.2
25%	1.0	8.0	0.0	3.4	13.8
50%	1.8	14.0	0.2	4.2	19.8
75%	3.6	16.4	0.2	5.8	25.4
Maximum	4.8	17.8	1.4	6.2	28.2

Table A.1. Descriptive statistics on the difference in the number of positive degree days per season between the firn accumulation seasons.

	DEM	ECHO_C	ECHO_R	MT	NWBN	NWBS	SWB
Mean	-100	-80.9	-55.8	-71.2	-27.1	-47.4	-71.8
Stand. Dev.	0.0	18.0	26.1	25.8	15.2	16.3	33.6
Min	-100	-100	-94.8	-100	-66.9	-100	-100
25%	-100	-92.0	-80.9	-100	-36.7	-55.2	-100
50%	-100	-88.3	-58.7	-68.1	-29.9	-47.0	-100
75%	-100	-74.9	-33.5	-56.3	-12.8	-38.6	-52.2
Max	-100	-33.3	0.6	-5.3	1.1	-3.1	14.4

Table A.2. Descriptive statistics of the percent change in firn thickness across the study site by tributary branch.
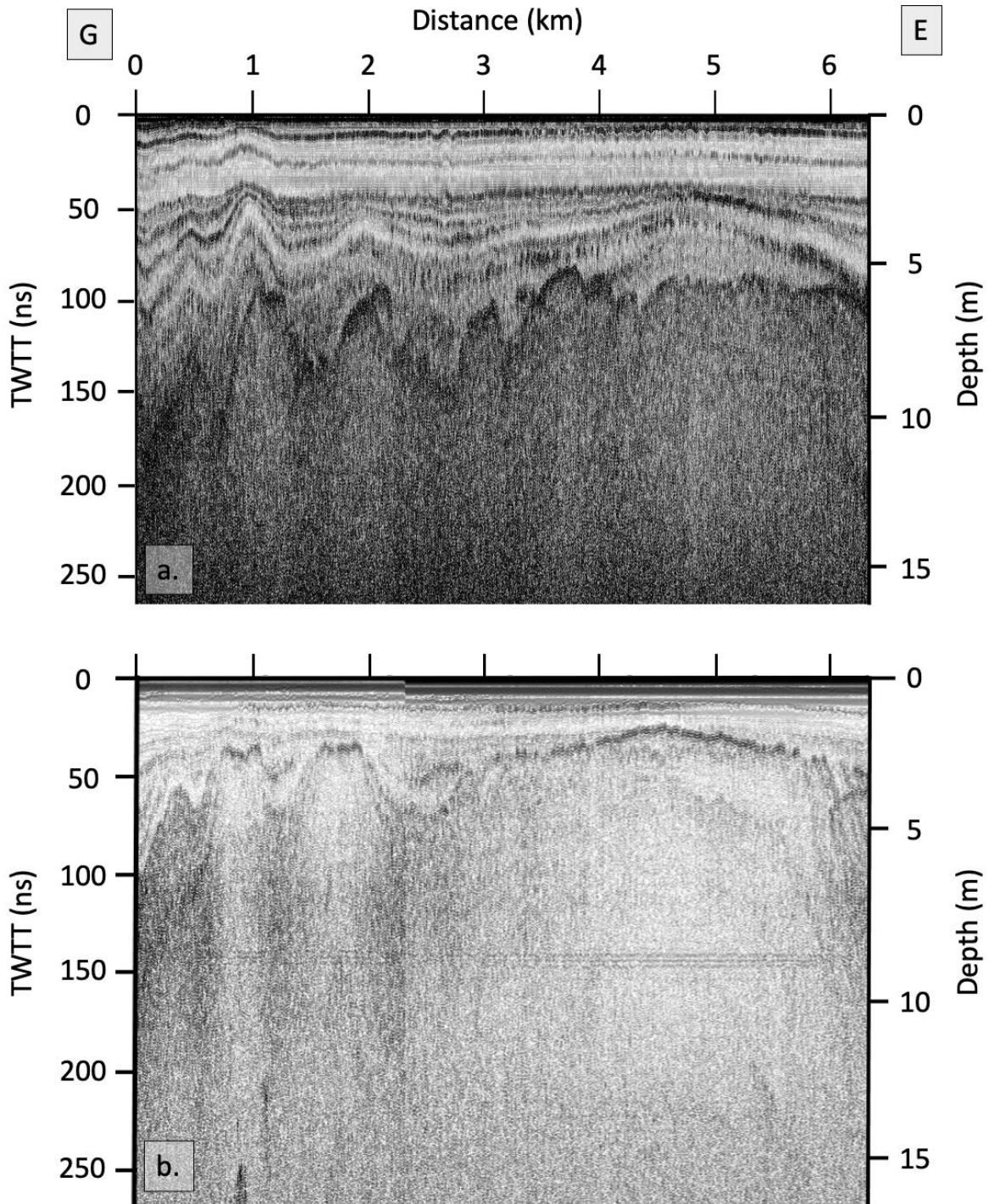
Figure A.1. Centerline 400 MHz surveys of Echo Glacier – Right in (a) 2012 and (b) 2021, located from G to E on the location map (Figure 3.3c). Two-way travel time (TWTT) shown with depth (m) interpreted with a relative permittivity of 6 ($v = 0.122$ m ns^{-1}).
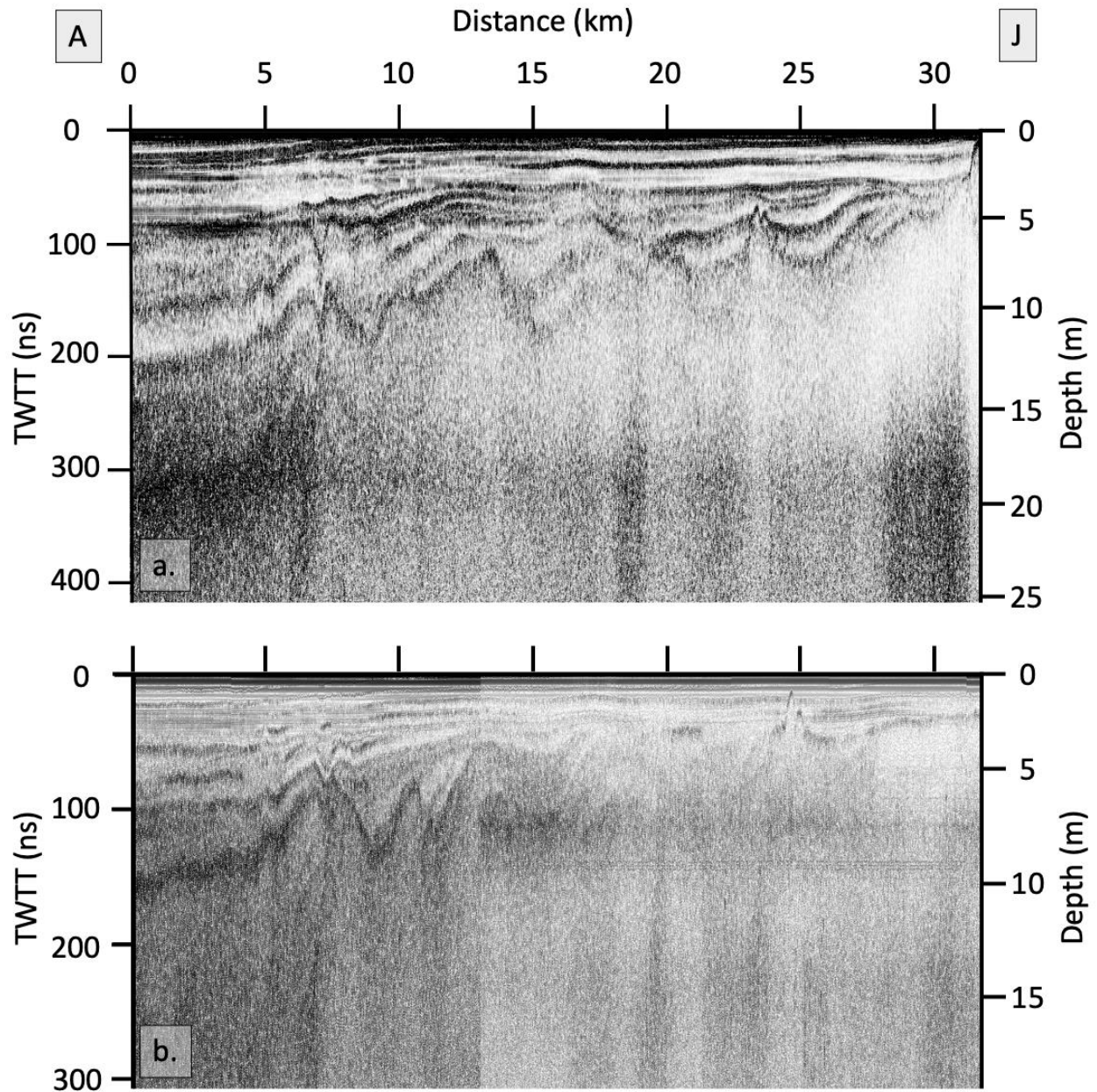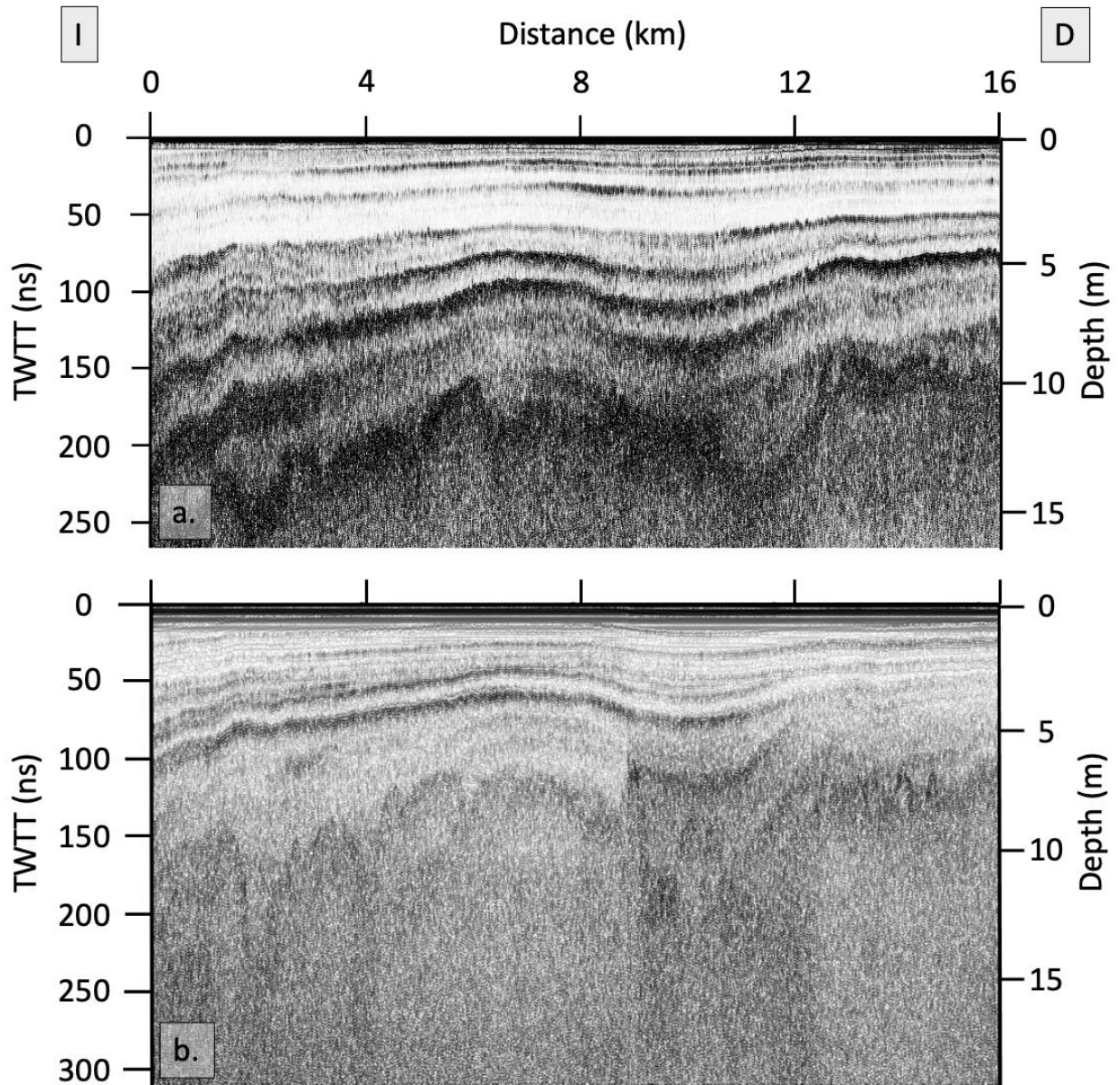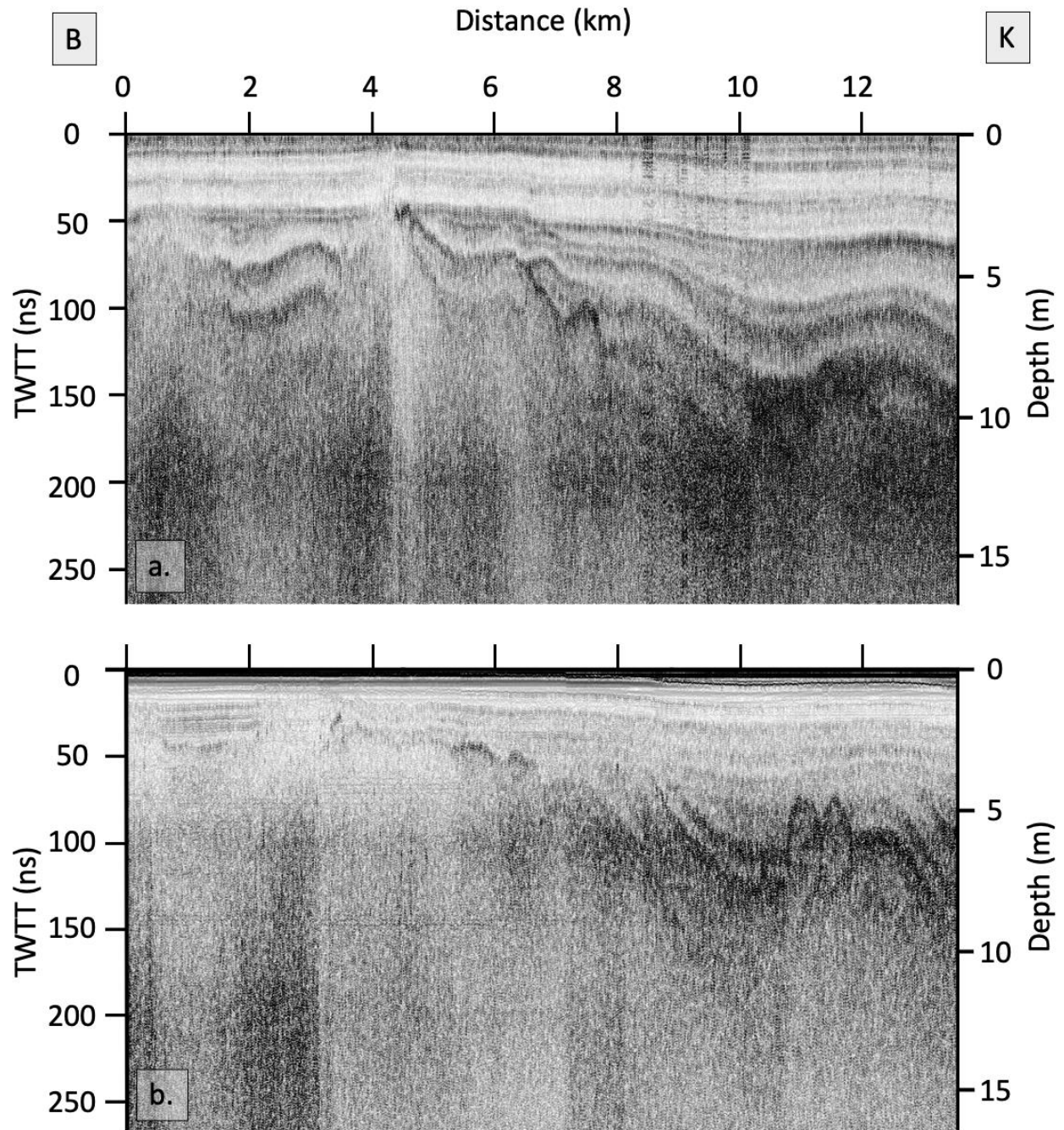
Figure A.2. Centerline 400 MHz surveys of Matthes-Taku in (a) 2012 and (b) 2021, located

from A to J on the location map (Figure 3.3c). Two-way travel time (TWTT) shown with depth

(m) interpreted with a relative permittivity of 6 (v = 0.122 m ns^{-1}).

Figure A.3. Centerline 400 MHz surveys of Southern-Northwest Branch in (a) 2012 and (b) 2021, located from I to D on the location map (Figure 3.3c). Two-way travel time (TWTT) shown with depth (m) interpreted with a relative permittivity of 6 (v = 0.122 m ns^{-1}).

Figure A.4. Centerline 400 MHz surveys of Southwest Branch in (a) 2012 and (b) 2021, located

from I to D on the location map (Figure 3.3c). Two-way travel time (TWTT) shown with depth

(m) interpreted with a relative permittivity of 6 (v = 0.122 m ns^{-1}).
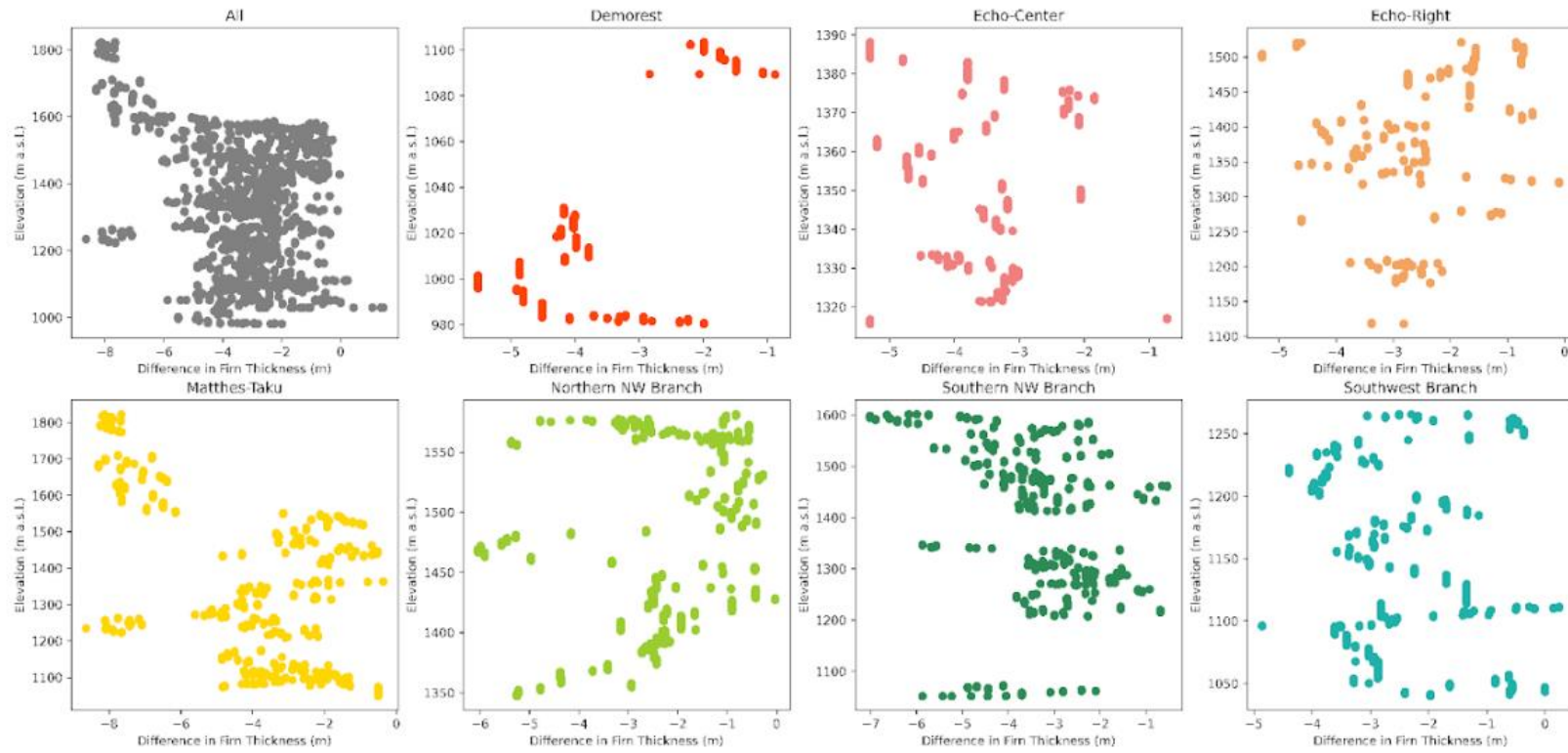
Figure A.5. Difference in firn thickness (m) between 2012 and 2021 versus elevation (m a.s.l.) for each main tributary.
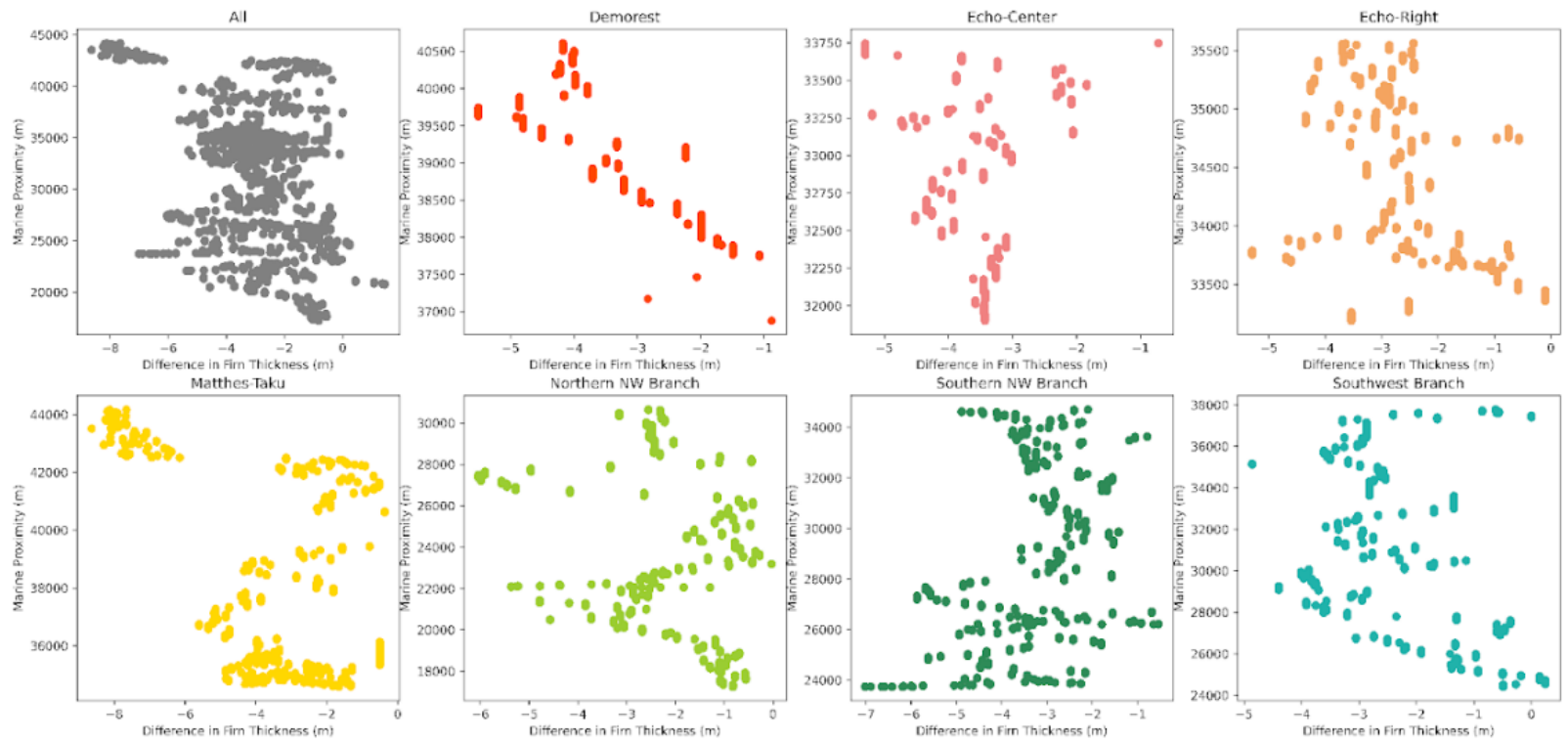
Figure A.6. Difference in firn thickness (m) between 2012 and 2021 versus distance from a moisture source (m) for each main tributary.
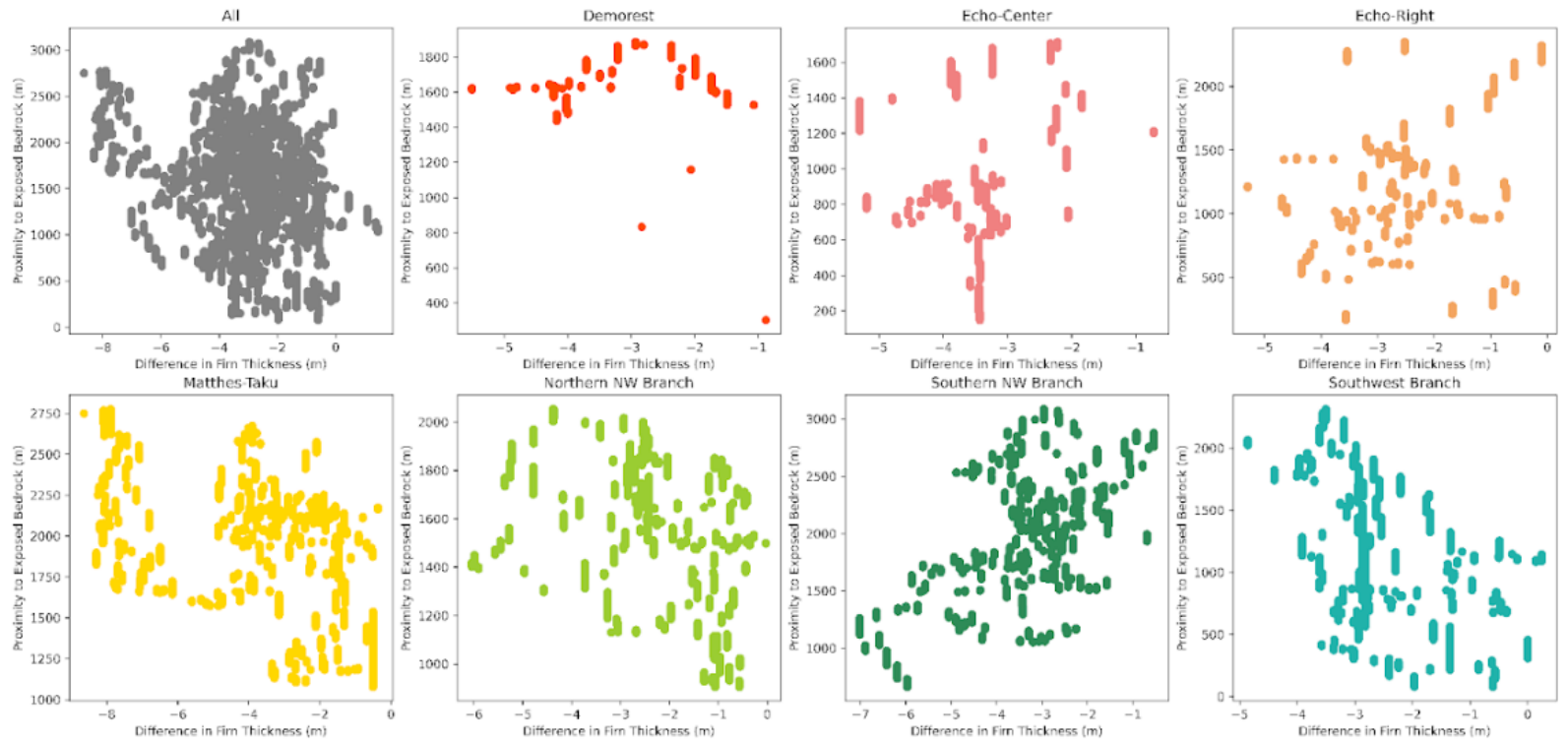
Figure A.7. Difference in firn thickness (m) between 2012 and 2021 versus distance from exposed bedrock (m) for each main tributary.
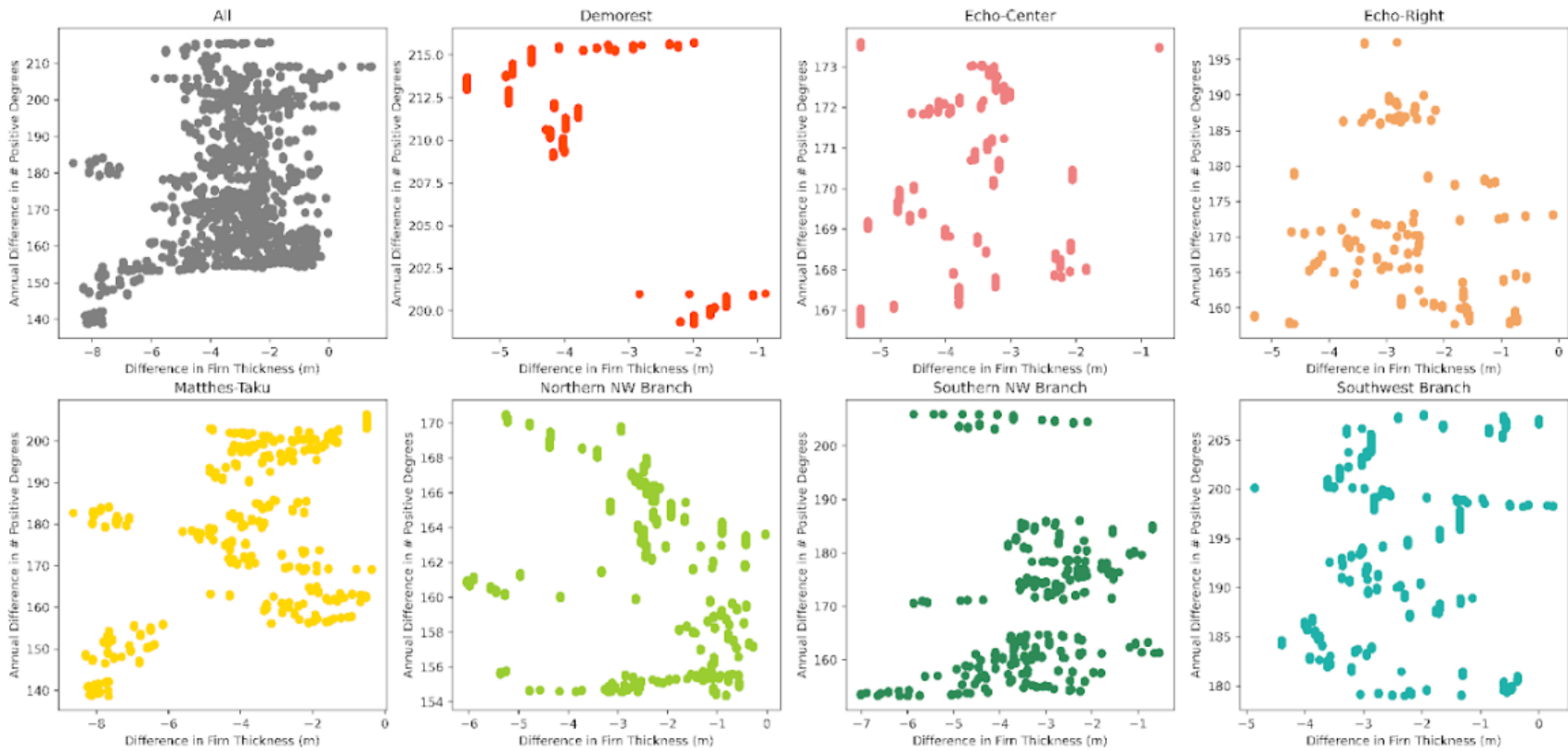
Figure A.8. Difference in firn thickness (m) between 2012 and 2021 versus distance from annual difference in positive degrees for each main tributary.
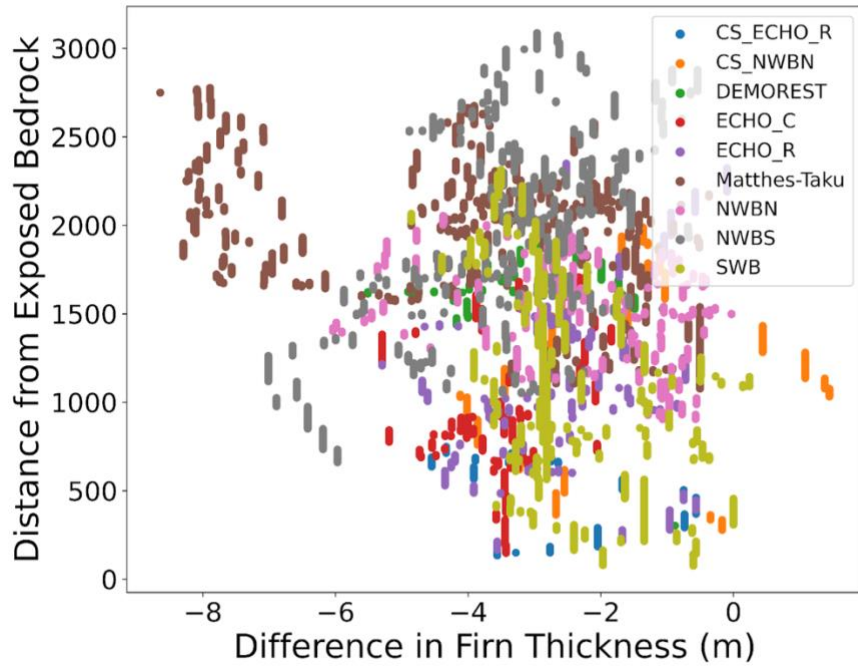
Figure A.6. Difference in firn thickness (m) between 2012 and 2021 versus distance from a
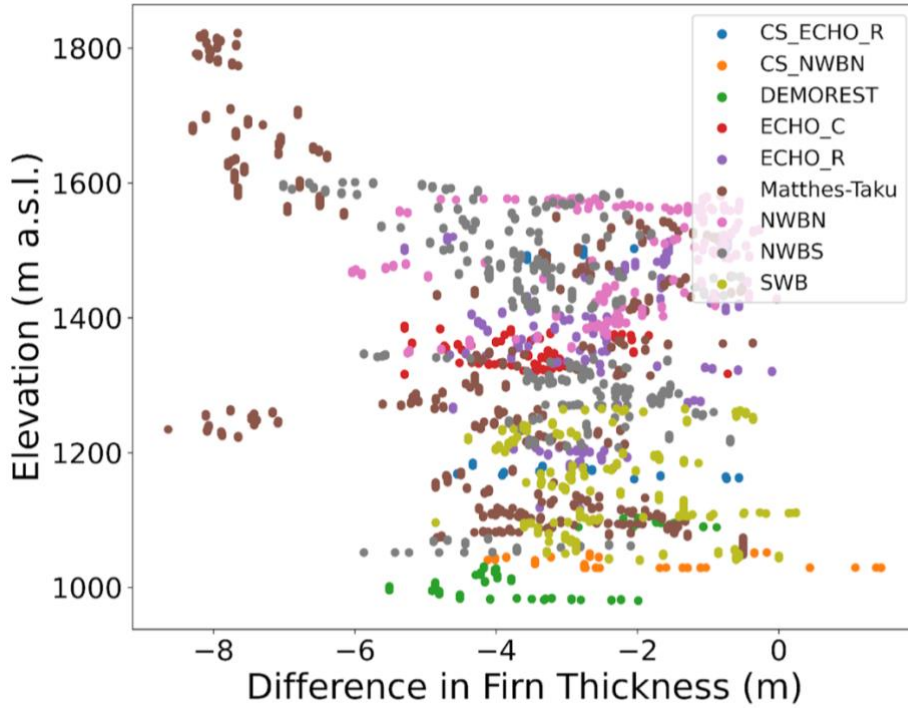
exposed bedrock (m).

Figure A.10. Difference in firn thickness (m) between 2012 and 2021 versus elevation (m a.s.l.).
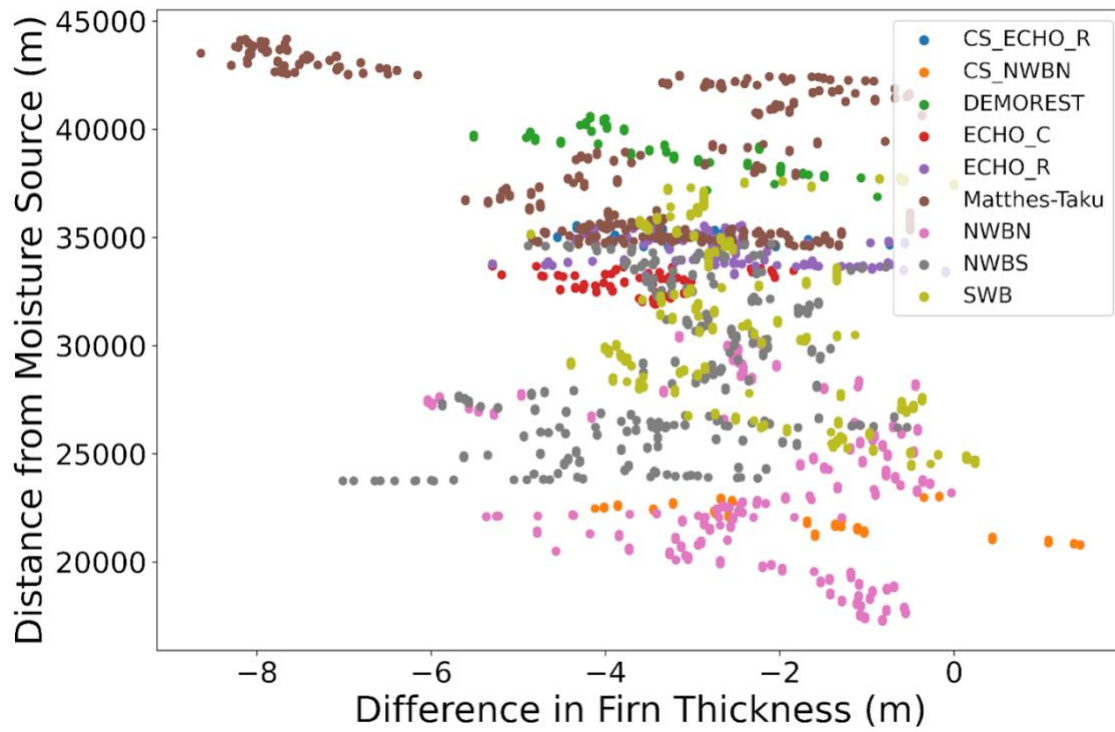
Figure A.11. Difference in firn thickness (m) between 2012 and 2021 versus distance from a

moisture source (m).

BIOGRAPHY OF THE AUTHOR

Mikaila Mannello is originally from West Chester, Pennsylvania. She completed her B.S. in Environmental Science with additional concentrations in Geographic Information Systems and International Relations at the University of Pittsburgh in December of 2020. She is enthusiastic about all things ice, radar, rock climbing, and skiing. When she's not in the field or writing her thesis, you can find her on the trails, climbing, or getting coffee with friends. After receiving her degree, Mikaila will be pursuing a Ph.D. in Earth and Climate Sciences at the University of Maine. Mikaila is a candidate for the Master of Science degree in Quaternary and Climate Studies from the University of Maine in December 2023.